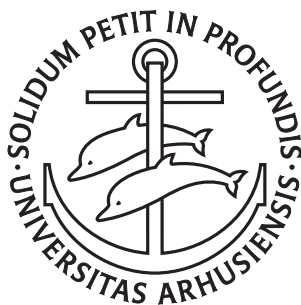


---

# A study of nuclear dynamics following excitation and ionization in small molecules and weakly bound clusters

---

A Dissertation  
Presented to the Faculty of Science and Technology  
of Aarhus University  
in Partial Fulfillment of the Requirements  
for the PhD Degree



by  
Qingli Jing  
September, 2018

Supervisor: Lars Bojer Madsen



---

# English summary

Great advances in modern laser technologies have made the generation of intense femtosecond and attosecond light pulses a trivial task in laboratory. The ultrashort pulses can induce electronic excitation and ionization in atomic and molecular systems. In the molecular systems, nuclear dynamics, such as dissociation into two fragments, can also take place due to a change of the potential landscapes seen by the nuclei. Thus, the theoretical study of the interaction of molecules with ultrashort light pulses is challenging since both the electronic and nuclear dynamics should be taken into consideration.

The Monte Carlo wave packet (MCWP) approach can be applied to study the nuclear dynamics following electronic excitation and ionization in small molecules and weakly bounded clusters. This method is equivalent to the master equation in the Lindblad form in quantum optics. In the MCWP method, we treat the interaction between the bound and continuum electronic states in a molecule as the interaction between an open system and its surroundings. This simplification greatly reduces the computational costs. In this thesis, we have obtained the nuclear kinetic energy release (KER) spectra following dissociative double ionization of  $\text{H}_2$  and triple ionization of  $\text{Ne}_2$ . An analysis of these nuclear KER spectra helps to reveal the nuclear dynamics during these processes.

---

# Danish Resumé

Store fremskridt indenfor moderne laserteknologi har gjort det til en triviel opgave at generere intense femtosekund og attosekund lypulser i laboratoriet. De ultrakorte pulser kan frembringe både elektroniske excitationer og ionisering af atomare- og molekulære systemer. I molekulære systemer kan nuklear dynamik, såsom dissociation i to fragmenter, også induceres på grund af ændringer i potentialelandskabet. Derfor er den teoretiske undersøgelse af interaktionen mellem molekyler og ultrakorte lypulser udfordrende, da både den elektroniske og nukleare dynamik skal tages i betragtning.

Monte Carlo-bølgepakken (MCWP) tilgangen kan anvendes til at studere den nukleare dynamik efter elektronisk excitation og ionisering i små molekyler og svagt bundne klynger. Denne metode svarer til masterligningen i Lindblad-form i kvanteoptik. I MCWP-metoden behandler vi samspillet mellem de bundne og kontinuerte elektroniske tilstande i et molekyle som interaktionen mellem et åbent system og dets omgivelser. Denne forenkling reducerer i høj grad beregningsomkostningerne. I denne afhandling har vi fundet spektrene for udsendelse af nuklear kinetisk energi (KER) efter dissociativ dobbelt ionisering af  $H_2$  og trippel ionisering af  $Ne_2$ . En analyse af disse nukleare KER-spektre hjælper med at afsløre den nukleare dynamik under disse processer.

---

# Preface

This thesis summarizes the work done during my Ph.D. studies at Department of Physics and Astronomy, Aarhus University, under the supervision of Professor Lars Bojer Madsen.

## Notation

Atomic units  $4\pi\epsilon_0 = \hbar = m_e = e = 1$  are used throughout this report unless stated otherwise.

## Acknowledgements

I want to express my great gratitude to my supervisor Lars Bojer Madsen for him offering me the opportunity to conduct my PhD studies under his excellent guidance. He has a strong passion for physics and is very kind, patient, and considerate.

I would like to thank Elke Fasshauer, Jørgen Johansen Rørstad, Nikolaj Schrøder Wittig Ravn, and Alexander Holm Kiilerich for writing the Danish resumé for this thesis. They also helped me to improve the English summary. I would like to thank Lun Yue for giving part of his Fortran codes to accelerate the startup of my PhD project. I also benefited a lot from discussion with him about my project. I would like to thank Chuan Yu for helping me solve a lot of technical problems

---

when I write my thesis. I would like to show my great thanks to all the group members. It is my pleasure to meet all of you.

I would like to thank the MEDEA project to provide me the funding for my PhD studies and to offer me the opportunity to become closer to many famous scientists. Thanks a lot to all the MEDEA colleagues.

I am really grateful for the two months' visit of Fernando Martín's group in Madrid. I really enjoyed working together with Alicia Palacios, Fernando Martin and the other colleagues in Madrid.

Great and great thanks to my family and friends to support me from the bottom of heart.

Finally, thank the beautiful world.

*Qingli Jing,  
Aarhus, September, 2018.*

---

# List of Abbreviations

|                |   |
|----------------|---|
| <b>KER</b>     | kinetic energy release  |
| <b>MCWP</b>    | Monte Carlo wave packet   |
| <b>FEL</b>     | free electron laser   |
| <b>HHG</b>     | high-harmonic generation  |
| <b>TDSE</b>    | time-dependent Schrödinger equation                               |
| <b>TDFCC</b>   | time-dependent Feshbach close coupling                            |
| <b>TDGASCI</b> | time-dependent generalized-active-space configuration-interaction |
| <b>MCTDHF</b>  | multiconfigurational time-dependent Hartree-Fock                  |
| <b>CREI</b>    | charge-resonance-enhanced ionization                              |
| <b>TISE</b>    | time-independent Schrödinger equation                             |
| <b>DES</b>     | doubly excited state  |
| <b>ICD</b>     | interatomic (intermolecular) Coulombic decay                      |
| <b>ETMD</b>    | electron transfer mediated decay                                  |

---

# Contents

|   |            |
|---|------------|
| <b>Preface</b>  | <b>iii</b> |
| <b>Contents</b>   | <b>vi</b>  |
| <b>I Overview</b>   | <b>1</b>   |
| <b>1 Introduction</b>   | <b>2</b>   |
| <b>2 TDSE for a molecular system</b>  | <b>9</b>   |
| 2.1 Laser-induced ionization . . . . .  | 9          |
| 2.2 Molecular Hamiltonian . . . . .   | 10         |
| 2.3 Time-independent Schrödinger equation for the electronic<br>Hamiltonian . . . . . | 14         |
| 2.4 Time-dependent Schrödinger equation for the nuclear<br>motion . . . . .           | 15         |
| <b>3 the Monte Carlo wave packet approach</b>   | <b>19</b>  |
| 3.1 Equivalence with the master equation . . . . .                                    | 19         |
| 3.2 Calculation strategy for the deterministic sampling method                        | 23         |
| 3.3 Approximations and simplifications . . . . .                                      | 25         |
| 3.4 Applications of the MCWP approach . . . . .                                       | 27         |
| <b>4 Dissociative single or double ionization of H<sub>2</sub></b>                    | <b>29</b>  |



|                            |   |               |
|----------------------------|---|---------------|
| 4.1                        | Implementation of the MCWP method to double ionization of $H_2$ . . . . .                               | 29            |
| 4.2                        | Nuclear KER spectra at near- and mid-IR wavelengths   | 32            |
|                            | Influences of laser parameters . . . . .  | 33            |
|                            | Influences of nuclear mass . . . . .  | 41            |
| 4.3                        | Nuclear KER spectra in an XUV-pump-IR-probe setup   | 42            |
| 4.4                        | Nuclear KER spectra when autoionization from doubly excited states is involved . . . . .                | 47            |
| 4.5                        | Concluding remarks . . . . .  | 55            |
| <b>5</b>                   | <b>Dissociative triple ionization of <math>Ne_2</math></b>  | <b>57</b>     |
| 5.1                        | Implementation of the MCWP method to triple ionization of $Ne_2$ . . . . .                              | 60            |
| 5.2                        | Nuclear KER spectra following triple ionization of $Ne_2$ interacting with coherent XUV pulse . . . . . | 66            |
| 5.3                        | Nuclear KER spectra following triple ionization of $Ne_2$ interacting with chaotic XUV pulses . . . . . | 73            |
| 5.4                        | Concluding remarks . . . . .  | 74            |
| <b>6</b>                   | <b>Summary and outlook</b>  | <b>77</b>     |
| <br><b>II Publications</b> |   | <br><b>79</b> |
|                            | <b>Paper I</b>  | <b>80</b>     |
|                            | <b>Paper II</b>   | <b>92</b>     |
|                            | <b>Bibliography</b>   | <b>107</b>    |



# Part I

## Overview

---

# Introduction

Molecules, which are composed by at least two atoms, are abounding in the universe. They are stable because there are chemical bonds between the constituent atoms. Due to the very small spatial scale of a molecule, quantum effects become important. Thus, in theory, to correctly predict the behaviors of a molecule, one has to resort to the quantum methods. Compared with atoms, the motion of molecules are more complex. Apart from translation in space, they can rotate and vibrate. It is known that the timescales for the dynamics in quantum systems like atoms and molecules can be expected from the time-energy uncertainty relation  $\Delta t \Delta E \approx 1$ . The energy uncertainty  $\Delta E$ , related to the discrete energy levels that are coherently populated, is dependent on the (reduced) mass of the considered object. Simply speaking,  $\Delta E$  is inversely proportional to the (reduced) mass of an object. Thus, the heavier the object is, the smaller  $\Delta E$  is and the larger  $\Delta t$  is. As a result, the timescales for the vibrational and rotational dynamics in a heavier molecule is larger than that in a lighter molecule. Even though the timescales for the nuclear dynamics are more or less different for different molecules, the rotation of molecules usually takes place on a timescale of picoseconds ( $10^{-12}$  s) and the vibration usually on a timescale of femtoseconds ( $10^{-15}$  s). For the much lighter electrons, their dynamics occur on a much smaller timescale of attoseconds ( $10^{-18}$  s). To image and control such fast nuclear and electronic dynamics in molecules, one can resort to femtosecond and attosecond light pulses to obtain time-resolved spectroscopy.

---

Femtosecond pulses can be generated by femtosecond laser sources. For example, the versatile femtosecond titanium sapphire laser (Ti:Al<sub>2</sub>O<sub>2</sub>) can produce pulses within the visible and near-infrared spectrum [1–3]. To produce laser pulses at shorter ultraviolet [4] or longer mid-infrared wavelengths [5–7], one can utilize the nonlinear optical effects in materials such as sum- and difference-frequency mixing. To generate femtosecond pulses at x-ray wavelength, one strategy is to apply femtosecond laser pulses in the visible or infrared light spectrum to modulate the energy of electrons in an electron storage ring in synchrotrons [8, 9]. Apart from that, femtosecond and subfemtosecond x-ray pulses can be generated by tailoring of the bunch electron distribution in a self-amplified spontaneous-emission free-electron laser (FEL) [10, 11].

The much shorter attosecond pulses can be produced via high-harmonic generation (HHG) by irradiating femtosecond laser pulses on a gas jet. One can obtain a train of attosecond pulses when the driving laser pulse is multi-cycle [12–14]. An isolated attosecond pulse would be obtained instead when the driving laser pulse is few-cycle [15–18]. Isolated attosecond pulses can be also produced with multi-cycle laser pulses by applying optical gating techniques such as polarization gating and two-color gating [19].

There have been many theoretical and experimental works in studying the interaction of molecules with femtosecond and attosecond light pulses. Various phenomena can be observed in molecules upon interacting with ultrashort pulses, i.e.,

- **non-adiabatic molecular alignment** induced by femtosecond laser pulses [20–22], the dynamic alignment of a molecule corresponds to a revival of a rotational wave packet at a rotational period. The rotational wave packet in a given vibronic band is created by coherent excitation of an ensemble of rotational states.
- **bond softening** and **bond hardening** [23], a sufficiently strong laser field can either weaken or strengthen the molecular bonds and thus dissociation or association can be induced.
- **above-threshold dissociation** [24], more photons are absorbed than required to overcome the bond energy and the access energy

appears as an ensemble of peaks spaced by a photon energy in the kinetic energy release spectrum.

- **dissociative ionization** [25, 26], it describes a process that dissociation of a molecule is accompanied with the occurrence of ionization. The ionization can be described in different regimes, e.g., tunneling ionization, over-the-barrier ionization and single- or multi-photoionization. One can employ dissociative ionization in molecules to achieve a coherent control of chemical reactions [27].
- **electron localization** in molecular dissociation [28–30] due to a coherent superposition of electronic states in different symmetries,
- **laser-induced electron diffraction** to image ultrafast molecular dynamics [31–33], the field-ionized coherent electron wave packet is accelerated by the laser field and its rescattering from its parent molecular ion mimics the conventional electron diffraction of an electron beam.
- **electron charge migration** in molecules via electron correlation [34, 35].

In addition to the above mentioned phenomena, anomalously high ionization at large internuclear separations resulting from charge-resonance-enhanced ionization (CREI) [36, 37] can be observed in some diatomic molecular ion.

We are particularly interested in resolving and retrieving nuclear dynamics in this thesis as control over nuclear dynamics is prerequisite for realizing control of chemical reactions. Many techniques have been developed to probe nuclear dynamics in molecules. For example, the vibrational wave packet in  $D_2^+$  was observed from the nuclear KER spectra of  $D_2^+$  by exploiting the correlation between the electronic and nuclear wave packets [38]. Apart from that, the pump-probe setup, by which the nuclear KER spectra were obtained as a function of delay, was widely used to image the ultrafast nuclear wave packet motion in real time [39–41]. It was also demonstrated that using the chirp in the HHG spectra allows information about nuclear dynamics on a

---

subfemtosecond timescale [42]. Moreover, the HHG spectra can be used to image molecular orbitals [43]. Nuclear dynamics in molecules can be also reflected by the photoelectron spectra [44] and by the attosecond transient absorption spectra [45].

When we look back into the history, we can find that it was the study of light-matter interaction that eventually resulted in the establishment of modern quantum mechanics. In the late 19th and early 20th century, classical physics failed in explaining the Rayleigh–Jeans law in blackbody radiation and the photoelectric effect in metal. The first problem, later known as ultraviolet catastrophe, was solved by Max Planck through assuming that the absorption or emission of electromagnetic radiation by a blackbody can be only in the form of discrete packets called *quanta*. Soon after, the photoelectric effect was successfully explained by Albert Einstein after introducing the hypothesis that light energy is carried in discrete packets called *photon*. The discrete or quantized description was later extended to material systems and sparked the birth of the old quantum theory in the early 20th century. This theory brought about strong brainstorming to the scientists at that time and numerous breakthroughs promoted the emergence of quantum mechanics. Nowadays, quantum mechanics has become a fundamental theory to describe microscopic systems.

The Hamiltonian is of fundamental importance in the formulation of a quantum theory. The Hamiltonian for a molecule interacting with an ultrashort pulse is time-dependent. Thus, one can perform a simulation of the quantum dynamics of the molecular system by solving the time-dependent Schrödinger equation (TDSE). Many methods have been developed to solve the TDSE for a molecular system, e.g.,

- the **time-dependent Feshbach close coupling (TDFCC)** method, this is an *ab initio* method and the TDSE is solved using the spectral method, where the total wave function is expanded in the basis of electronic eigenstates by diagonalizing the field-free Hamiltonian. The Feshbach formalism introduces projection operators to project the total wave function onto non-resonant scattering and bound states, respectively. This method has been used to study resonant dissociative photoionization of diatomic molecules where singly or doubly excited states are involved [46–49].

- the **multiconfigurational time-dependent Hartree-Fock (MCT-DHF)** method generalized to treat correlated electronic and molecular dynamics in diatomic molecules [50], in this method, the correlated state of a multi-electron system is expressed by a superposition of determinant of time-dependent orbitals.
- the **time-dependent generalized-active-space configuration-interaction (TDGASCI)** approach to study correlated ionization dynamics of diatomic molecules [51], in this method, the many-body wave function is expanded based on the configuration interaction and the determinantal space is restricted to a reduced subspace.
- the **Monte Carlo wave packet (MCWP)** method applied in this thesis, this method treats ionization as a decay process where electrons are gradually lost to the surroundings. Lack of information related to the continuum electrons, the MCWP method is especially powerful in studying nuclear dynamics following double or multiple ionization of small molecules. This method was initially developed for dissipative processes in quantum optics [52] and was applied to study dissociative double ionization of  $\text{H}_2$  or  $\text{D}_2$  [53–55] and  $\text{O}_2$  [56]. A good agreement between the results obtained by this method and by the experiments [57, 58] has been achieved.

In addition to solving the TDSE, laser-induced coupled electron-nuclear dynamic can be obtained by solving quantum Liouville–von Neumann equation with the semiclassical surface hopping method [59].

## Outline of this thesis

This thesis presents theoretical studies on the nuclear dynamics following electronic excitation and ionization of small molecules and weakly bounded clusters by the MCWP approach. It is divided into two parts: **Part One** gives an overview of the discussed topics and **Part Two** attaches our publications [60, 61]. We organize the remaining chapters of **Part One** as follows:



- 
- Started from the molecular Hamiltonian, **Chapter 2** introduces the TDSE for a molecular system exposed to external electromagnetic fields.
  - **Chapter 3** provides a detailed description of the MCWP approach including its equivalence with the master equation in quantum optics, its implementation under the deterministic sampling method and the approximations and simplifications it has made.
  - **Chapter 4** simulates single or double ionization of  $H_2$  when exposed to intense laser pulses by applying the MCWP approach. The interaction of  $H_2$  with different laser pulses including single infrared and XUV pulses and two pulses in a pump-probe setting are discussed. When the XUV pulses are applied, nuclear dynamics in the singly or doubly excited states in  $H_2$  are induced.
  - **Chapter 5** extends the MCWP approach to simulate dissociative triple ionization of the neon dimer. A comparison between our simulation and a recent experiment in an XUV-pump-XUV-probe setup [62] is carried out.
  - **Chapter 6** gives a brief summary and conclusion of this thesis as well as a short outlook on future research.



---

# TDSE for a molecular system

In this chapter, we will deduce the time-dependent Schrödinger equation (TDSE) for the interaction of a molecule with intense laser pulses starting from the molecular Hamiltonian. Before that, we will first have a brief discussion of different ionization regimes in the following.

## 2.1 Laser-induced ionization

When an atom or molecule interacts with an intense laser pulse, ionization may take place since the external field is comparable to the internal field that binds the outer electron. The ionization is separated into two regimes by the Keldysh parameter  $\gamma$ , i.e.,

$$\gamma = \sqrt{\frac{I_p}{2U_p}}, \quad (2.1)$$

where  $I_p$  is the ionization potential and  $U_p$  is the pondermotive energy and is determined as

$$U_p = \frac{F^2}{4\omega^2}, \quad (2.2)$$

where  $F$  is the electric field strength and  $\omega$  is the frequency of the external field.

If  $\gamma \lesssim 1$  is satisfied, the field-induced ionization can be described as a tunneling process. When a strong electrostatic field is applied,

the potential well felt by the electrons is suppressed to form a finite barrier through which an electron can tunnel out. When the field strength is sufficiently large (larger than a critical value), the finite barrier is so suppressed that over-the-barrier ionization can take place, i.e., the electron can escape the nuclear core over the barrier.

When a strong oscillating laser field at a very low frequency is applied, the potential well would change adiabatically following the instantaneous field in a quasi-static picture. An electron can tunnel out through the barrier only if the tunneling time is smaller than half of the laser period, i.e., tunneling of an electron should be finished before the direction of electric field is reversed. Over-the-barrier ionization can be similarly induced by a sufficiently strong laser field at a very low frequency.

If  $\gamma \gg 1$  is satisfied, the ionization can be described as a multiphoton process: when a laser field at a sufficiently high frequency is applied, the electron may absorb a large amount of energy, i.e., several photons, from the external field before it succeeds in escaping the nucleus due to the fast change of direction of the electric field. When the frequency is extremely high, the ionization can be described as a single- or double-photon process: absorption of one or two photons from the external field is sufficient to support the energy for the electron escaping the nuclear core.

## 2.2 Molecular Hamiltonian

Hamiltonian is the starting point to perform a quantum-mechanical description of a system. For a molecular system with  $N_n$  nuclei and  $N_e$  electrons interacting with an external laser field, its time-dependent Hamiltonian in the laboratory frame of reference is expressed as

$$\begin{aligned}
 H_{\text{total}}(t) &= \sum_j^{N_n} \frac{\vec{p}_{Nj}^2}{2m_{Nj}} + \sum_j^{N_e} \frac{\vec{p}_{ej}^2}{2} + \frac{1}{2} \sum_{j,k \neq j}^{N_n} \frac{Z_j Z_k}{|\vec{R}_j - \vec{R}_k|} + \frac{1}{2} \sum_{j,k \neq j}^{N_e} \frac{1}{|\vec{r}_j - \vec{r}_k|} \\
 &- \sum_{j,k}^{N_n, N_e} \frac{Z_j}{|\vec{R}_j - \vec{r}_k|} + V_I(t), \tag{2.3}
 \end{aligned}$$

where  $\vec{p}_{Nj} = -i\nabla_{\vec{R}_j}$  ( $\vec{p}_{ej} = -i\nabla_{\vec{r}_j}$ ) is the momentum operator of the  $j$ th nucleus (electron),  $Z_j$  and  $m_{Nj}$  denote the charge and mass of

the  $j$ th nucleus, and  $\vec{R}_j$  ( $\vec{r}_j$ ) is the position vector of the  $j$ th nucleus (electron). On the right hand of Eq. (2.3), from left to right, the first term represents the kinetic energy operator of the  $N_n$  nuclei, the second term the kinetic energy operator of the  $N_e$  electrons, the third term the Coulomb interaction between the  $N_n$  nuclei, the fourth term the Coulomb interaction between the  $N_e$  electrons, the fifth term the Coulomb interaction between the  $N_n$  nuclei and  $N_e$  electrons and the last term the laser-molecule interaction operator, which has different forms in the length and velocity gauges, i.e.,

$$V_I(t) = \begin{cases} \vec{F}(t) \cdot (\sum_j^{N_e} \vec{r}_j - \sum_j^{N_n} Z_j \vec{R}_j) & \text{LG,} \\ \sum_j^{N_e} (\vec{p}_{ej} \cdot \vec{A}(t) + \frac{\vec{A}^2(t)}{2}) + \sum_j^{N_n} (-Z_j \vec{p}_{nj} \cdot \vec{A}(t) + \frac{Z_j^2 \vec{A}^2(t)}{2}) & \text{VG,} \end{cases} \quad (2.4)$$

where  $\vec{F}(t)$  and  $\vec{A}(t)$  are the electric field and vector potential of the applied laser pulse, respectively. The laser-molecule interaction operator in the above equation also implies the application of dipole approximation. In this thesis, we will use the Hamiltonian in the length gauge. For many cases, it is more convenient to use the Hamiltonian in the center of mass frame instead of the Hamiltonian in Eq. (2.3). This is because the center of mass frame, which is independent of experimental geometries, can provide intuitive pictures of the considered processes. The position vector of the center of mass in the laboratory frame is

$$\vec{R}_{\text{CM}} = \frac{\sum_j^{N_n} m_{Nj} \vec{R}_j + \sum_j^{N_e} \vec{r}_j}{\sum_j^{N_n} m_{Nj} + N_e}. \quad (2.5)$$

The position vectors of the nuclei and electrons in the center of mass frame are

$$\vec{\mathbf{R}}_j = \vec{R}_j - \vec{R}_{\text{CM}}, \quad (2.6)$$

$$\vec{\mathbf{r}}_j = \vec{r}_j - \vec{R}_{\text{CM}}. \quad (2.7)$$

Exploiting the fact that the position of the center of mass in the center of mass frame is the origin of this frame, we obtain the following relation

$$\vec{\mathbf{R}}_{\text{CM}} = 0 = \frac{\sum_j^{N_n} m_{Nj} \vec{\mathbf{R}}_j + \sum_j^{N_e} \vec{\mathbf{r}}_j}{\sum_j^{N_n} m_{Nj} + N_e}. \quad (2.8)$$

For a diatomic molecule, i.e.,  $N_n = 2$ , the Coulomb interaction between the two nuclei only depends on their relative position vector, i.e.,

$$\vec{\mathbf{R}} = \vec{\mathbf{R}}_1 - \vec{\mathbf{R}}_2. \quad (2.9)$$

Combining Eqs. (2.8-2.9) together, we can first express the position vectors of the two nuclei in the center of mass frame, i.e.,  $\vec{\mathbf{R}}_1$  and  $\vec{\mathbf{R}}_2$ , by the relative position vector of the two nuclei  $\vec{\mathbf{R}}$  and the position vectors of the electrons in the center of mass frame  $\vec{\mathbf{r}}_j$ . By applying the relation in Eq. (2.6), we can then represent the position vectors of the nuclei in the laboratory frame by the position vector of the center of mass in the laboratory frame  $\vec{\mathbf{R}}_{\text{CM}}$ , the relative positive vector between the two nuclei  $\vec{\mathbf{R}}$ , and the position vectors of the electrons in the center of mass frame  $\vec{\mathbf{r}}_j$ , i.e.,

$$\vec{\mathbf{R}}_1 = \frac{-\sum_j^{N_e} \vec{\mathbf{r}}_j + m_{N2} \vec{\mathbf{R}}}{m_{N1} + m_{N2}} + \vec{\mathbf{R}}_{\text{CM}} \approx \frac{m_{N2} \vec{\mathbf{R}}}{m_{N1} + m_{N2}} + \vec{\mathbf{R}}_{\text{CM}} \quad (2.10)$$

$$\vec{\mathbf{R}}_2 = \frac{-\sum_j^{N_e} \vec{\mathbf{r}}_j - m_{N1} \vec{\mathbf{R}}}{m_{N1} + m_{N2}} + \vec{\mathbf{R}}_{\text{CM}} \approx \frac{-m_{N1} \vec{\mathbf{R}}}{m_{N1} + m_{N2}} + \vec{\mathbf{R}}_{\text{CM}} \quad (2.11)$$

The approximations on the right hands of the above two equations are fairly reasonable due to the fact that the electron mass is much smaller than that of the nuclei. Now we take the approximated position vectors of the two nuclei in Eqs. (2.10-2.11) and the position vectors of the electrons in Eq. (2.7) into Eq. (2.3), together with the relations

$$\begin{aligned} \nabla_{\vec{\mathbf{R}}_1} &= \frac{\partial \vec{\mathbf{R}}}{\partial \vec{\mathbf{R}}_1} \nabla_{\vec{\mathbf{R}}} + \frac{\partial \vec{\mathbf{R}}_{\text{CM}}}{\partial \vec{\mathbf{R}}_1} \nabla_{\vec{\mathbf{R}}_{\text{CM}}} + \sum_j \frac{\partial \vec{\mathbf{r}}_j}{\partial \vec{\mathbf{R}}_1} \nabla_{\vec{\mathbf{r}}_j} \\ &= \nabla_{\vec{\mathbf{R}}} + \frac{m_{N1}}{m_{N1} + m_{N2} + N_e} (\nabla_{\vec{\mathbf{R}}_{\text{CM}}} - \sum_j \nabla_{\vec{\mathbf{r}}_j}), \end{aligned} \quad (2.12)$$

$$\begin{aligned} \nabla_{\vec{\mathbf{R}}_2} &= \frac{\partial \vec{\mathbf{R}}}{\partial \vec{\mathbf{R}}_2} \nabla_{\vec{\mathbf{R}}} + \frac{\partial \vec{\mathbf{R}}_{\text{CM}}}{\partial \vec{\mathbf{R}}_2} \nabla_{\vec{\mathbf{R}}_{\text{CM}}} + \sum_j \frac{\partial \vec{\mathbf{r}}_j}{\partial \vec{\mathbf{R}}_2} \nabla_{\vec{\mathbf{r}}_j} \\ &= -\nabla_{\vec{\mathbf{R}}} + \frac{m_{N2}}{m_{N1} + m_{N2} + N_e} (\nabla_{\vec{\mathbf{R}}_{\text{CM}}} - \sum_j \nabla_{\vec{\mathbf{r}}_j}), \end{aligned} \quad (2.13)$$

and

$$\begin{aligned}
 \nabla_{\vec{r}_j} &= \frac{\partial \vec{r}_j}{\partial \vec{r}_j} \nabla_{\vec{r}_j} + \sum_{k \neq j}^{N_e} \frac{\partial \vec{r}_k}{\partial \vec{r}_j} \nabla_{\vec{r}_k} + \frac{\partial \vec{R}_{\text{CM}}}{\partial \vec{r}_j} \nabla_{\vec{R}_{\text{CM}}} \\
 &= \nabla_{\vec{r}_j} - \sum_k^{N_e} \frac{1}{m_{\text{N1}} + m_{\text{N2}} + N_e} \nabla_{\vec{r}_k} + \frac{1}{m_{\text{N1}} + m_{\text{N2}} + N_e} \nabla_{\vec{R}_{\text{CM}}},
 \end{aligned} \tag{2.14}$$

we can rewrite the Hamiltonian for a diatomic molecule with  $N_e$  electrons as a combination of the Hamiltonian for the center of mass  $H_{\text{CM}}(t)$  and the Hamiltonian describing the relative motion  $H(t)$ , i.e.,

$$H_{\text{total}}(t) = H_{\text{CM}}(t) + H(t) = H_{\text{CM}}(t) + T_{\text{N}} + T_{\text{e}} + V_{\text{N}} + V_{\text{e}} + V_{\text{Ne}} + V_{\text{mp}} + V_{\text{L}}(t). \tag{2.15}$$

In the above equation,  $T_{\text{N}}$  ( $T_{\text{e}}$ ) is the kinetic energy operator of the reduced nuclei (electrons),  $V_{\text{N}}$  ( $V_{\text{e}}$ ) is the Coulomb interaction between the nuclei (electrons),  $V_{\text{Ne}}$  is the Coulomb interaction between the nuclei and electrons,  $V_{\text{mp}}$  is the mass polarization term and  $V_{\text{L}}(t)$  is the laser-molecular interaction in the center of mass frame. The expressions for these operators in Eq. (2.15) can be found in the following,

$$H_{\text{CM}}(t) = -\frac{i \nabla_{\vec{R}_{\text{CM}}}^2}{2(m_{\text{N1}} + m_{\text{N2}} + N_e)} + \sum_j^{N_e} (N_e - Z_1 - Z_2) \vec{F}(t) \cdot \vec{R}_{\text{CM}} \tag{2.16}$$

$$T_{\text{N}} = -i \frac{\nabla_{\vec{R}}^2}{2\mu}, \quad T_{\text{e}} = \sum_j^{N_e} -i \frac{\nabla_{\vec{r}_j}^2}{2m_{\text{e}}} \tag{2.17}$$

$$V_{\text{N}} = \frac{Z_1 Z_2}{R}, \quad V_{\text{e}} = \sum_{j,k < j} \frac{1}{|\vec{r}_j - \vec{r}_k|} \tag{2.18}$$

$$V_{\text{Ne}} = \sum_j \frac{Z_1}{\left| \frac{m_{\text{N2}} \vec{R}}{m_{\text{N1}} + m_{\text{N2}}} - \vec{r}_j \right|} + \sum_j \frac{Z_2}{\left| \frac{m_{\text{N1}} \vec{R}}{m_{\text{N1}} + m_{\text{N2}}} + \vec{r}_j \right|} \tag{2.19}$$

$$V_{\text{mp}} = \sum_{j,k \neq j} \frac{\nabla_{\vec{r}_j} \cdot \nabla_{\vec{r}_k}}{2(m_{\text{N1}} + m_{\text{N2}} + N_e)} \tag{2.20}$$

$$V_{\text{L}}(t) = \vec{F}(t) \cdot \left[ \sum_j \vec{r}_j \left( 1 + \frac{Z_1 + Z_2}{m_{\text{N1}} + m_{\text{N2}}} \right) - \frac{Z_1 m_{\text{N2}} - Z_2 m_{\text{N1}}}{m_{\text{N1}} + m_{\text{N2}}} \vec{R} \right] \tag{2.21}$$

with

$$\mu = \frac{m_{N1}m_{N2}}{m_{N1} + m_{N2}}, \quad m_e = \frac{m_{N1} + m_{N2} + N_e}{m_{N1} + m_{N2} + N_e - 1}. \quad (2.22)$$

The mass polarization term  $V_{mp}$ , which is purely dependent on the electronic coordinates, is usually neglected because its denominator is much larger than that of the electronic kinetic energy operator  $T_e$ . Thus, it is reasonable to only include the other six terms of the Hamiltonian for the relative motion, i.e.,  $H(t) = T_N + T_e + V_N + V_e + V_{Ne} + V_L(t)$ . The above equations altogether shows clearly to us that the Hamiltonian for the center of mass  $H_{CM}$  is only dependent on the position vector  $\vec{R}_{CM}$ , while the Hamiltonian for the relative motion  $H(t)$  has nothing to do with  $\vec{R}_{CM}$ . Thus, the total wave function  $|\Psi_{total}(t)\rangle$  can be written as a tensor product of the wave function for the center of mass  $|\Psi_{CM}(t)\rangle$  and the wave function for the relative motion  $|\Psi(t)\rangle$ , i.e.,

$$|\Psi_{total}(t)\rangle = |\Psi_{CM}(t)\rangle \otimes |\Psi(t)\rangle. \quad (2.23)$$

The center of mass mimics a particle with mass  $m_{N1} + m_{N2} + N_e$  and charge  $N_e - Z_1 - Z_2$  moving in the external field  $F(t)$ . Its motion does not affect the relative motion of the system. As a result, to study the dynamics in a molecule, we can directly take the Hamiltonian describing the relative motion  $H(t)$ .

## 2.3 Time-independent Schrödinger equation for the electronic Hamiltonian

Now that we have obtained the molecular Hamiltonian  $H(t)$ , the next step is to solve the corresponding TDSE, i.e.,

$$i|\dot{\Psi}(t)\rangle = H(t)|\Psi(t)\rangle. \quad (2.24)$$

Taking use of the fact that the electronic dynamics is usually much faster than the nuclear dynamics, we can separate the nuclear and electronic motion by applying the Born-Oppenheimer approximation



via using the following ansatz

$$|\Psi(t)\rangle = \sum_m |\chi_m(t)\rangle \otimes |\psi_{R,m}^{\text{el}}\rangle = \sum_m \int d\vec{R} \chi_m(\vec{R}, t) |\psi_{R,m}^{\text{el}}\rangle \otimes |\vec{R}\rangle, \quad (2.25)$$

where the completeness relation  $\hat{1} = \int d\vec{R} |\vec{R}\rangle \langle \vec{R}|$  is utilized and  $\chi_m(\vec{R}, t) = \langle \vec{R} | \chi_m(t) \rangle$  is the nuclear wave function when the electronic state is  $|\psi_{R,m}^{\text{el}}\rangle$ . The electronic wave functions can be obtained by solving the time-independent Schrödinger equation for the field-free electronic Hamiltonian  $H_{\text{el}}$ , i.e.,

$$H_{\text{el}} |\psi_{R,m}^{\text{el}}\rangle = E_m(\vec{R}) |\psi_{R,m}^{\text{el}}\rangle, \quad (2.26)$$

with  $H_{\text{el}} = T_e + V_N + V_e + V_{\text{Ne}}$ . We note that the electronic Hamiltonian and its corresponding eigenfunctions  $|\psi_{R,m}^{\text{el}}\rangle$  and eigenvalues  $E_m$  all have a parametric dependence on the internuclear separation vectors  $\vec{R}$ . For a given  $m$ , different internuclear separation vectors would result in different  $E_m(\vec{R})$  values, which eventually form an energy surface. We will show in the following section that the energy surfaces are indeed the potential energy surfaces where the nuclei move on.

## 2.4 Time-dependent Schrödinger equation for the nuclear motion

In this section, we will focus on obtaining the evolution of time-dependent nuclear wave functions  $\chi_m(\vec{R}, t)$ . After first taking Eq. (2.25) into the TDSE in Eq. (2.24) and then projecting both sides on the state  $\langle \psi_{R,m}^{\text{el}} | \otimes \langle \vec{R} |$ , we obtain the TDSE for the nuclear motion, i.e.,

$$\begin{aligned} i\dot{\chi}_m(\vec{R}, t) &= \left(-\frac{\nabla_{\vec{R}}^2}{2\mu} + E_m(\vec{R})\right) \chi_m(\vec{R}, t) \\ &+ \sum_{j \neq m} \langle \psi_{R,m}^{\text{el}} | V_L(t) | \psi_{R,j}^{\text{el}} \rangle \chi_j(\vec{R}, t) \\ &- \sum_j \langle \psi_{R,m}^{\text{el}} | \frac{\nabla_{\vec{R}}^2}{2\mu} | \psi_{R,j}^{\text{el}} \rangle \chi_j(\vec{R}, t) \\ &- \frac{1}{\mu} \langle \psi_{R,m}^{\text{el}} | \nabla_{\vec{R}} | \psi_{R,j}^{\text{el}} \rangle \nabla_{\vec{R}} \chi_j(\vec{R}, t). \end{aligned} \quad (2.27)$$

Now it is time to implement the adiabatic approximation to simplify the above equation by neglecting the last two vibronic coupling terms on the right side of the equation, i.e.,

$$i\dot{\chi}_m(\vec{\mathbf{R}}, t) = \left(-\frac{\nabla_{\vec{\mathbf{R}}}^2}{2\mu} + E_m(\vec{\mathbf{R}})\right)\chi_m(\vec{\mathbf{R}}, t) + \sum_{j \neq m} \langle \psi_{R,m}^{\text{el}} | V_L(t) | \psi_{R,j}^{\text{el}} \rangle \chi_j(\vec{\mathbf{R}}, t). \quad (2.28)$$

The adiabatic approximation is adopted throughout this thesis because we do not pay attention to physics near avoided crossings, where this approximation breaks down. We note that for a homonuclear diatomic molecule, the laser-molecular interaction operator is as simple as  $V_L(t) = \beta \vec{F}(t) \cdot \sum_j \mathbf{r}_k$  according to Eq. (2.21) with  $\beta = 1 + \frac{Z_1 + Z_2}{m_{N_1} + m_{N_2}}$ .

We can see from Eq (2.28) that the nuclear wave packet  $\chi_m(\vec{\mathbf{R}}, t)$  moves along its potential energy surfaces  $E_m(\vec{\mathbf{R}})$  accompanied with laser-induced couplings with the other electronic states. In principle, one should include the electronic states as many as possible to obtain the nuclear dynamics as accurate as possible. This means that one has to take many calculation resources to solve a huge number of coupled equations according to Eq. (2.28). In this thesis, we take the assumption that the molecules are rotationally frozen and the laser polarization direction is parallel to the molecular axis. Thus, the three-dimensional coupled equations in Eq. (2.28) will be reduced to one-dimensional by replacing the internuclear separation vector  $\vec{\mathbf{R}}$  by the scalar  $R$ . Besides, the potential energy surfaces are reduced to potential energy curves.

In this thesis, we are concerning about nuclear dynamics following electronic excitation and ionization in molecules. When the ionization occurs, a large number of continuum electronic states with continuous eigenenergies  $E_m(R) + \epsilon$  would be populated. Here  $\epsilon$  is the energy of the continuum electron and  $E_m(R)$  is the energy of the  $m$ th electronic state in the remaining ion. Thus, the potential energy curves for the continuum electronic states converging to the same  $m$ th electronic state in the remaining ion are parallel to the potential energy curve for the  $m$ th electronic state. It is an acceptable approximation to treat the evolution of the nuclear wave packets along the potential energy curves for the continuum states converging to a given ionic state as an effective nuclear wave packet evolving along the potential energy

## 2.4. Time-dependent Schrödinger equation for the nuclear motion

---

curve for the ionic state. This simplification, as we shown in the next chapter, is implemented by the MCWP approach where the nuclear dynamics is main concern.



---

# the Monte Carlo wave packet approach

In this chapter, we will present a thorough discussion of the MCWP approach. This method is developed to study multiple ionization of small molecules. It treats ionization as a decay process by phenomenologically introducing a non-Hermitian term into the system Hamiltonian. We will start this chapter by presenting to readers the equivalence of the MCWP method with the master equations.

## 3.1 Equivalence with the master equation

We can see from the previous chapter that the Hamiltonian  $H(t)$  for a molecule is Hermitian, so is the electronic Hamiltonian  $H_{\text{el}}$ . Thus, solving the TISE for the electronic Hamiltonian will result in real eigenvalues  $E_m(\vec{\mathbf{R}})$  for the eigenstates  $|\phi_{R,m}^{\text{el}}\rangle$ . Non-Hermitian Hamiltonian, however, would lead to complex eigenvalues for the eigenstates, where the real parts correspond to the eigenenergies for the eigenstates and the imaginary parts are related to the decay rates of the eigenstates. Thus, the complex eigenenergy representation is usually used to obtain the lifetimes or decay rates of unstable states. These states have a finite lifetime due to spontaneous relaxation processes such as spontaneous emission and autoionization. Now we generalize

the concept of instability to the states experiencing non-spontaneous decay processes, e.g., ionization induced by laser. Thus, in this thesis, for the considered states which undergo laser-induced ionization, their eigenenergies can be also constructed by complex numbers, i.e.,  $E'_m(\vec{\mathbf{R}}) = E_m(\vec{\mathbf{R}}) - \frac{i}{2}\Gamma_m(\vec{\mathbf{R}})$ , where  $\Gamma_m(\vec{\mathbf{R}})$  are the  $\vec{\mathbf{R}}$ - and state-dependent ionization rates. These complex eigenenergies indicate a new electronic Hamiltonian, i.e.,

$$H'_{\text{el}} = H_{\text{el}} - \frac{i}{2} \sum_m \int d\vec{\mathbf{R}} \Gamma_m(\vec{\mathbf{R}}) |\psi_{R,m}^{\text{el}}\rangle \langle \psi_{R,m}^{\text{el}}| \otimes |\vec{\mathbf{R}}\rangle \langle \vec{\mathbf{R}}|, \quad (3.1)$$

where the non-Hermitian term in Eq. (3.1) describes the laser-induced ionization from the involved bound electronic states  $|\psi_{R,m}^{\text{el}}\rangle$ . We note that the laser-induced ionization only accounts for the couplings between the bound and the continuum electronic states. To describe the coherent couplings between the bound electronic states (couplings between continuum states are neglected), we remain the use of the laser-molecule interaction operator  $V_L(t)$ . The new electronic Hamiltonian in Eq. (3.1), the nuclear kinetic operator  $T_N$  and the laser-molecule interaction operator  $V_L(t)$  altogether constitute a new non-Hermitian Hamiltonian  $H'(t)$ , which is the starting point of the MCWP approach, i.e.,

$$\begin{aligned} H'(t) &= T_N + H'_{\text{el}} + V_L(t) \\ &= H(t) - \frac{i}{2} \sum_m \int d\vec{\mathbf{R}} \Gamma_m(\vec{\mathbf{R}}) |\psi_{R,m}^{\text{el}}\rangle \langle \psi_{R,m}^{\text{el}}| \otimes |\vec{\mathbf{R}}\rangle \langle \vec{\mathbf{R}}| \\ &= H(t) - \frac{i}{2} \sum_m C_m^\dagger C_m. \end{aligned} \quad (3.2)$$

In the above equation, we rewrite the non-Hermitian term by introducing the quantum jump operators  $C_m$ , which specify the transitions from the  $|\psi_{R,m}^{\text{el}}\rangle$  states in a given charge state to the  $|\psi_{R,n}^{\text{el}}\rangle$  states in the charge state with an electron less. The jump operators may be different for different ionization mechanisms. In this chapter, the jump operators for tunneling ionization are expressed as

$$C_m = \int d\vec{\mathbf{R}} \sqrt{\Gamma_m(\vec{\mathbf{R}})} \sum_n c_n |\psi_{R,n}^{\text{el}}\rangle \langle \psi_{R,m}^{\text{el}}| \otimes |\vec{\mathbf{R}}\rangle \langle \vec{\mathbf{R}}|. \quad (3.3)$$

A sum over  $n$  in Eq. (3.3) means the final state following tunnel ionization by the strong external field is a coherent superposition of the

electronic states in the charge state with one electron less. For many cases, only including one electronic state in the charge state with one electron less in Eq. (3.3) is a good approximation, i.e.,  $n = 1$  and  $c_n = 1$ . We note that the tunneling ionization rates of molecules are not only dependent on the internuclear distances but also on the instantaneous external field. Thus, the tunneling ionization rates  $\Gamma_m(\vec{R})$  are time-dependent.

The explicit operations of the MCWP approach at each time step by using the stochastic sampling method are as follows:

1. Propagate the state  $|\Psi(t)\rangle$  described by Eq. (2.25) using the small-time evolution operator  $U(t + \Delta t, t) = \exp(-H'(t)\Delta t)$ , i.e,

$$|\Psi(t + \Delta t)\rangle = U(t + \Delta t, t)|\Psi(t)\rangle. \quad (3.4)$$

Here we choose a very small time step  $\Delta t$  so that  $H'(t)$  can be regarded as a constant within this small time interval.

2. Calculate the drop in the probability after a time step  $\Delta t$ , i.e.,

$$\begin{aligned} dP &= \langle \Psi(t) | \Psi(t) \rangle - \langle \Psi(t + \Delta t) | \Psi(t + \Delta t) \rangle \\ &= \sum_m dP_m \approx \sum_m \langle \Psi(t) | C_m^\dagger C_m | \Psi(t) \rangle \Delta t, \end{aligned} \quad (3.5)$$

where the above approximation is to the first order of  $\Delta t$ .

3. Determine the quantum jump occurs or not by comparing  $dP$  with a random number  $\epsilon$ . If  $dP$  is smaller than  $\epsilon$ , the jump can not occur and the system remains in the following state

$$|\Psi(t + \Delta t)\rangle = \frac{|\Psi(t + \Delta t)\rangle}{\sqrt{(1 - dP)}} = \frac{U(t + \Delta t)|\Psi(t)\rangle}{\sqrt{(1 - dP)}}. \quad (3.6)$$

Otherwise, the jump occurs and the new state is

$$|\Psi(t + \Delta t)\rangle = \frac{C_m |\Psi(t)\rangle}{\sqrt{dP_m / \Delta t}}, \quad (3.7)$$

where the choice of the  $m$ th channel above depends on a comparison of a new random number  $\eta$  with the branching ratio  $dP_m / dP$ . For example, for the case of two states, i.e.,  $m = 1, 2$ , if  $\eta$  is smaller than  $dP_1 / dP$ , then the jump occurs from  $|\psi_{R,1}^{\text{el}}\rangle$  state, otherwise, from the  $|\psi_{R,2}^{\text{el}}\rangle$  state.

4. Continue to the next time step from point 1.

The propagation from the initial state at the beginning to the final state at the end of the propagation time is called a realization. We should include many realizations and average over them to obtain the physical evolution of a system.

We will show in the following the equivalence of the MCWP approach with the master equation in the Lindblad form for a dissipative process. The density operator at  $t + \Delta t$  is  $\rho(t + \Delta t) = |\Psi(t + \Delta t)\rangle\langle\Psi(t + \Delta t)|$ . Statistically, the average value of this density operator can be expressed as

$$\begin{aligned} \bar{\rho}(t + \Delta t) &= (1 - dP) \frac{|\Psi(t + \Delta t)\rangle\langle\Psi(t + \Delta t)|}{1 - dP} \\ &+ \sum_m dP_m \frac{C_m |\Psi(t)\rangle\langle\Psi(t)| C_m^\dagger}{dP_m / \Delta t}, \end{aligned} \quad (3.8)$$

with the knowledge that there is a probability of  $(1 - dP)$  that the system is in the  $\frac{|\Psi(t + \Delta t)\rangle}{\sqrt{1 - dP}}$  state and there is a probability of  $dP_m$  that the state is in the  $\frac{C_m |\Psi(t)\rangle}{\sqrt{dP_m \Delta t}}$  state. By taking Eq. (3.6) into Eq. (3.8), we can obtain the following equation after neglecting the  $(\Delta t)^2$  term, i.e.,

$$\begin{aligned} \bar{\rho}(t + \Delta t) &= (1 - iH(t)\Delta t - \frac{1}{2} \sum_m C_m^\dagger C_m \Delta t) \bar{\rho}(t) \\ &\times (1 + iH(t)\Delta t - \frac{1}{2} C_m^\dagger C_m \Delta t) + \Delta t C_m \bar{\rho}(t) C_m^\dagger \\ &= \bar{\rho}(t) - i[H(t), \bar{\rho}(t)]\Delta t - \frac{1}{2} \{\bar{\rho}(t), C_m^\dagger C_m\} \Delta t \\ &+ \Delta t C_m \bar{\rho}(t) C_m^\dagger. \end{aligned} \quad (3.9)$$

Taking  $\dot{\bar{\rho}}(t) = \frac{\bar{\rho}(t + \Delta t) - \bar{\rho}(t)}{\Delta t}$  into the above equation, we can obtain the master equation in the Lindblad form

$$i\dot{\bar{\rho}} = [\bar{\rho}, H(t)] - \frac{i}{2} \{\bar{\rho}, C_m^\dagger C_m\} + iC_m \bar{\rho} C_m^\dagger. \quad (3.10)$$



## 3.2 Calculation strategy for the deterministic sampling method

In the MCWP approach, the evolution equation for the nuclear wave functions in each charge state can be similarly obtained by projecting the TDSE of the non-Hermitian Hamiltonian  $H'(t)$  on the  $\langle \psi_{R,m}^{\text{el}} | \otimes \langle \vec{R} |$  state. After applying the adiabatic approximation, the obtained equation for the nuclear motion is similar to Eq. (2.28) except that  $E_m(\vec{R})$  in Eq. (2.28) is replaced by  $E_m(R) - \frac{i}{2}\Gamma_m(R, t)$ , i.e.,

$$\begin{aligned}
 i\dot{\chi}_m(R, t) &= \left(-\frac{\nabla_R^2}{2\mu} + E_m(R) - \frac{i}{2}\Gamma_m(R, t)\right)\chi_m(R, t) \\
 &+ \sum_{j \neq m} \langle \psi_{R,m}^{\text{el}} | V_L(t) | \psi_{R,j}^{\text{el}} \rangle \chi_j(R, t). \quad (3.11)
 \end{aligned}$$

In the previous section, we have discussed the procedures for the implementation of the MCWP approach when the stochastic sampling method is applied. An alternative is to apply a much more simplified deterministic method [63]. Here are the explicit procedures for obtaining the nuclear KER spectrum following double ionization of a diatomic molecule by using the deterministic sample strategy:

1. Propagate the nuclear wave packet along the potential energy curves for the electronic states involved according to Eq. (3.11) in the neutral molecule. The probability in the neutral charge state  $P_n(t)$  is decreasing over time because of ionization. The first jumps are assumed to occur at every time step. The probability for a jump occurring at a given time step is the ionization probability within a small time interval  $\Delta t$ , i.e.,

$$P_1(t) = P_n(t) - P_n(t + \Delta t) = \sum_m \int dR |\chi_m^n(R, t)|^2 - |\chi_m^n(R, t + \Delta t)|^2, \quad (3.12)$$

where  $\chi_m^n(R, t)$  is the nuclear wave packet evolving along the potential energy curve for the  $|\psi_{R,m}^{\text{el},n}\rangle$  state.

2. When the first ionization occurs at  $t_1$ , the initial nuclear wave packet along the potential energy curve for the  $|\psi_{R,k}^{\text{el},s}\rangle$  state in

the singly ionized molecule can be obtained by from Eq. (3.7)

$$\chi_k^s(R, t_1) = N c_k \sqrt{\Gamma_m^n(R, t_1)} \chi_m^n(R, t_1), \quad (3.13)$$

where  $N$  is introduced to normalize total wave function in the singly ionized system, i.e.,  $\sum_k \int dR |\chi_k^s(R, t_1)|^2 = 1$ , and  $\Gamma_m^n(R, t_1)$  is the  $R$ -dependent ionization rates from the  $|\psi_{R,m}^{\text{el},n}\rangle$  state in the neutral molecule to the singly charged ion at  $t_1$ . The appearance of  $c_k$  in Eq. (3.13) comes from the jump operator  $C_m$  in Eq. (3.3). When several electronic states in the neutral molecule are involved, there are several first ionization pathways since the first ionization can take place from each state in the neutral molecule. The relative probability or branch ratio for a given pathway whose ionization takes place from the  $|\psi_{R,m}^{\text{el},n}\rangle$  state is

$$P_{1m}(t_1) = \frac{\int dR \Gamma_m^n(R, t_1) |\chi_m^n(R, t_1)|^2}{\sum_m \int dR \Gamma_m^n(R, t_1) |\chi_m^n(R, t_1)|^2}. \quad (3.14)$$

Thus, the probability for the first jump occurring at  $t_1$  from the  $|\psi_{R,m}^{\text{el},n}\rangle$  state is  $P_1(t_1) \times P_{1m}(t_1)$ .

3. After the first jump at  $t_1$ , the nuclear wave packet would evolve along the potential energy curves for the electronic states in the singly charged ion according to Eq. (3.11) by using the initial nuclear wave packet in Eq. (3.13) as the initial condition. The probability in the singly charged ion  $P_s(t)$  is decreasing over time due to ionization. The probabilities for the second jumps occurring at  $t_2$  are similarly obtained by

$$P_2(t_2) = P_s(t_2) - P_s(t_2 + \Delta t) = \sum_k \int dR |\chi_k^s(R, t_2)|^2 - |\chi_k^s(R, t_2 + \Delta t)|^2. \quad (3.15)$$

The initial nuclear wave packet  $\chi_j^d(R, t_2)$  along the potential energy curve for the  $|\psi_{R,j}^{\text{el},d}\rangle$  state at  $t_2$  in the doubly ionized molecule is described by

$$\chi_j^d(R, t_2) = M c_j \sqrt{\Gamma_k^s(R, t_2)} \chi_k^s(R, t_2). \quad (3.16)$$

In the above equation, a similar constant  $M$  is introduced to make the total wave function normalized and  $\Gamma_k^s(R, t_2)$  represents

the ionization rates from the  $|\psi_{R,k}^{\text{el},s}\rangle$  in the singly ionized molecule to the doubly ionized system. Similarly, when there are several second jump pathways, the relative probability or branch ratio for the pathway whose ionization takes place from the  $|\psi_{R,k}^{\text{el},s}\rangle$  state is

$$P_{2j}(t_2) = \frac{\int dR \Gamma_k^s(R, t_2) |\chi_k^s(R, t_2)|^2}{\sum_k \int dR \Gamma_k^s(R, t_2) |\chi_k^s(R, t_2)|^2}. \quad (3.17)$$

Thus, the probability for the second jump occurring at  $t_2$  via from the  $|\psi_{R,k}^{\text{el},s}\rangle$  state are  $P_2(t_2) \times P_{2m}(t_2)$ .

4. Once the second ionization takes place at  $t_2$ , the nuclear wave packet would propagate along the potential energy curves for the states in the doubly ionized system according to Eq. (3.11) by using the nuclear wave packet in Eq. (3.16) as the initial condition. The nuclear wave packets in the doubly ionized molecule at the end of laser pulse, i.e.,  $\chi_j^d(R, t_e)$  with  $j = 1, 2, \dots$ , are projected on the eigenstates  $\chi_{E,j}(R)$  of the potential energy curves for the  $|\psi_{R,j}^{\text{el},d}\rangle$  states to obtain the nuclear KER spectrum for a deterministic realization, i.e.,

$$p_E(m, t_1, k, t_2) = \sum_j \left| \int dR \chi_{E,j}(R) \chi_j^d(R, t_e) \right|^2. \quad (3.18)$$

The final nuclear KER spectra can be obtained by summing over the contributions from the realizations, also called trajectories, at different first and second jump times, and from different first and second jump pathways, i.e.,

$$P_E = \sum_{m, t_1, k, t_2} P_1(t_1) P_{1m}(t_1) P_2(t_2) P_{2k}(t_2) p_E(m, t_1, k, t_2). \quad (3.19)$$

### 3.3 Approximations and simplifications

We have adopted a series of approximations and simplifications in the MCWP approach. We first summarize the approximations in the following:

1. the **dipole approximation**, we have applied the dipole approximation by using the laser-molecule interaction operator in

Eq. (2.4). The dependence of the external field on the spatial coordinates can be neglected when the scale of small molecules is much smaller than the wavelength of the applied laser pulse.

2. the **Born-Oppenheimer approximation**, we have applied this approximation to assume the total wave function as a product of the nuclear wave function and electronic wave functions, see Eq. (2.25). This is reasonable when the electronic dynamics is much faster than the nuclear dynamics.
3. the **adiabatic approximation**, this means that we ignore the change of the electronic states on the nuclear motion, see Eq. (2.28). The electronic states remain the same order. For example, if the system is initially in the ground electronic state at a given internuclear distance, when the nuclei move to another internuclear distance, the electronic state is still the ground state of the new electronic Hamiltonian.
4. the **Born-Markov approximation**, when the electron is removed from the molecule, it is immediately absorbed by the (imaginary) detector so that rescattering of the electron by the external field is not included in our simulation. The unidirectional loss of electrons to the surroundings is described by the non-Hermitian term in the Hamiltonian in Eq. (3.2).
5. the **quasi-static approximation** in obtaining the tunneling ionization rates, tunneling ionization rates in a slowly oscillating field is assumed to be dependent on the instantaneous field strength.

The simplifications are summarized as follows:

1. neglecting the mass-polarization term in the Hamiltonian, this term is much smaller than the electronic kinetic energy operator and thus it can be neglected, see Eq. (2.15).
2. assuming the molecules are rotationally frozen, this assumption is reasonable since the rotational motion of molecules are usually much slower than the vibrational motion. It greatly simplifies the problem by reducing the three dimensional  $\vec{R}$  to the scalar  $R$ .

3. assuming the laser polarization direction parallel to the molecular axis throughout this thesis

## 3.4 Applications of the MCWP approach

The MCWP approach was applied to study dissociative double ionization of small diatomic molecules such as  $\text{H}_2$  interacting with laser pulses at visible or near-infrared wavelengths [53–55] and  $\text{O}_2$  interacting with UV pulses [56]. We have extended this method to study dissociative double ionization of  $\text{H}_2$  interacting with intense mid-infrared laser pulses [60]. In addition, we have applied this method to study the nuclear dynamics in the singly excited states in  $\text{H}_2$  by using XUV-pump-IR-probe spectroscopy [61]. This method can be further extended to study triple ionization of small molecules, which is beyond the capacities of many quantum methods, as shown in Chapter 5. We can easily apply this method to study multiple ionization in other diatomic molecules when the potential energy curves, electronic ionization rates and dipole moment functions are available in literature.

The MCWP approach is appropriate to simulate multiple ionization of small molecules in the cost of lack of information for the electrons removed from the molecular system. It provides a unique possibility to conduct a trajectory analysis of the features in the nuclear KER spectrum to obtain the origins of the features.



---

# Dissociative single or double ionization of H<sub>2</sub>

In this chapter, we apply the MCWP approach to simulate dissociative single or double ionization of H<sub>2</sub> when exposed intense laser pulses. Before we present the nuclear KER spectra following double ionization of H<sub>2</sub> at different laser parameters, we first explicitly describe how to obtain the individual trajectories by the MCWP method.

## 4.1 Implementation of the MCWP method to double ionization of H<sub>2</sub>

When we consider double ionization of H<sub>2</sub>, three charge states are involved, i.e., H<sub>2</sub>, H<sub>2</sub><sup>+</sup> and H<sub>2</sub><sup>++</sup>: the first ionization takes the neutral H<sub>2</sub> to the singly charged H<sub>2</sub><sup>+</sup> and the second ionization takes H<sub>2</sub><sup>+</sup> to the doubly charged H<sub>2</sub><sup>++</sup>. We first obtain the evolution of the nuclear packets in the neutral H<sub>2</sub> by solving Eq. (3.11). The probability in H<sub>2</sub> decreases over time due to laser-induced ionization. Different from the deterministic method discussed in Chapter 3, where the ionization is assumed to occur at every time step, we attempt to adopt a smarter sampling method to reduce the computational cost: we take advantage of the gradually decreased probability in H<sub>2</sub> as a function time to pick up the first jumps. Here are the methods for different cases:

1. If the ionization probabilities within a time interval  $\Delta t$  around the field extrema are locally largest. The jumps are assumed to occur at the instants of the field extrema. They jumps are evenly separated in time by half a laser cycle and their probabilities are represented by the ionization probabilities within a small time interval  $\Delta t$  according to Eq. (3.12). This sampling strategy to gather the first jumps was applied in Ref. [53–55, 60].
2. If the locally largest ionization probabilities within a time interval  $\Delta t$  do not appear at the instants for the field extrema. The jumps are still assumed to occur at the instants with locally largest ionization probabilities within a small time interval. Since these jump times are not necessarily equally separated in time, it is unfair to treat their probabilities as the ionization probabilities within a time interval  $\Delta t$  for all the jump. For a given jump occurring at  $t_1$ , we can find the instants  $t_L$  and  $t_R$  for the two adjacent locally smallest ionization probabilities within a time interval  $\Delta t$ .  $t_L$  and  $t_R$  are left and right to  $t_1$ , respectively. The probability for the jump at  $t_1$  is taken by the sum of the ionization probabilities within a time interval  $\Delta t$  at the instants from  $t_L$  to  $t_R$ , i.e.,  $P_{\text{new}}(t_1) = \sum_{t_L}^{t_R} P_1(t)$ . This sampling method to pick up the first jumps was applied in Ref. [61].
3. If the ionization probabilities within a small time interval do not dramatically change for a relatively long time, e.g., for an autoionization process, the jumps are simply assumed to occur at every several time steps. The probability for a given first jump is the ionization probability within a small time interval at that jump time.

Once the first ionization occurs, we continue to propagate the nuclear wave packets in  $H_2^+$  until the second ionization takes place. The nuclear dynamics in  $H_2^+$  is induced thus we assume the second jumps taking place at every several time steps. After the second ionization, the nuclear wave packets would propagate to large internuclear distances due to the repulsion energy of  $1/R$  between two two protons. To obtain the KER of the two protons, it is not necessary to project the nuclear wave packet in  $H_2^{++}$  at very large internuclear distances on the



#### 4.1. Implementation of the MCWP method to double ionization of $\text{H}_2$

Coulomb waves  $\chi_E(R)$  satisfying the following TISE, i.e.,

$$(T_N + \frac{1}{R})\chi_E(R) = E\chi_E(R). \quad (4.1)$$

Instead, we can project directly the normalized initial wave packet in  $\text{H}_2^{++}$  to the above Coulomb waves, since the probabilities of the individual Coulomb waves remain unchanged over time during the evolution of the nuclear wave packet in  $\text{H}_2^{++}$  according to the TDSE for the nuclear motion in  $\text{H}_2^{++}$

$$i\dot{\chi}_c(R, t) = ((T_N + \frac{1}{R}))\chi_c(R, t). \quad (4.2)$$

Summing over the contributions from the trajectories at different first and second jump times according to Eq. (3.19), we can obtain the nuclear KER spectrum following double ionization  $\text{H}_2$  interacting with intense laser pulse. In the following part, the influences of the laser parameters such as peak intensity, pulse duration, central wavelength as well as nuclear mass on the nuclear KER spectra, are investigated following double ionization of  $\text{H}_2$ .

Numerically, within charge state, we solve Eq. (3.11) by applying the split-operator method [64, 65] on the short-time propagator, i.e.,

$$\begin{aligned} U(t + \Delta t, t) &= \exp(-iT_N \frac{\Delta t}{2}) \exp(-iV(R, t + \frac{\Delta t}{2}) \Delta t) \\ &\times \exp(-iT_N \frac{\Delta t}{2}), \end{aligned} \quad (4.3)$$

with  $T_N = -\frac{1}{2\mu} \frac{d^2}{dR^2}$  and  $V(R, t) = M(R) + \beta D(R)F(t)$ . The matrix  $M(R)$  is diagonal with diagonal elements  $M_{mm}(R) = E_m(R) - \frac{i}{2}\Gamma_m(R, t)$  and the matrix elements of  $D(R)$  are the electric dipole moment functions  $D_{mj}(R) = \langle \psi_{R,m}^{\text{el}} | r | \psi_{R,j}^{\text{el}} \rangle$ .

The size of our simulation box for dissociative ionization of  $\text{H}_2$  is 40.96. The time step  $\Delta t$  is 1 and the spatial step  $\Delta R$  is 0.02. The matrix  $\exp(-iT_N \frac{\Delta t}{2})$  is diagonal in the momentum representation. Thus, the fast Fourier transformation from position to momentum and vice versa is implemented to speed up solving Eq. (3.11).

## 4.2 Nuclear KER spectra at near- and mid-IR wavelengths

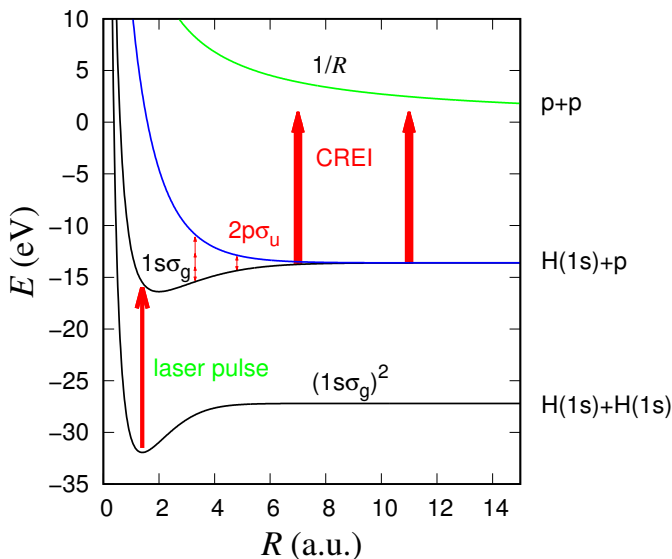


Figure 4.1: Potential energy curves involved when we consider H<sub>2</sub> interacts with laser pulses at IR wavelengths. They are the potential energy curves for the ground state in H<sub>2</sub>, for the ground  $1s\sigma_g$  and first excited  $2p\sigma_u$  states in H<sub>2</sub><sup>+</sup> and the  $1/R$  curve for the two protons in H<sub>2</sub><sup>++</sup>, respectively.

Double ionization of the hydrogen molecule by femtosecond laser pulses at the near-infrared wavelengths has been studied for over two decades [57, 66–69]. Due to the limited accessibility of the mid-infrared laser sources, the interaction of H<sub>2</sub> with laser pulses at mid-infrared wavelengths has barely been investigated [70]. Therefore, we apply the MCWP method to study dissociative double ionization of H<sub>2</sub> interacting with femtosecond mid-infrared laser pulses [60]. Laser-induced ionization by infrared wavelengths works in the tunneling ionization regime when the Keldysh parameter is smaller than 1. In H<sub>2</sub>, the first excited electronic state is well separated from the ground electronic state: the energy separation between these two states is over 10 eV in

the Franck-Condon region. Thus, laser-induced couplings between the ground state and the excited states in  $\text{H}_2$  by the IR laser pulses can be neglected. It is reasonable to only include the ground electronic state in  $\text{H}_2$  in our simulation. After tunneling ionization from the ground state in  $\text{H}_2$ , the ground and first excited states in  $\text{H}_2^+$ , i.e., the  $1s\sigma_g$  and  $2p\sigma_u$  states, can be coherently populated. Thus we can only include the  $1s\sigma_g$  and  $2p\sigma_u$  states in  $\text{H}_2^+$  in our simulation. The applied laser pulse can also induce couplings between these two states and simultaneously induce tunneling ionization from the two states leading to Coulomb explosion. In  $\text{H}_2^{++}$ , the repulsion energy between two protons is  $1/R$ . The potential energy curves for the states involved in the simulation are plotted in Fig. 4.1. The data for the potential energy curves for the electronic states in  $\text{H}_2$  and  $\text{H}_2^+$  are taken from Ref. [71]. The dipole moment functions between the  $1s\sigma_g$  and  $2p\sigma_u$  states are taken from Ref. [72]. The tunneling ionization rates from the ground state in  $\text{H}_2$  are obtained by using the weak field asymptotic theory [73, 74]. The tunneling ionization rates from the two states in  $\text{H}_2^+$  are obtained by interpolation and extrapolation of the rates available in Ref. [75]. Charge-resonance enhanced ionization (CREI) in the  $2p\sigma_u$  state in  $\text{H}_2^+$  is observed in Ref. [75], e.g., enhanced ionization at around  $R = 7$  a.u. and  $R = 11$  a.u. for a field strength of 0.04 a.u.. According to Eq. (3.7), the initial states in  $\text{H}_2^+$  can be expressed (without normalization) as  $c_g\sqrt{\Gamma_h(R, t)}\chi_g(R, t_1)|g\rangle + c_u\sqrt{\Gamma_h(R, t)}\chi_u(R, t_1)|u\rangle$ . Here  $\Gamma_h(R, t)$  is the time-dependent ionization rate from the ground state in  $\text{H}_2$ , and  $|g\rangle$  and  $|u\rangle$  denotes the  $1s\sigma_g$  and  $2p\sigma_u$  states.  $c_g$  and  $c_u$  are taken from Ref. [76]. The initial nuclear wave packet in  $\text{H}_2^{++}$  after the second jump can be easily obtained according to Eq. (3.16) by taking  $j = 1$  since there is only one state in  $\text{H}_2^{++}$ .

## Influences of laser parameters

In this section, we will investigate the influence of laser parameters on the nuclear KER spectra following double ionization of  $\text{H}_2$ . The external laser field has a Gaussian envelope and its electric field component is

$$F(t) = F_{\text{IRO}} \exp\left(-\frac{2 \ln 2(t - t_c)^2}{T_{\text{IR}}^2}\right) \times \cos(\omega_{\text{IR}}(t - t_c)),$$

where  $F_{\text{IR0}}$  is the peak field strength,  $T_{\text{IR}}$  is the pulse duration (FWHM) and  $t_c = 1.5T_{\text{IR}}$ . We present the nuclear KER spectra for laser pulses at four different wavelengths, i.e., 800, 1600, 3200 and 6400 nm, in Fig. 4.2. The pulse duration  $T_{\text{IR}}$  for the four laser pulses is fixed at 64 fs and the peak intensity of these pulses is  $6 \times 10^{13}$  W/cm<sup>2</sup> (corresponding to a field strength of  $F_{\text{IR0}} = 0.0413$ ). For all the wavelengths, we observe signal peaks at similar KER positions, i.e., KER  $\approx$  10 and 4 eV. From the simple reflection principle, i.e., KER  $\approx$  1/ $R$ , we can relate the formation of the peaks around these two KER values in the nuclear KER spectra to nuclear motion as follows:

1. the signals peaks at around 10 eV are mainly from the nuclear wave packets at around  $R = 27.2/10 = 2.72$  a.u.. This position is close to the outer turning point of the nuclear wave packets evolving along the  $1\sigma_g$  curve in  $H_2^+$  when the initial nuclear wave packet centers at around 1.4 a.u..
2. the signals peaks at around 4 eV are mainly from the nuclear wave packets at around  $R = 27.2/4 = 6.8$  a.u., which is close to the first CREI position at around  $R = 7$  a.u. in the  $2p\sigma_u$  state for the considered peak intensity.

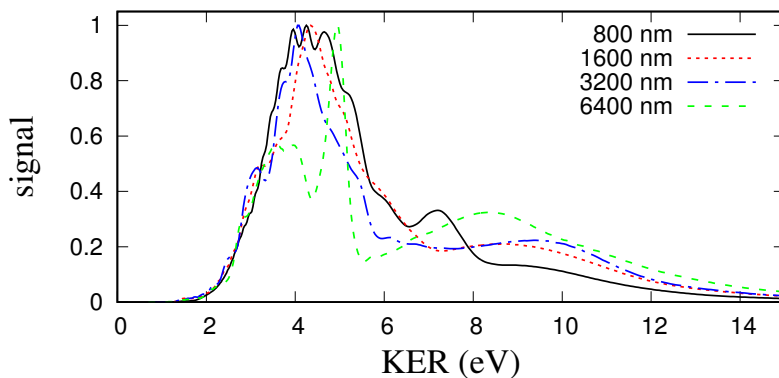


Figure 4.2: Nuclear KER spectra following double ionization of  $H_2$  interacting with laser pulses at four different wavelengths, i.e., 800, 1600, 3200 and 6400 nm. The pulse duration (FWHM) is fixed at 64 fs and the peak intensity is fixed at  $6 \times 10^{13}$  W/cm<sup>2</sup>.

We can also see from Fig. 4.2 that the relative intensities of the peaks at around 10 eV slightly increases when the wavelength is increased from 800 to 6400 nm. This feature can be understood by the fact that a smaller part of the nuclear wave packet along the  $2p\sigma_u$  curve in  $\text{H}_2^+$  can reach the first CREI position of  $R = 7$  for a longer wavelength. The one-photon resonance position between the  $1s\sigma_g$  and  $2p\sigma_u$  states in  $\text{H}_2^+$  is larger for a longer wavelength. It is beyond the outer turning point of the  $1s\sigma_g$  curve at around  $R = 3$  for the infrared wavelength. It is more unlikely for the nuclear wave packet along  $1s\sigma_g$  curve reaching the one-photon resonance position for a longer wavelength. Thus, for a longer wavelength, there is a smaller part of nuclear wave packet along the  $2p\sigma_u$  curve at around  $R = 7$ , which comes from couplings between  $1s\sigma_g$  and  $2p\sigma_u$  states in  $\text{H}_2^+$  at the one-photon resonance position.

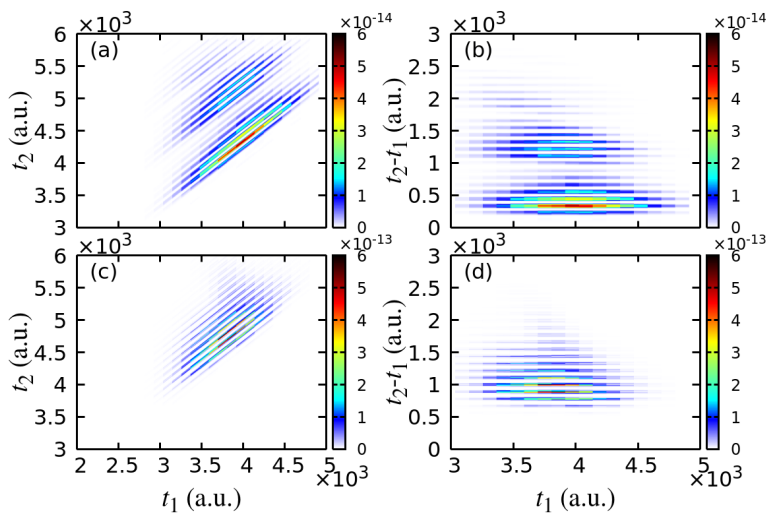


Figure 4.3: Results obtained by conducting a trajectory analysis to the peaks at around 10 and 4 eV for the 1600 nm case in Fig. 4.2. Contributions from the individual trajectories at different first and second jump times, i.e,  $t_1$  and  $t_2$ , to the peaks at around 10 eV (a) and 4 eV (c). Transformation of (a) and (c) to (b) and (d), respectively, by replacing the  $t_2$  axis with a new  $t_2 - t_1$  axis.

One unique possibility of the MCWP approach is to carry out a trajectory analysis to obtain the origin of the features of interest in the

nuclear KER spectra. A trajectory analysis to a given feature in the nuclear KERR spectrum can tell us information about the dominant trajectories including the first and second jump times, i.e.,  $t_1$  and  $t_2$ , and the states where the second jump takes place. In the following, we will conduct a trajectory analysis to the peaks at around 10 and 4 eV for the 1600 nm case in Fig. 4.2. We show the contributions (probabilities) of the individual trajectories, whose second jumps take place from the  $2p\sigma_u$  state in  $H_2^+$ , to the two peaks in Figs. 4.3(a) and (c), respectively. The much smaller contributions of the trajectories whose second jumps take place from the  $1s\sigma_g$  state in  $H_2^+$  are not presented here. In Figs. 4.3(a) and (c), the probabilities from the trajectories are distributed along titled parallel lines, each of which corresponds to an identical evolution time in  $H_2^+$ , i.e.,  $t_2 - t_1$ .

The initial nuclear wave packets in  $H_2^+$  after the first jumps are very similar in spite of different first jump times. This fact results in that the nuclear dynamics in  $H_2^+$  is mainly determined by the evolution time in  $H_2^+$ . Therefore, we make a transformation of Figs. 4.3(a) and (c) to Figs. 4.3(b) and (d), respectively, by replacing the  $t_2$  axis with  $t_2 - t_1$ . From Figs. 4.3(a) and (c), we can see that for the trajectories at a given  $t_1$ , their probabilities oscillate as a function of  $t_2$  with a period of half a laser cycle. The large (small) probability for a given trajectory originates from that its second jump taking place at instants when the instantaneous field strength is large (small) due to large (small) laser-induced ionization rates. For the trajectories at a given  $t_2$ , we do not observe a similar oscillatory behavior of the probabilities as a function  $t_1$  since the first ionization is assumed to only take place at the instants for the field extrema.

It is clearly shown in Figs. 4.3(b) and (d) that the evolution time in  $H_2^+$  for the most dominant trajectories are around  $t_2 - t_1 = 300$  and 1200 a.u. for the peak at 10 eV and around  $t_2 - t_1 = 1000$  a.u. for the peak at 4 eV. From the reflection principle, we aware that the two peaks at 10 and 4 eV mainly comes from trajectories whose nuclear wave packets evolving along the  $2p\sigma_u$  curve in  $H_2^+$  are at around  $R = 3$  and  $R = 7$  when the second jumps occur. Thus, it takes the nuclear wave packet in  $H_2^+$  about 300 a.u. to reach the internuclear positions of the outer turning point at around  $R = 3$  for the first time and about 1200 a.u. to reach the internuclear positions at around  $R = 3$  for the second time. The difference between them, i.e.,  $1200 - 300 = 900$  a.u.,

reflects that the vibrational period of the nuclear wave packet along the  $1s\sigma_g$  state in  $\text{H}_2^+$  is around 900 a.u. = 22 fs. For the peak at 4 eV, it takes about 1000 a.u. for the nuclear wave packet to reach the first CREI region at around  $R = 7$ .

We can read from Figs. 4.3(a) and (c) the information about the most dominant trajectory for the peak at 4 eV: the first jump occurs at  $t_1 = 3806$  a.u. and the second jump occurs at  $t_2 = 4719$  a.u.. For the peak at 10 eV, the information about the most dominant trajectory is that the first jump takes place at  $t_1 = 3938$  a.u. and the second jump at  $t_2 = 4231$  a.u.. The difference of the first times for these two trajectories is half a laser cycle. We present in Figs. 4.4(a) and (b) the evolution of the nuclear wave packet along the  $1s\sigma_g$  and  $2p\sigma_u$  curves in  $\text{H}_2^+$  when the first jump takes place at  $t_1 = 3806$  a.u.. In addition, we show in Figs. 4.4(c) and (d) the initial nuclear wave packets (without normalization) in  $\text{H}_2^{++}$  for the second jumps taking place from the  $\sigma_g$  and  $2p\sigma_u$  curves when the first jump occur at  $t_1 = 3806$  a.u.. We can see that the probabilities of the initial nuclear wave packets for the trajectories whose second jumps take place from the  $2p\sigma_u$  state are several order larger than that for the trajectories whose second jumps take place from the  $1s\sigma_g$  state.

We can clearly see from Fig. 4.4(a) that the vibrational period of the nuclear wave packet evolving along the  $1s\sigma_g$  curve is around 900 a.u. = 22 fs, which agrees very well to the result obtained from the above trajectory analysis. We can also see from Fig. 4.4(b) the nuclear wave packet evolving along the  $2p\sigma_u$  curve can reach around  $R = 7$  at  $t_2 = 4719$  a.u.. Due to the CREI at around  $R = 7$ , the large probabilities of the initial nuclear wave packet at around  $R = 7$  in  $\text{H}_2^{++}$  can be observed at  $t_2 = 4719$  a.u. in Fig. 4.4(d). It is the large signals at around  $R = 7$  in Fig. 4.4(d) that eventually result in the appearance of the peak at around 4 eV in the considered nuclear KER spectrum. The signals at around  $R = 3$  in Fig. 4.4(d) leads to the peak at around 10 eV in the nuclear KER spectrum.

We will investigate the influence of the pulse duration of the applied laser pulse on the nuclear KER spectra. We show the results in Fig. 4.5 for two wavelengths of 1600 nm and 6400 nm. A systematical study of the dependence on the duration for several wavelengths has been performed in a recent article [60]. From Fig. 4.5, we can observe that the nuclear KER spectrum moves to smaller KER values when

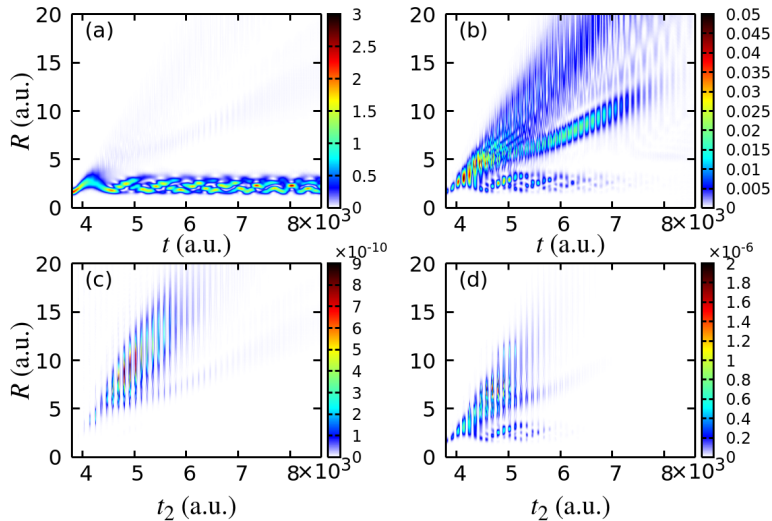


Figure 4.4: Evolution of the nuclear wave packets along the  $1s\sigma_g$  (a) and  $2p\sigma_u$  (b) curves in  $H_2^+$  when the first jump occurs at  $t_1 = 3806$  a.u.. The initial nuclear wave packets in  $H_2^{++}$  for the second jumps taking place from the  $1s\sigma_g$  (c) and  $2p\sigma_u$  (d) curves at varying second jump times when the first jump occurs at  $t_1 = 3806$  a.u..

the pulse duration is increased. A larger pulse duration can induce the ionization from  $H_2^+$  at larger internuclear distances when the nuclear wave packet evolves along the  $2p\sigma_u$  curve in  $H_2^+$ . The ionization from  $H_2^+$  at larger internuclear distances would result in signals at smaller KER values. We can also observe several peaks at similar KER positions in the nuclear KER spectra at the same wavelength in Fig. 4.5. The KER of  $H_2^{++}$  is made up of two parts: the kinetic energy obtained in  $H_2^+$  and the Coulomb repulsion energy between the two protons. The kinetic energy obtained along the  $2p\sigma_u$  curve in  $H_2^+$  is determined by the position for the one- or three- photon resonance between the two states in  $H_2^+$  and the position where the second jump takes place. The internuclear position for the one- or three- photon resonances between the two states in  $H_2^+$  is only dependent on the wavelength. For  $H_2$  interacting with relatively long pulses, there is a large probability that the second jumps take places at the CREI regions. The trajectories whose second jumps take place from the CREI regions would result in



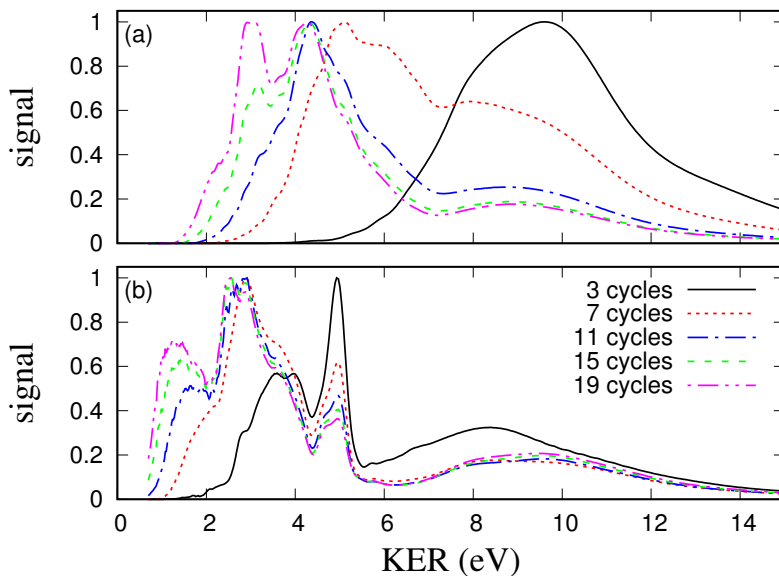


Figure 4.5: Nuclear KER spectra following double ionization of  $\text{H}_2$  when exposed to laser pulses at (a) 1600 nm and (b) 6400 nm for different pulse durations. The pulse duration (FWHM) is expressed by the number of laser cycles. The peak intensity is fixed at  $6 \times 10^{13}$   $\text{W}/\text{cm}^2$ .

signals at similar KER positions for the pulses at the same wavelength, since both the kinetic energy obtained in  $\text{H}_2^+$  and the Coulomb repulsion energy between the two protons are similar. The peaks at very low KER values, i.e., about 1.5 eV, in Fig. 4.5 results from the trajectories whose the evolution time in  $\text{H}_2^+$  is sufficient long so that large ionization at internuclear distances beyond the CREI region of  $R = 11$  can take place. A trajectory analysis of this peak has been conducted in Ref. [60]. The peaks at around and 10 eV have similar origins as we discussed before. For the 6400 nm case, the peaks at around 3 eV are from trajectories whose nuclear wave packets in  $\text{H}_2^+$  reach the second CREI position at around  $R = 11$  a.u. for the considered peak intensity.

We turn to study the influences of the peak intensity on the nuclear KER spectra. In a previous work [54],  $\text{H}_2$  interacting with 40-fs laser pulses at 800 nm with increasing peak intensity from  $0.4$  to  $0.7 \times 10^{14}$

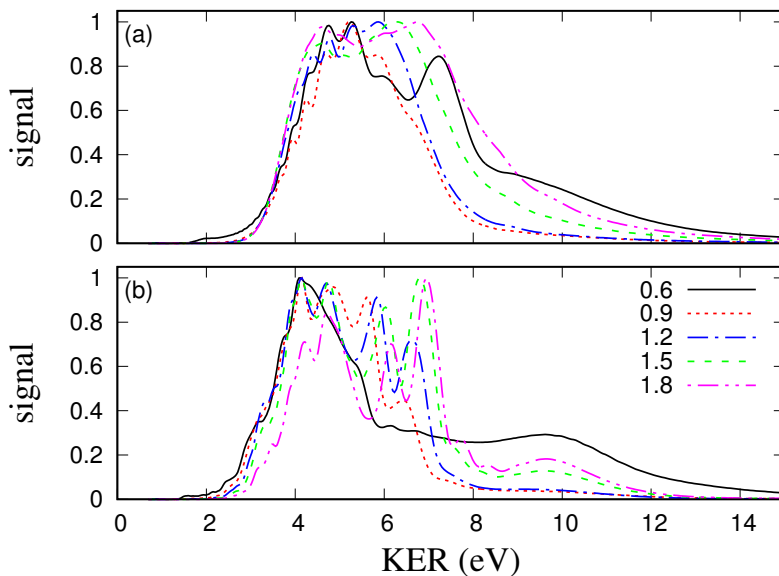


Figure 4.6: Nuclear KER spectra following double ionization of H<sub>2</sub> when exposed to laser pulses at (a) 800 nm and (b) 3200 nm with the peak intensities ranging from  $0.6$  to  $1.8 \times 10^{14}$  W/cm<sup>2</sup>. The pulse durations (FWHM) are 40 fs for the 800 nm pulses and 53 fs for the 3200 nm pulses, respectively.

W/cm<sup>2</sup> was studied by the MCWP approach. Now we extend the study of H<sub>2</sub> interacting with pulses at much larger peak intensities for the 800 nm wavelength and with pulses at a mid-IR wavelength of 3200 nm. The pulse durations for the 800 nm case is 15 laser cycles (40 fs) and for the 3200 nm case, it is 5 laser cycles (40 fs). In Ref. [54], the nuclear KER spectra move to smaller KER values when the peak intensities are increased from  $0.4$  to  $0.7 \times 10^{14}$  W/cm<sup>2</sup>. The nuclear KER spectra, however, moves oppositely, i.e., to larger KER values, when we increase the peak intensities from  $0.9$  to  $1.8 \times 10^{14}$  W/cm<sup>2</sup> in Fig. 4.6(a). This also applies to the mid-IR wavelength in Fig. 4.6(b). The shift of the nuclear KER spectra to smaller KER values in Ref. [54] is ascribed to the fact that an increase of the peak intensity of a laser pulse is equivalent to an increase of the pulse duration. This is true when the applied laser field is relatively weak, i.e., the loss of the probability in H<sub>2</sub><sup>+</sup> continues gradually until the end of the laser pulse. However, when

the peak intensity is sufficiently large, the most loss of the probability in  $\text{H}_2^+$  takes place within a short time. Thus, for a larger peak intensity, the nuclear wave packet in  $\text{H}_2^+$  reaches smaller internuclear distances when the second ionization occurs, which results in signals at larger KER values, see Fig. 4.6. A similar shift of the nuclear KER spectra to slightly larger KER values was observed when the peak intensity was increased from 1 to  $5 \times 10^{14} \text{ W/cm}^2$  in an experiment where  $\text{D}_2$  interacting with 100-fs pulses at 600 nm was studied [77].

## Influences of nuclear mass

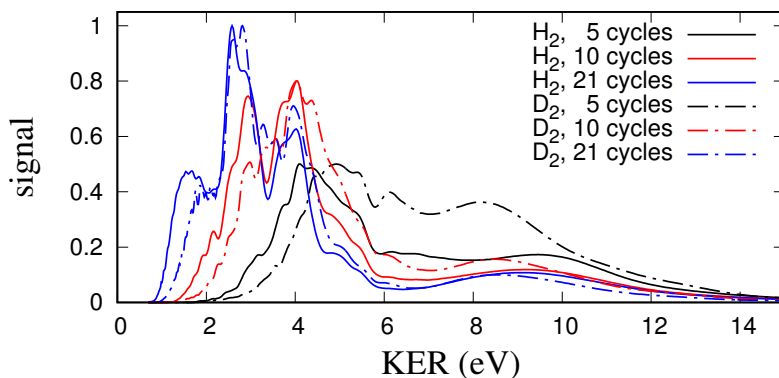


Figure 4.7: Nuclear KER spectra following double ionization of  $\text{H}_2$  and  $\text{D}_2$  interacting with laser pulses at 3200 nm for three pulse durations, i.e., 5, 10 and 21 cycles. The peak intensity is fixed at  $0.6 \times 10^{14} \text{ W/cm}^2$ .

In addition to the laser parameters, the nuclear mass has an effect on the nuclear dynamics. Generally speaking, the heavier the nuclei are, the more slowly they can move, and the slower the nuclear dynamics is. We will study the isotope effect on the nuclear KER spectra. The isotope effect has been studied at near-IR wavelengths [57] and we will extend the study to mid-IR wavelengths. We present the nuclear KER spectra following double ionization of  $\text{H}_2$  and  $\text{D}_2$  at a mid-IR wavelength of 3200 nm in Fig. 4.7 for three different pulse durations, i.e., 5, 10 and 21 cycles. At a given pulse duration, the nuclear KER spectrum for  $\text{D}_2$  moves to larger KER values compared to that for  $\text{H}_2$ . The shifts are more apparent for shorter pulse durations. The signals

at around 3 and 4 eV in Fig. 4.7 mainly come from trajectories whose second jumps occur the two CREI regions at  $R = 7$  and  $R = 11$ , respectively.

### 4.3 Nuclear KER spectra in an XUV-pump-IR-probe setup

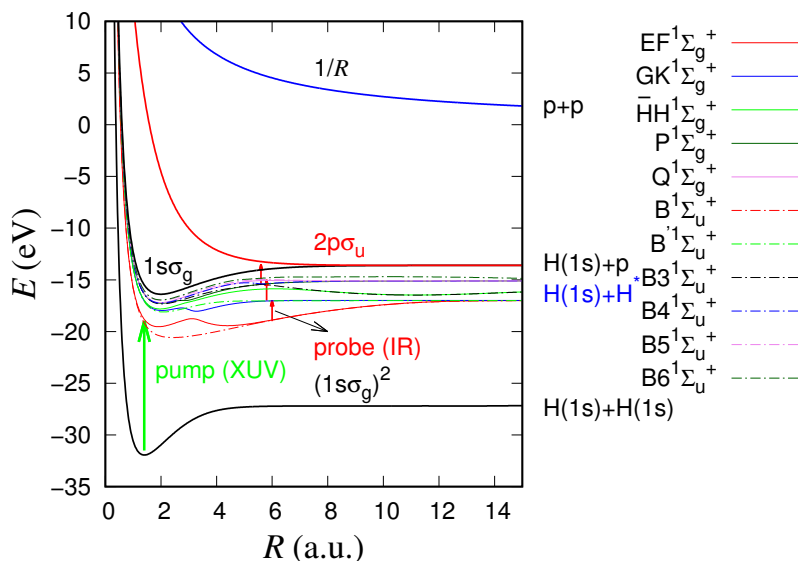


Figure 4.8: Potential energy curves for the electronic states as a function of  $R$ . They are the curves for the six lowest states of  $^1\Sigma_g^+$  and  $^1\Sigma_u^+$  symmetries in  $H_2$ , the curves for the ground and first excited states in  $H_2^+$  and the  $1/R$  Coulomb in  $H_2^{++}$ , respectively.

In the former section, we studied the interaction of  $H_2$  with single IR laser pulses. Double ionization of  $H_2$  ( $D_2$ ) by laser pulses in a pump-probe setup has been studied by many works [60, 78, 79]. The pump pulse is applied to initiate the dynamics in molecules and the probe pulse is applied to take the snapshots of the dynamics in real time. The XUV-pump-IR-probe setup has been applied to study nuclear dynamics in the singly excited states in  $H_2$  by obtaining the nuclear KER spectra following single ionization of  $H_2$  [80–82]. In this section,

we will apply MCWP approach to study the nuclear dynamics in the singly excited states in  $\text{H}_2$  following single and double ionization of  $\text{H}_2$  by using the XUV-pump-IR probe spectroscopy. The central frequency of the XUV pulse is chosen to make the lowest singly excited state of  ${}^1\Sigma_u^+$  symmetry resonantly excited in the Franck-Condon region, i.e.,  $\omega_{\text{XUV}} = 0.46$  a.u.. The IR pulse can induce couplings between the singly excited states in  $\text{H}_2$ . It can also induce the first ionization from the states in  $\text{H}_2$  to  $\text{H}_2^+$  and the second ionization from the states in  $\text{H}_2^+$  to  $\text{H}_2^{++}$ . Couplings between the two states in  $\text{H}_2^+$  are also induced by the IR laser pulse. The potential energy curves for the electronic states involved in our simulation are plotted in Fig. 4.8. They are the potential energy curves for the six lowest electronic states of  ${}^1\Sigma_g^+$  and  ${}^1\Sigma_u^+$  symmetries, for the  $1s\sigma_g$  and  $2p\sigma_u$  states in  $\text{H}_2^+$ , and the  $1/R$  curve in  $\text{H}_2^{++}$ . The energies for the ground and excited states of  $\text{H}_2$  are taken from ab initio calculations [83, 84]. The peak intensity of the XUV (IR) laser pulses is  $1 \times 10^{12}$  W/cm $^2$  ( $0.6 \times 10^{12}$  W/cm $^2$ ). The central wavelength of the IR pulse is 2400 nm. The XUV pulse has a sin-square envelope and the IR pulse has a Gaussian envelope. The electric fields for the XUV and IR pulses are

$$\begin{aligned}
 F_{\text{XUV}}(t) &= F_{\text{XUV}0} \sin^2\left(\frac{\pi t}{T_{\text{XUV}}}\right) \sin(\omega_{\text{XUV}}t), \\
 F_{\text{IR}}(t) &= F_{\text{IR}0} \exp\left(-\frac{2 \ln 2 (t - \tau - T_{\text{XUV}}/2)^2}{T_{\text{IR}}^2}\right) \\
 &\quad \times \cos\left(\omega_{\text{IR}}(t - \tau - T_{\text{XUV}}/2)\right), \tag{4.4}
 \end{aligned}$$

respectively.  $T_{\text{IR}}$  ( $T_{\text{XUV}}$ ) is the pulse duration (FWHM) of the IR (XUV) pulse. The pulse duration of the IR pulses is fixed at 3 laser cycles. The tunneling ionization rates from the excited states  $\text{H}_2$  are approximated by  $\Gamma_m(R, t) = \exp(-2[\sqrt{I_m(R)}]^3/[3F_{\text{IR}}(t)])$ , where  $I_m(R)$  are the  $R$ -dependent ionization potentials for the excited states. The dipole moment functions between electronic states are obtained through a configuration-interaction calculation for  $\text{H}_2$  [85].

In the MCWP method, we obtain the nuclear dynamics by solving Eq. (3.11) in each charge state, respectively. The initial nuclear wave packets in  $\text{H}_2^+$  and  $\text{H}_2^{++}$  can be similarly obtained as described in the previous section. To simulate single ionization of  $\text{H}_2$ , two charge states,

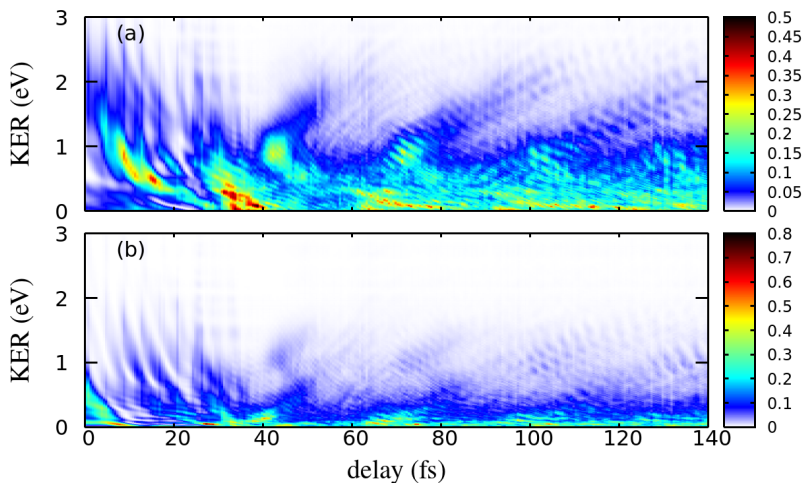


Figure 4.9: Nuclear KER spectra following single ionization of H<sub>2</sub> as a function of delay when an XUV-pump-IR-probe setup is applied. Contributions from the nuclear wave packets along the  $1s\sigma_g$  (a) and  $2p\sigma_u$  (b) curves. The pulse duration of the XUV pulse is 3 cycles.

i.e., H<sub>2</sub> and H<sub>2</sub><sup>+</sup>, are involved. Since there are 12 electronic states in H<sub>2</sub> involved in our calculation, the matrix of  $M(R)$  and  $V(R)$  in the small time propagator for H<sub>2</sub> are 12 by 12. We will present the nuclear KER spectra as a function a delay following single and double ionization of H<sub>2</sub> by applying the second sampling method in Sec. 4.1 to gather the first jumps. The second jumps are assumed to take place at every several time steps when we simulate double ionization of H<sub>2</sub>.

### Single ionization channel

For single ionization of H<sub>2</sub>, a trajectory is specified by its first jump time  $t_1$  and the state from which the first jump takes place. There are 12 first jump pathways. By projecting the nuclear wave packets  $\chi_m(R, t_e)$  (with  $m = g, u$ ) at the end of the IR laser pulse along the  $1s\sigma_g$  and  $2p\sigma_u$  curves in H<sub>2</sub><sup>+</sup> for a given trajectory on the corresponding eigenstates  $\chi_{Em}(R)$  for the two curves, one can obtain the nuclear KER

spectrum of  $\text{H}_2^+$  for that trajectory, i.e.,

$$p_{Em} = \left| \int dR \chi_{Em}(R) \chi_m(R, t_2) \right|^2. \quad (4.5)$$

with  $m = g, u$ . The total nuclear KER spectrum can be obtained by summing over the nuclear KER spectra for all the individual trajectories in  $\text{H}_2^+$ , i.e.,

$$P_E(k, t_1) = \sum_{k, t_1} P_1(t_1) P_{1k} \sum_{m=g, u} p_{Em}, \quad (4.6)$$

where  $P_1(t_1)$  is the total jump probability for the first jumps occurring at  $t_1$  and  $P_{1k}$  are the relative probabilities for different ionization pathways. We should note that the first jump probability  $P_1(t_1)$  relies on the sampling method.

We show in Fig. 4.9 the nuclear KER spectra following single ionization of  $\text{H}_2$  as a function of delay when an XUV-pump-IR-probe setup is applied. The pulse duration of the applied XUV pulse is 3 cycles. After absorption of a photon from the XUV pulse, the nuclear wave packets along the singly excited states of  $^1\Sigma_u^+$  symmetry in  $\text{H}_2$  are created. The IR pulse couples the excited states together since they are close with each other. The nuclear wave packets can move to large internuclear distances along the potential energy curves for the excited states in  $\text{H}_2$ . For the nuclear wave packets at large internuclear distances, the initial state in  $\text{H}_2^+$  following the first ionization would not prefer to one of two states in  $\text{H}_2^+$  since they are almost degenerate at large internuclear positions, i.e.,  $|c_g|^2 \approx |c_u|^2$ . Different from the double ionization channel, for the single ionization channel, contributions to the nuclear KER spectra from the nuclear wave packets along the  $1s\sigma_g$  curve are comparable to that from the  $2p\sigma_u$  curve [Figs. 4.9(a) and (b)].

From Fig. 4.9, we can see a periodical enhancement of the signals at KER values smaller than 0.5 eV. This period is around 30 fs, which results from the vibrational motion of the nuclear wave packets along the singly-excited states in  $\text{H}_2$ . There are several energy decreasing branches at delays smaller than 40 fs at Figs. 4.9(a) and (b), showing that the nuclear wave packets in the excited states move to larger internuclear distances.

## Double ionization channel

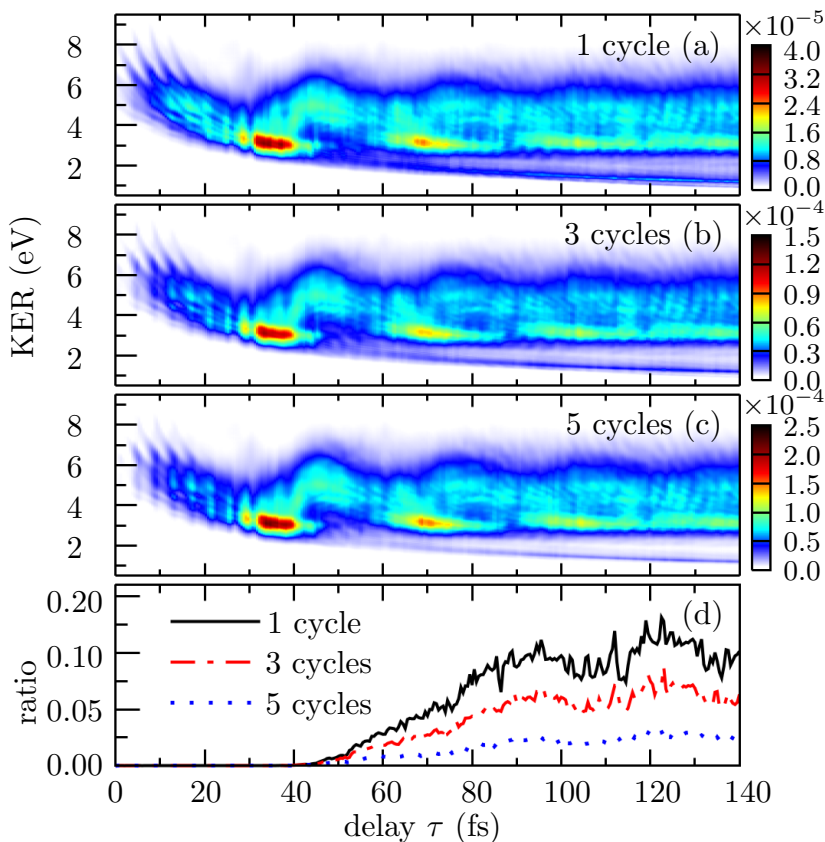


Figure 4.10: Results taken from Ref. [61]: nuclear KER spectra following double ionization of  $\text{H}_2$  within the XUV-pump-IR-probe setup when the XUV pulses are 1 (a), 3 (b) and 5 (c) cycles, respectively. (d) Ratios between the signals on the energy decreasing branches and the total yield for the three XUV durations as a function of delay.

The MCWP approach is particularly useful in simulating multiple ionization process. In this section, the nuclear KER spectra as a function of delay following double ionization of  $\text{H}_2$  are presented in Fig. 4.10. The results are for three XUV pulse durations, which are



#### 4.4. Nuclear KER spectra when autoionization from doubly excited states is involved

---

taken from our recent work [61]. We will summarize the main features in Fig. 4.10 and their origins in the following:

1. enhancements of the signals at KER values around 4 eV appearing at delays around 40, 70 and 100 fs. A detailed analysis in Ref. [61] shows us that this 30-fs period corresponds to the vibrational period of the nuclear wave packet evolving along the potential energy curve for the  $B^1\Sigma_u^+$  state in  $H_2$ .
2. periodical enhancements of the signals appearing at delays smaller than 30 fs. This period is half an IR laser cycle. The structure becomes clearer for larger XUV pulse durations and it originates from the AC Stark effect. When the IR field is strong (weak) at the overlap between the ultrashort XUV pulse and the IR pulse, the Stark shift of the  $B^+\Sigma_u^+$  state is large (small). Thus, the excitation from the ground state to the  $B^+\Sigma_u^+$  state in  $H_2$  is small (large) because the two states are off-resonant (resonant) with the XUV pulse.
3. an energy decreasing branch moving from around 2 to 1 eV for delays larger than 50 fs. The signals in this branch come from the nuclear wave packet reaching internuclear distances larger than  $R = 15$  a.u.. The nuclear wave packets at such large internuclear distances come from the dissociating part of the nuclear wave packet along the potential energy curve for the  $B3^1\Sigma_u^+$  state. This branch becomes relatively less important for a larger XUV pulse duration, which results from that there is a relatively smaller population transfer from the ground state to the  $B3^1\Sigma_u^+$  state when the XUV pulse is larger.

## 4.4 Nuclear KER spectra when autoionization from doubly excited states is involved

In the previous section, we investigated the nuclear dynamics when the singly excited states in  $H_2$  are involved. Now we will study the influences of the doubly excited states in  $H_2$  on the nuclear dynamics.

We still take the example of the simplest molecule of H<sub>2</sub>. A doubly excited state is a state where two electrons in the system are excited simultaneously. The doubly excited states in atoms stay beyond the first ionization threshold. In molecules, however, the doubly excited states may be below the first ionization threshold at certain internuclear distance regions. The singly excited states in atoms and molecules can decay to the more stable states via the radiation or non-radiation relaxation processes. In addition, vibrational autoionization [86, 87] may take place from the very highly excited states in molecules by converting the vibrational energy of the ion core to the kinetic energy of the outgoing electron. The doubly excited states in atoms and molecules can decay to more stable states by electron emission. This autoionization process may be a dominant relaxation process since it occurs much faster than the radiation or non-radiation relaxation processes.

The evidences of doubly excited states in the hydrogen molecules were provided by electron impact experiments [88, 89]. The doubly excited states can be also reached by absorption of one energetic photon from the external field [90, 91]. The doubly excited states in molecules can not only autoionize but also dissociate into two neutral nuclei. It was the doubly excited states in H<sub>2</sub> that resulted in the comparatively large ratio between H<sup>+</sup> and H<sub>2</sub><sup>+</sup> at the 26 eV photon energy [92]. *Ab initio* calculations have been conducted to obtain the potential energy curves and the corresponding autoionization rates for the doubly excited states [93–96]. There are series of doubly excited states. For example, the  $Q_1$  series are the doubly excited states lying between the first single-ionization threshold and the second single-ionization threshold and the  $Q_2$  series are made up of the doubly excited states beyond the second single-ionization threshold and below the third single-ionization threshold.

In this thesis, we apply the MCWP approach to study the influence of doubly excited states on the nuclear KER spectra of H<sub>2</sub><sup>+</sup> following photoionization of H<sub>2</sub> interacting with intense XUV pulses. The initial state is the ground state in H<sub>2</sub>, i.e.,  $X^1\Sigma_g^+(v=0)$ . Within the Frank-Condon region, the ionization potentials for the ground state in H<sub>2</sub> to the first and second single-ionization thresholds, i.e., the  $1s\sigma_g$  and  $2p\sigma_u$  states in H<sub>2</sub><sup>+</sup>, are around 18 and 30 eV, respectively. We show the potential energy curves for the above mentioned states in Fig. 4.11. After absorbing one photon with an energy larger than 18 eV and

#### 4.4. Nuclear KER spectra when autoionization from doubly excited states is involved

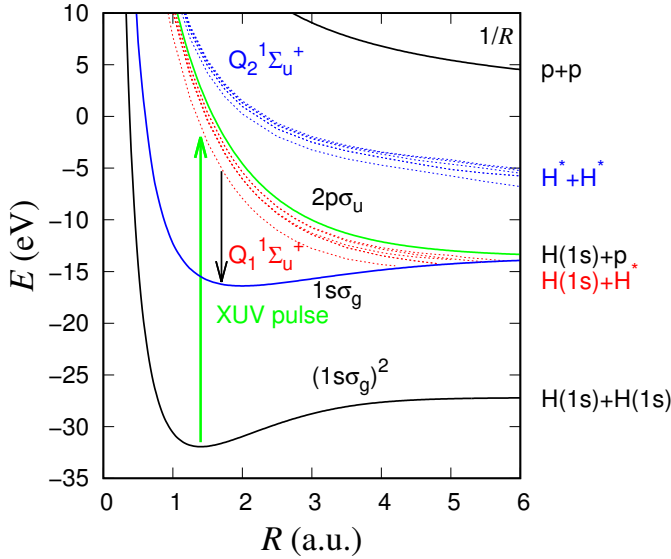


Figure 4.11: Potential energy curves for the ground electronic state in  $\text{H}_2$ , for the ground and first excited states in  $\text{H}_2^+$  and for selected  $Q_1^1\Sigma_u^+$  [94] and  $Q_2^1\Sigma_u^+$  [95] doubly excited states in  $\text{H}_2$ .

smaller than 30 eV, photoionization to the  $1s\sigma_g$  state in  $\text{H}_2^+$  is allowed. In addition to this direct ionization channel, first excitation to the the  $Q_1$  DESs and then autoionization to the  $1s\sigma_g$  state in  $\text{H}_2^+$  is also possible. Due to the fact that the laser polarization is assumed to be parallel to the molecular axis throughout this thesis, excitation to the  $Q_1^1\Sigma_u^+$  doubly excited states by the one-photon absorption is allowed according to the selection rule. We have also plotted the potential energy curves for the  $Q_1^1\Sigma_u^+$  DESs in Fig. 4.11. When the photon energy is increased over 30 eV, a new direct ionization channel, i.e., photoionization to the  $2p\sigma_u$  state in  $\text{H}_2^+$ , and excitation to the  $Q_2$  DESs are allowed. The potential energy curves for the  $Q_2^1\Sigma_u^+$  DESs are also plotted in Fig. 4.11.

In this thesis, we will focus on the interaction of  $\text{H}_2$  with XUV pulses at a central photon energy ranging from 25 to 28 eV. Thus, direct ionization to the  $1s\sigma_g$  state and excitation to the  $Q_1^1\Sigma_u^+$  states by absorption of one photon from the XUV pulse are allowed. As a result, three channels are involved:

#### 4. DISSOCIATIVE SINGLE OR DOUBLE IONIZATION OF H<sub>2</sub>

---

- $\text{H}_2 + \hbar\omega \rightarrow \text{H}_2^+(1s\sigma_g) + e^-$ , direct ionization
- $\text{H}_2 + \hbar\omega \rightarrow \text{H}_2^{**}(Q_1) \rightarrow \text{H}_2^+(1s\sigma_g) + e^-$ , autoionization
- $\text{H}_2 + \hbar\omega \rightarrow \text{H}_2^{**}(Q_1) \rightarrow \text{H}(1s) + \text{H}^*$ , dissociation

We can see from Fig. 4.11 that the potential energy curves for the  $Q_1$  DESs are repulsive and they cross with the potential energy curve for the  $1s\sigma_g$  state in H<sub>2</sub> at certain critical internuclear positions. The nuclear wave packets along the potential energy curves for the  $Q_1$  DESs move very fast. Autoionization from the DESs takes place at internuclear distances left to the crossing points. If there are nuclear wave packets evolving along the potential energy curves for the  $Q_1$  DESs beyond the crossing points, dissociation of H<sub>2</sub> into two neutral H atoms, i.e., one is in the ground state and the other is excited, is allowed.

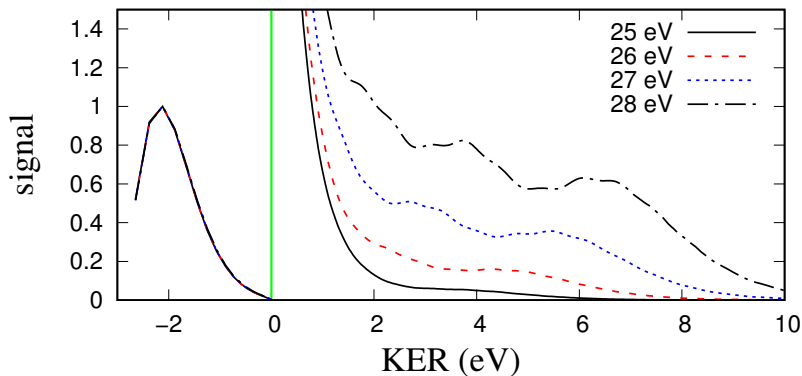


Figure 4.12: Nuclear KER spectra following single ionization of H<sub>2</sub> when interacting with XUV pulses at different photon energies. The signals at negative energies corresponds to the vibrational distribution for H<sub>2</sub><sup>+</sup> and the signals at positive energies to the proton kinetic energy distribution.

As we see in Fig. 4.11, the  $Q_1^1\Sigma_u^+$  states are very close to each other, the one-photon absorption would result in a coherent superposition of these states. The more states we include in our simulation, the more accurate results we would obtain. The following results, however, are obtained by only including the  $Q_1^1\Sigma_u^+(1)$  state. This simplification would greatly reduce our computational costs and it is a reasonable

#### 4.4. Nuclear KER spectra when autoionization from doubly excited states is involved

---

approximation since these  $Q_1^1\Sigma_u^+$  states are close to each other at the Franck-Condon region; the dipole coupling strengths from the ground state in  $H_2$  to the  $Q_1^1\Sigma_u^+(1)$  state are several times larger than that for the  $Q_1^1\Sigma_u^+(2)$  state [97]. It is also shown in Ref. [94] that the autoionization widths of the  $Q_1^1\Sigma_u^+(1)$  state are several times larger than that for the  $Q_1^1\Sigma_u^+(2)$  state. Thus, the influence of the  $Q_1^1\Sigma_u^+(1)$  state on the nuclear KER spectra would be dominant.

We show in Fig. 4.12 the nuclear KER spectra following single ionization of  $H_2$  interacting with a 10 fs XUV pulses at four central photon energies, i.e., 25, 26, 27 and 28 eV. These spectra are obtained by summing the spectra for the individual trajectories. The spectrum for each trajectory is calculated according to Eq. (4.5), i.e., by projecting the nuclear wave packets along the  $1s\sigma_g$  curve in  $H_2^+$  at the end of the propagation time on the corresponding eigenstates for the  $1s\sigma_g$  curve. We obtain the knowledge that the direct ionization cross section is about one order of magnitude larger than the absorption cross section to the  $Q_1^1\Sigma_u^+$  states for the considered photon energies [48]. The direct ionization channel would mainly lead to bound  $H_2^+$  signals at negative energies in Fig. 4.12 and the relatively weak channel, i.e, autoionization from the DESs to the  $1s\sigma_g$  state, can result in relatively large  $H + p$  signals at relatively large KER values. This is because the nuclear wave packets gain kinetic energies through moving along the potential energy curves for the DESs. We will summarize the other required calculation inputs in obtaining Fig. 4.12 in the following:

- The total photoionization cross section  $\sigma_p$  of  $H_2$  by photons at the considered energies can be found in Ref. [48]. The photoionization rate thus can be obtained using the relation

$$\Gamma_p = \frac{\sigma_p \times I_{XUV}}{\omega_{XUV}}, \quad (4.7)$$

where  $I_{XUV}$  is the intensity of the XUV pulse.

- assuming the first jumps occurring at every 40 a.u..

Now let us have a more careful look at Fig. 4.12. For better comparison, the amplitudes for the signals at -2.11 eV are rescaled to 1 for the four cases. The signals at negative energies corresponds to the vibrational distribution for  $H_2^+$  and the signals at positive energies

corresponds to the proton kinetic energy distribution. When we increase the photon energy from 25 to 28 eV, the spectra at negative energies look the same. This similarity implies that the signals at negative KER values are mainly from the direct ionization channel, where the photon energy only influences the absolute ionization cross section from H<sub>2</sub> to H<sub>2</sub><sup>+</sup> and has nearly no effect on initial the nuclear wave packets in H<sub>2</sub><sup>+</sup> after direct ionization. The spectra are quite different at positive KER values. First, there are relatively more and more signals when the photon energy is increased. Second, the spectra are extended to larger and larger KER values when the photon energy is increased. For example, when the XUV photon energy is 25 eV, a cutoff of 8 eV of spectrum is observed and when the XUV photon energy is 26 eV, we see a larger cutoff of 10 eV. The increase of the cutoff energy can be understood by the fact that a higher photon energy means a larger energy shared by the nuclei and autoionizing electron. The signals at positive energies become relatively larger for larger photon energies due to the fact that the direct ionization cross section is reduced for a larger photon energy and the photon energy becomes closer to the resonant photon energy within the Franck-Condon region. In addition, there is a slight shift of the peak positions to larger energies when the photon energy is increased: the peak for the 26 eV is at around 5 eV and for the 27 eV case at around 5.8 eV and for the 28 eV case at around 6.5 eV.

Next we will compare our simulation results with the experimental results in Ref. [98] and with the simulation results in Ref. [99]. Similar with the experimental results, there are relatively more dissociation signals and the spectra tend to become broader for larger photon energies and there are more structures at positive kinetic energies. We note, however, that our simulation results do not agree with the experiment [98] as well as the simulation in Ref. [99]. The discrepancies mainly emerge at the positive kinetic energies. One discrepancy is that we have a longer tail at relatively large energies. This is because part of the the nuclear wave packets along the  $Q_1^1\Sigma_u^+(1)$  curve would evolve to internuclear distances larger than the cross point between this curve and the  $1s\sigma_g$  curve and thus autoionization taking place near the cross point would result in a large KER value, which is indeed the cutoff energy in our spectra. In fact, the cutoff energy can be obtained by using the energy conservation, i.e.,  $\omega_{\text{XUV}} = E_e + \text{KER} + \text{IP} + 1.5 \text{ eV}$ ,

#### 4.4. Nuclear KER spectra when autoionization from doubly excited states is involved

where  $E_e$  is the energy for the autoionizing electron and IP is the ionization potential to the  $1s\sigma_g$  state in  $\text{H}_2^+$  within the Franck-Condon region. For example, the cutoff energy for the 25 eV case is around  $\text{KER} = 25 - 18.5 = 6.5$  eV. While the experiment gave a smaller cutoff of at around 4 eV at this photon energy. There are also differences for the peak positions, e.g., we can not reproduce the peaks at around 1 eV by our spectra, which may come from a underestimate of the contributions from the DES. Further efforts should be taken to resolve the discrepancies.

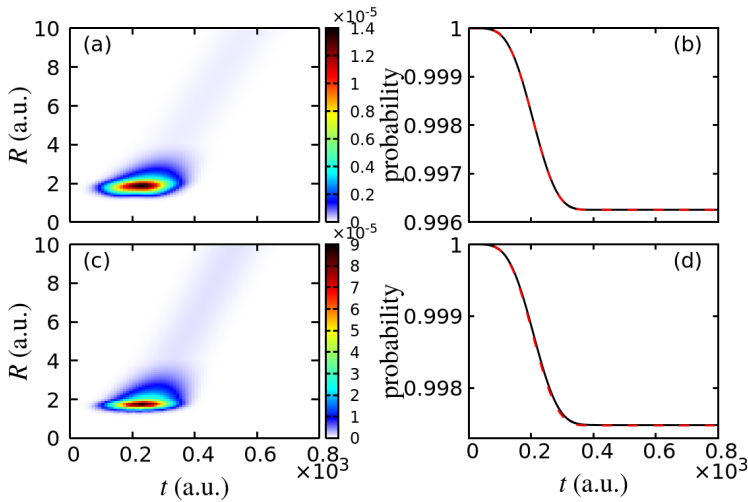


Figure 4.13: Evolution of the nuclear wave packets along the potential energy curve for the  $Q_1^1\Sigma_u^+(1)$  state when interacting with laser pulses at 25 eV (a) and 28 eV (c). The probability as a function of time staying in  $\text{H}_2$  for 25 eV (b) and 28 eV (d). In both (b) and (d), the solid (black) curve is for the probability in  $\text{H}_2$  and the dashed (red) curve for that in the ground state in  $\text{H}_2$ .

In Fig. 4.13, we show the evolution of the nuclear wave packets along the  $Q_1^1\Sigma_u^+$  state for two cases, i.e.,  $\omega_{\text{XUV}} = 25$  and 28 eV. For the both two cases, the nuclear wave packets move very quickly and reach beyond the cross point at around  $R = 4$  in 400 a.u. (10 fs). The XUV pulse is as short as 10 fs, thus when  $t$  is larger than 400 a.u., no excitation from the ground state to the  $Q_1^1\Sigma_u^+$  state and no

autoionization to the  $1s\sigma_g$  state in  $\text{H}_2^+$ . We also show in the left panel the probability of staying in  $\text{H}_2$  and in the ground state of  $\text{H}_2$  as a function of time for the two cases. For both two cases, the two curves are very close to each other, which means that the direct ionization dominates the ionization process. For the 28 eV case, there is visible difference between the two probabilities and thus the autoionization from the DES plays a more important role. This is consistent with our findings in Fig. 4.12 that there are more signals at positive KER values for larger photon energies.

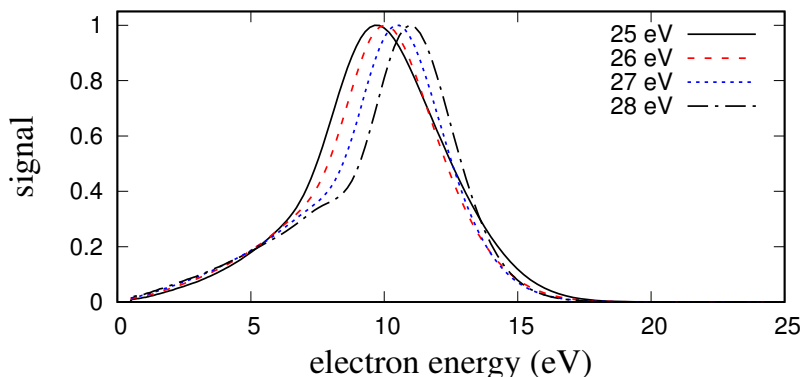


Figure 4.14: Autoionizing electron spectra following single ionization of  $\text{H}_2$  interacting with XUV pulses at different photon energies.

Apart from the nuclear KER spectra, we can obtain the kinetic energy spectra for the autoionizing electrons. We show the results for the above mentioned four cases in Fig. 4.14. The spectra are obtained by simply using the fact that autoionization at a specific  $R$  along the  $Q_1^1\Sigma_u^+$  curve would result in an electron whose kinetic energy is the energy difference between the DES state and the  $1s\sigma_g$  state at that position, i.e.,  $E_e = E_{\text{DES}}(R) - E_g(R)$ . The probability to produce an electron at a given  $R$  is directly related to the initial nuclear wave packets created along the  $1s\sigma_g$  curve following autoionization at  $t_1$ , i.e.,  $P(R) = \Gamma_{\text{DES}}(R)|\chi_{\text{DES}}(R, t_1)|^2$ . By summing the spectra for all the trajectories, we can get the kinetic energy spectrum for the autoionizing electron. From Fig. 4.14, we can see that the autoionizing electron kinetic energy spectra tend to move to larger kinetic energies for larger photon energies. This feature is due to a larger energy is



shared by the autoionizing electron and the nuclei for a larger photon energy. Thus, as we discussed before, it actually is consistent with a larger cutoff KER value of the nuclear KER spectra in Fig. 4.14. The peak at a given KER position demonstrate that the nuclear wave packets along the  $Q_1^1\Sigma_u^+$  curve are largely decayed to the  $1s\sigma_g$  state at specific internuclear distances. For example, the peak at 11 eV for the 28 eV case corresponds to large autoionization at around  $R = 1.7$  a.u., while for the 25 eV case peak at 9 eV corresponds to large autoionization at around  $R = 1.9$  a.u..

## 4.5 Concluding remarks

In this chapter, we have applied the MCWP method to study the interaction of  $H_2$  with intense laser pulses including single IR femtosecond pulses, combined pulses in the XUV-pump-IR-probe setting and single XUV pulses. When we consider the interaction of  $H_2$  with intense IR pulses, tunneling ionization from  $H_2$  to  $H_2^+$  and from  $H_2^+$  to  $H_2^{++}$  can take place. Thus, we have obtained the nuclear KER spectra following the full break-up of  $H_2$ , since our method is especially powerful in treating the double or multiple ionization processes. We have studied the influences of the laser parameters as well as the nuclear mass on the nuclear dynamics in  $H_2$  when exposed to laser pulses at IR wavelength. When we consider the interaction of  $H_2$  with XUV pulses, relatively large single-photon ionization or excitation would be induced from the ground state in  $H_2$  when the XUV photon energy is larger than the ionization potential or is comparable with the energy difference between the excited electronic states and the ground state in  $H_2$ . We have obtained and analyzed the nuclear KER spectra following double ionization of  $H_2$  to resolve the nuclear dynamics in the singly excited states in  $H_2$  by using XUV-pump-IR-probe spectroscopy. By tuning the photon energy, photoionization may be accompanied by the excitation of double excited states. Compared with the singly excited states, (when the singly excited states are very close to the ionization thresholds, vibrational autoionization [86, 87] may also take place in molecules, but we will do not study this process in this thesis), there are autoionization from DESs due to the electron correlation, i.e., the energy of one electron is transferred to the other electron to remove the

other electron from the molecule. We have studied the influences of the excitation of the  $Q_1$  DESs and the autoionization from the DESs in H<sub>2</sub> to the nuclear KER spectra following single ionization of H<sub>2</sub>. More efforts should be put into the study of the influence of the DESs on the nuclear dynamics in H<sub>2</sub> to resolve the discrepancies between our simulation and the experiment. Further studies can be conducted on obtaining the lifetimes of the DESs by using the pump-probe spectroscopy.

---

# Dissociative triple ionization of $\text{Ne}_2$

The previous chapter shows us the application of the MCWP approach to study the nuclear dynamics following ionization and excitation of molecules by intense laser pulses. In this chapter, we will turn to study the ultrafast dynamics in a new system, i.e., weakly bounded clusters. In the field of atomic and molecular physics, clusters refer to a bunch of atoms or molecules which are loosely bounded by weak attraction forces, i.e., Van der Waals forces or hydrogen bonds, between them. The size of clusters ranges from 2 to millions of atoms or molecules. The bonds in forming clusters are comparably weak compared with ionic or covalent bonds in molecules. Thus, clusters are not as stable as molecules and are prone to break up under external interferences. The interactions between the constituent atoms and molecules in clusters are either repulsive or attractive, depending on the internuclear distances and the electronic states. Thus, similar to molecules, following excitation or ionization by a strong external field, nuclear dynamics are induced in weakly bounded clusters. Different from molecules, due to the weak interactions between individual atoms or molecules in clusters, the double or higher ionization thresholds for clusters are lowered than that for the constituent atoms or molecules. Thus, unique electronic decay channels are opened for weakly bounded clusters, e.g., the interatomic (intermolecular) Coulombic decay (ICD) and electron transfer mediated decay (ETMD) [100].

Before we go detailed to ICD or ETMD, we first give a short introduction of a multi-electron effect called the Auger decay, named after P. V. Auger who independently discovered this effect after L. Meitner's first discovery. The Auger decay is a phenomenon that the filling of a deep inner-shell vacancy, e.g., a core-shell vacancy, within an atom is accompanied by the emission of another electron. The Auger effect has been widely investigated in atoms and molecules [101–103]. The core-shell vacancy in an atom can be created by the incidence of very highly energetic photons or electrons to atomic or molecular samples. After the emission of a core-shell electron, the remaining ion is highly excited and unstable, and thus would relax to more stable states through an emission of an energetic photon or electron. This electronic decay is energetically allowed since the highly excited ionic state is above the lowest double ionization thresholds for the atom or molecule. The electronic and radiational decays are competitive and the former one would be more favorable since it is much faster than the latter case, typically on a timescale of femtoseconds.

However, if a inner-shell electron is kicked out from an atom, it is energetically forbidden for the Auger decay to take place. This is because even though the remaining ionic state is still excited, it is now below the lowest double ionization thresholds for the atom or molecule. It becomes fascinating when the atom has weakly bounded neighbors, i.e., these atoms or molecules have formed clusters. The energy released from filling the inner-shell vacancy can not support to remove an outer-valence electron from the same site but it can supply the emission of an outer-valence electron at the neighboring sites via a virtual photon. This process is called interatomic (intermolecular) Coulombic decay (ICD) due to the fact that it is an interatomic (intermolecular) phenomenon and ICD is driven by the Coulombic interaction between the two electrons. For the ICD processes, two resultant positively charged particles would repel with each other via the Coulomb force between them. This electronic decay mechanism was first theoretically predicted by [104] and later experimental evidences were found in Van der Waals clusters [105–107] and hydrogen bonded clusters [108–110]. The direct ICD process is shown in Fig. 5.1. The ICD occurs at a timescale from a few to hundreds of femtoseconds, depending on the size and type of clusters. Thus in some clusters where the ICD lifetimes are comparable to the timescales for the nuclear dynamics, it

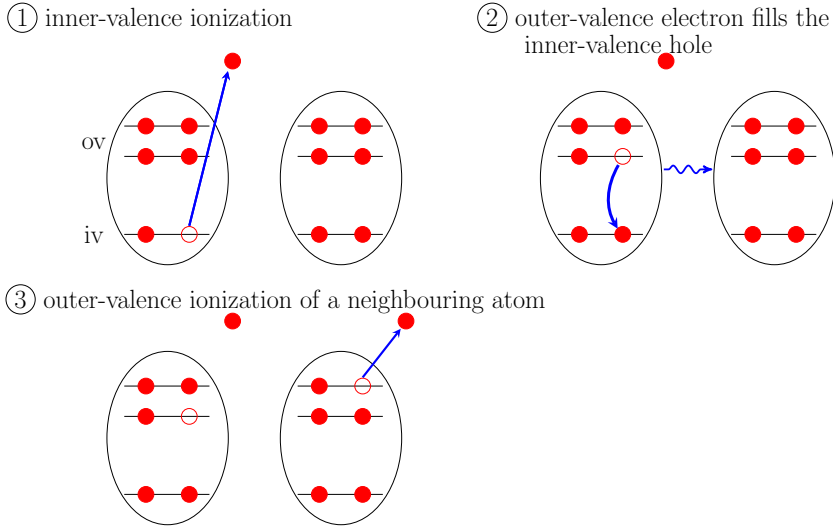


Figure 5.1: A direct ICD process in a dimer: 1, the inner-valence electron is freed from one atom by the incident energetic photon; 2, the inner-valence hole is refilled by an outer-valence electron; 3, the released energy supports to kick out one outer-valence electron from an atom in a neighbouring site of a cluster.

would be more accurate to take the nuclear dynamics of clusters into consideration [111–113]. The nuclear KER spectra following ICD and the ICD electron kinetic energy spectra have been studied. Similar to Auger electron spectroscopy, ICD electron spectroscopy can be used to study the cluster structures.

When we study ICD in clusters, the lifetimes of the excited states where ICD occurs are of main interests. The ICD lifetimes can be obtained from the ICD electron spectra [104, 105], i.e., the inverse of the linewidth of the ICD electron spectrum  $\tau_{\text{ICD}} \sim 1/\Gamma_{\text{ICD}}$ . The ICD rates can be calculated by using the complex absorbing potential method [114] and by the Wigner-Weisskopf expression [115]. Besides, one can also extract the ICD lifetimes from the measured nuclear KER spectra following ICD by using the knowledge that the signals resulting from ICD would increase exponentially [62], i.e.,  $a - b \exp(-t/\tau_{\text{ICD}})$ . The experiment in Ref. [62] provides us the nuclear KER spectra following triple ionization of the neon dimer. So far, there is no quan-

tum theory applied to obtain the similar nuclear KER spectra as a function of delays. Therefore, in this chapter, we will extend our MCWP method to simulate this process, which is beyond the capacity of many theories, to help us to better understand the involved ICD processes in the neon dimer. We will show in the following section the implementation of the MCWP approach to treat triple ionization.

## 5.1 Implementation of the MCWP method to triple ionization of $\text{Ne}_2$

In Chapter 3, we have presented in detail how to apply the MCWP approach to simulate the process of double ionization of a molecule due to its interaction with intense laser pulses. Now we will extend our method to simulate the process of triple ionization, i.e., two photoionizations and an autoionization via ICD, in  $\text{Ne}_2$ . An XUV-pump-XUV-probe setup is applied to resolve the involved ICD dynamics in the neon dimer. Four charge states are involved during this process, i.e.,  $\text{Ne}_2$ ,  $\text{Ne}_2^+$ ,  $\text{Ne}_2^{2+}$  and  $\text{Ne}_2^{3+}$ . This triple ionization process is described in detail as follows: starting from the initial state, i.e., the ground state of  $\text{Ne}_2$ , the system would evolve and stay in  $\text{Ne}_2$  until

- 1 an  $2s$  inner-valence electron is removed from one of the atom in  $\text{Ne}_2$  by the XUV pump pulse,
- 2 nuclear dynamics is induced in the remaining ion, i.e.,  $\text{Ne}_2^+(1s^{-1})$ . At the same time, it can be further ionized by the XUV pump or probe pulse to  $\text{Ne}_2^{2+}(1s^{-1}2p^{-1})$  or can undergo an ICD to  $\text{Ne}_2^{2+}(2p^{-2})$  because the cation is highly excited,
- 3 nuclear dynamics in  $\text{Ne}_2^{2+}(2p^{-2})$  or  $\text{Ne}_2^{2+}(1s^{-1}2p^{-1})$  is also induced. Besides,  $\text{Ne}_2^{2+}(2p^{-2})$  can be further ionized by absorption of an XUV photon from the XUV pump or probe pulse to  $\text{Ne}_2^{3+}(2p^{-3})$  and  $\text{Ne}_2^{2+}(1s^{-1}2p^{-1})$  would also decay to  $\text{Ne}_2^{3+}(2p^{-3})$  via ICD.

We assume that the neon dimer is rotationally frozen since the rotational timescale is much larger than that for the vibrational motion of  $\text{Ne}_2$ . Thus, the evolution of the nuclear dynamics in each charge state

## 5.1. Implementation of the MCWP method to triple ionization of $\text{Ne}_2$

can be obtained by solving the simplified one-dimensional equations, i.e., Eq. (3.11) for each charge state. To solve the above-mentioned equation(s) in the positive charge states, the initial conditions, i.e., the initial nuclear wave packets after ionization, are required. We know that it is the quantum jumps, either in the manner of photoionization or autoionization, that connect different charge states together. Thus, applying the jump operators to the electronic states in a given charge state according to Eq. (3.7), the initial nuclear wave packet in the charge state with one electron less at a given jump time can be obtained. The potential energy curves for the electronic states involved in our simulation are plotted Fig. 5.2. They are extracted from Ref. [62].

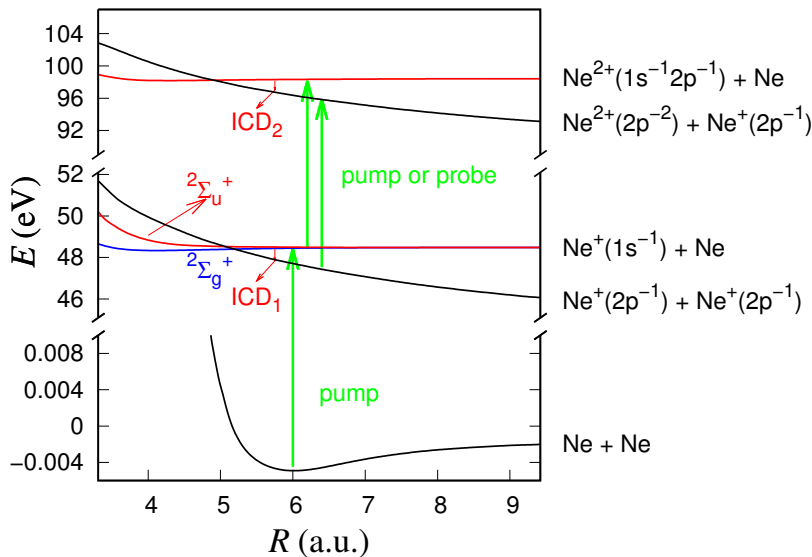


Figure 5.2: Selected Born-Oppenheimer potential energy curves as a function of the internuclear distance  $R$  for  $\text{Ne}_2$ . From bottom to top at  $R = 5$  a.u., they are the potential curves for the ground state in  $\text{Ne}_2$ , the  $2^2\Sigma_g^+$  and  $2^2\Sigma_u^+$  inner-valence hole states in  $\text{Ne}_2^+$ , the two-site outer-valence hole state in  $\text{Ne}_2^{2+}$ , the inner- and outer-valence vacancy state in  $\text{Ne}_2^{2+}$  and the two-site triple outer-valence vacancy state of  $\text{Ne}_2^{3+}$ , respectively.

As shown in Fig. 5.2, we only include the ground electronic state

in  $\text{Ne}_2$  since the excited states in  $\text{Ne}_2$  are far away from resonance with the XUV pulses. This curve is very shallow which reflects the weak bounded feature of the neon dimer. In  $\text{Ne}_2^+$ , the  $2^2\Sigma_u^+$  and  $2^2\Sigma_g^+$  states are involved. Due to the different symmetry of these two states, the one-photon ionization would result in an incoherent superposition of these two states. The couplings between the two states can be neglected because of the relatively large photon energy compared with the energy separation between the two states. There are several two-site outer-valence vacancy states in  $\text{Ne}_2^{2+}$ . As they are nearly parallel and are close to each other, only considering one averaged state would capture the important dynamics. It is also possible to open the channel of populating the single-site inner- and outer-valence vacancy state from the two inner-valence hole states in  $\text{Ne}_2^+$  by the XUV pulse. For simplicity, only one state is included. This state can also undergo an ICD to the triply ionized neon dimer. There are several states for the triply ionized states and since they are nearly parallel to each other we only include one for simplicity. Compared with the double ionization case, the implementation of the MCWP approach to the triple ionization process is more complicated since we have to include a third ionization channel into our simulation. Another aspect that results in the increase of the computational costs is that we have to evolve the nuclear wave packets long after the pulse until ICD removes most of the population in the excited state.

The sampling strategy for the triple ionization process is summarized below. We have considered two pulses cases, the XUV pulse is a coherent pulse or a chaotic pulse with random noises. The former case models the pulses from table-top lasers by high harmonic generation processes. Similar to the XUV pulses applied in Chapter 4, the coherent pulses have a sin-square envelope and its field is expressed by Eq. (4.4). The latter case models the pulses free electron lasers (FEL) in self-amplified spontaneous emission mode. For the first jumps from  $\text{Ne}_2$  to  $\text{Ne}_2^+$  by photoionization, it is reasonable for both cases to take the second sampling method in Chapter 4, i.e., assuming the first jumps occurring at the instants whose ionization probabilities are locally largest. For the second jumps to  $\text{Ne}_2^+$  to  $\text{Ne}_2^{2+}$ , however, the photoionization is accompanied by the ICD which continues to take place long after the pulse. During the ICD, the nuclear wave packets experience a substantial change. Thus, the second sampling method



## 5.1. Implementation of the MCWP method to triple ionization of $\text{Ne}_2$

in Chapter 4 is not appropriate to carry the information of the nuclear dynamics. We instead choose the third sampling method in Chapter 4, which assumes the jumps occurs at every several time steps. The third sampling method is similarly applied to pick up the trajectories for the third jumps from  $\text{Ne}_2^{2+}$  to  $\text{Ne}_2^{3+}$ . The nuclear wave packet in  $\text{Ne}_2$  nearly does not change due to the fact that the initial state is the ground state. Even though the coherent pulses have smooth envelopes while the chaotic pulses do not, we can consider only one first jump with its probability being the total ionization probability in  $\text{Ne}_2$  due to the interaction with the pulses. Under this circumstance, the computational time for the chaotic pulses is not increased.

There have been plenty of works [116–118] which studied the field statistics of the self-amplified spontaneous emission FEL sources. Due to random noises, the coherence of the FEL pulses is broken and pulses are different from shot to shot. Researchers show that the coherence time of the FEL pulses is decreased and thus is equivalent to ultrashort pulses which is powerful to capture ultrafast dynamics [119]. In the following, we will present how to use the partial coherence method [120] to model the chaotic pulses. First, the average frequency spectra for the intensity of the pulses from many shots are obtained, i.e.,  $I(\omega)$ . The average electric field spectra is the square root of that for the intensity, i.e.,  $E(\omega) = \sqrt{I(\omega)}$ . Now it is time to introduce the random noises by introducing random phases  $\theta_n(\omega)$ , i.e.,

$$E_1(\omega) = E(\omega) \exp(-i\theta_n(\omega)). \quad (5.1)$$

The temporal electric field  $E_1(t)$  is obtained after performing a Fourier transform of  $E_1(\omega)$ . The obtained result  $E_1(t)$  is totally incoherent and infinitely long in the time domain. To have a limited pulse duration  $\tau_p$  instead, one has to multiply a temporal filtering function  $f(t)$  to  $E_1(t)$ . For example, we can choose a temporal Gaussian filtering function if the average temporal envelope has a Gaussian envelope. We assume a Gaussian filtering function in our simulation and thus the electric field  $E(t)$  is

$$E(t) = \exp\left(-\frac{2 \ln 2 (t - t_c)^2}{\tau_p^2}\right) E_1(t). \quad (5.2)$$

with  $t_c = 1.5\tau_p$ . The constructed pulse after the above mentioned procedures is partially coherent and this is the reason why this method

is called the partial coherence method. In Fig. 5.3, as an example, we show several chaotic pulses constructed by the partial coherence method. The laser parameters are as follows: the central frequency is 2.14 a.u., the average pulse duration is 60 fs, the average bandwidth is 0.1 a.u., and the peak intensity is  $1 \times 10^{12}$  W/cm<sup>2</sup>. We can clearly

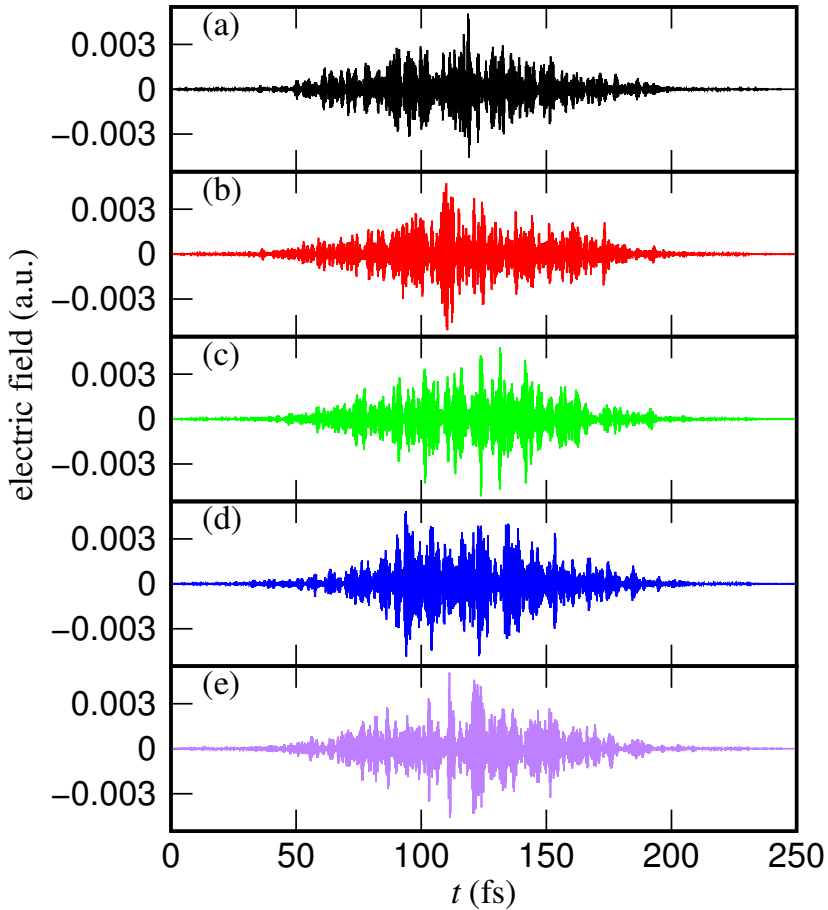


Figure 5.3: Temporal electric fields for five chaotic FEL pulses (a)-(e). The laser parameters of the FEL pulses are as follows: the central photon energy is 2.14 a.u., the average pulse duration is  $\tau_p = 60$  fs, the average bandwidth is 0.1 a.u., and the peak intensity is  $I_0 = 10^{12}$  W/cm<sup>2</sup>.

## 5.1. Implementation of the MCWP method to triple ionization of $\text{Ne}_2$

observe the fast variation of the field envelope for the chaotic pulses. That is the origin why we have to take more sampling points when treating  $\text{Ne}_2$  interacting with the chaotic pulses.

The nuclear KER spectrum following triple ionization of  $\text{Ne}_2$  can be obtained by summering over the contributions from all the trajectories. Each trajectory is specified by its first, second and third jump times, i.e.,  $t_1$ ,  $t_2$  and  $t_3$ , and the states from which the first, second and third jumps takes. For the trajectories taking place at  $t_1$ ,  $t_2$  and  $t_3$ , the ionization probabilities for the first, second and third jumps are  $P_1(t_1)$ ,  $P_2(t_2)$  and  $P_3(t_3)$ , respectively. When there are more than one jump pathways from one charge state to another charge state, the actual ionization probability for the  $j$ th pathway for the  $k$ th jump, i.e.,  $\bar{P}_{kj}$ , should be a multiplication of the ionization probabilities  $P_k$  by the relative probability for that pathway, i.e.,  $\bar{P}_{kj}(t_k) = P_k(t_k) \times P_{kj}(t_k)$ . Here the relative probability for the  $j$ th pathway is

$$P_{kj}(t_k) = \frac{\langle \Psi(t_k) | C_{kj}^\dagger C_{kj} | \Psi(t_k) \rangle}{\sum_j \langle \Psi(t_k) | C_{kj}^\dagger C_{kj} | \Psi(t_k) \rangle}, \quad (5.3)$$

Where  $|\Psi\rangle$  is expressed by Eq. (2.25) and  $C_{kj}$  is the jump operator describing the  $j$ th jump pathway for the  $k$ th jump by Eq. (3.3). The nuclear KER spectrum for each trajectory is obtained by projecting the nuclear wave packets at the end of propagation, i.e.,  $\chi_3(R, t_e)$ , in  $\text{Ne}_2^{3+}$  to its energy-normalized vibrational eigenstates  $\chi_E(R)$  for the final potential energy curve, i.e.,

$$p_{Ejkm}(t_1, t_2, t_3) = \left| \int dR \chi_3(R, t_e; j, k, m, t_1, t_2, t_3) \chi_E(R) \right|^2 \quad (5.4)$$

Thus, the total nuclear KER spectrum following triple ionization is

$$\text{KER} = \sum_{j,k,m,t_1,t_2,t_3} \bar{P}_{1j} \bar{P}_{2k} \bar{P}_{3m} p_{Ejkm}(t_1, t_2, t_3). \quad (5.5)$$

The input data in our calculation are as follows. The photoionization cross section of the  $2s$  inner-valence electron in  $\text{Ne}_2$  was approximate by the photoionization cross section of the  $2s$  electron in Ne [121], i.e.,  $\sigma_{2s/2p} = 0.36$  Mb. There have been no works in investigating the photoionization from  $\text{Ne}_2^{2+}(2p^{-2})$  to  $\text{Ne}_2^{3+}(2p^{-3})$  and we approximate this process by the photoionization of the neon atom [122]. Thus the

photoionization cross section from  $\text{Ne}_2^{2+}(2p^{-2})$  to  $\text{Ne}_2^{3+}(2p^{-3})$  is approximated by  $\sigma_{2p}^{3p} = 8.08$  Mb. We can find the ICD rates from the two excited states in  $\text{Ne}_2^+$  in Ref. [123] where they were calculated by the complex absorbing potential method. Another ICD process from  $\text{Ne}_2^{2+}(1s^{-1}2s^{-1})$  to  $\text{Ne}_2^{3+}(2p^{-3})$  has been not investigated in literature and the ICD rates are simply assume to be same with the first ICD process. The photonization cross section from  $\text{Ne}_2^+(1s^{-1})$  to  $\text{Ne}_2^{2+}(1s^{-1}2s^{-1})$  is unknown and we make an initial guess, i.e.,  $\sigma_{1s}^{2p} = 0.24$  Mb and laser adjust it according to the comparison between our simulation results and the experimental results.

Similar to the H<sub>2</sub> case, we adopt the split-operator fast Fourier transform method to solve Eq. (3.11) in each charge state numerically. We utilize a time step of  $\Delta t = 4$  a.u.. and a space step  $\Delta R = 0.0215$  a.u. in our simulation. The reason why we can choose a relatively large  $\Delta t$  here is the photoionization involved in this triple ionization process follows the relatively slow-varying temporal profile of the intensity of the XUV pulse. To avoid reflection from the box boundaries, we adopt a simulation box from  $R_{\min} = 3.32$  a.u. to  $R_{\max} = 91.15$  a.u.. For both the coherent and chaotic pulse cases, the first jump occurs at the intensity maximum and the second and third jumps are assumed to occur at every 40 time steps.

## 5.2 Nuclear KER spectra following triple ionization of Ne<sub>2</sub> interacting with coherent XUV pulse

In this section, we will present the results obtained by our method for Ne<sub>2</sub> interacting with coherent XUV pulses. According to the experiment, the pump and probe pulses are identical to each other except the probe pulse is delayed by  $\tau$ . The vector potential of the pump pulse is expressed by

$$A(t) = \begin{cases} A_0 \sin^2\left(\frac{\pi t}{T_{\text{XUV}}}\right) \cos(\omega_{\text{XUV}} t) & 0 \leq t \leq T_{\text{XUV}}, \\ 0 & \text{elsewhere,} \end{cases} \quad (5.6)$$

where  $T_{\text{XUV}}$  is the pulse duration of the pump pulse and the electric field can be obtained by using the relation  $F(t) = -\frac{\partial A(t)}{\partial t}$ . The peak

## 5.2. Nuclear KER spectra following triple ionization of Ne<sub>2</sub> interacting with coherent XUV pulse

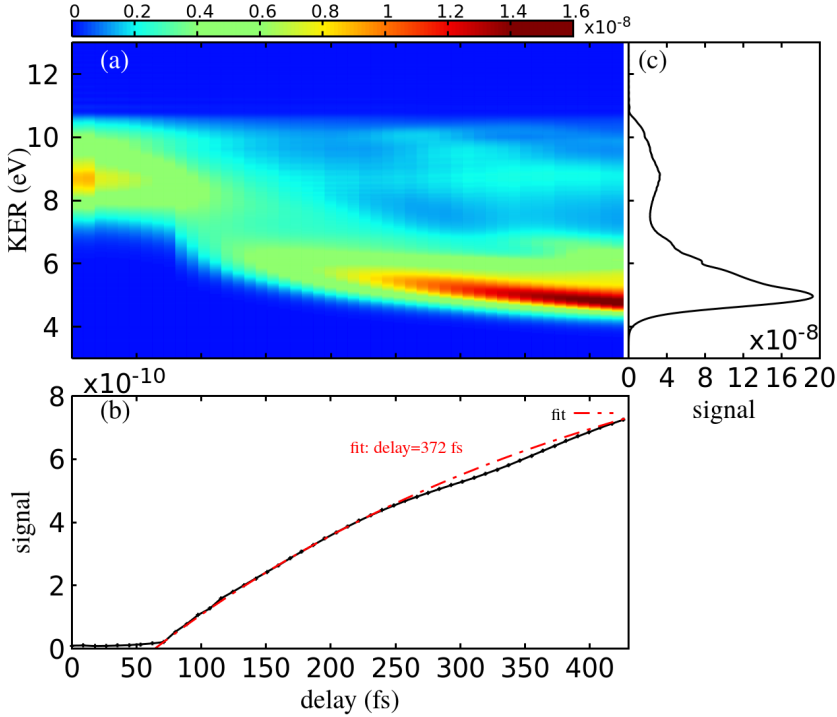


Figure 5.4: (a) Calculated nuclear KER spectra for coincident Ne<sup>2+</sup> and Ne<sup>+</sup> fragments following triple ionization of Ne<sub>2</sub> as a function of delay  $\tau$  when the applied XUV pump and probe pulses are coherent pulses. (b) The solid line shows yields of coincident Ne<sup>2+</sup> and Ne<sup>+</sup> pairs integrated over KER values between 3 and 7 eV in (a), i.e.,  $\int_3^7 \text{eV} dE \text{ KER}(E; \tau)$ . The dashed line is an exponential fit of the solid line to extract the lifetime of the ICD in Ne<sub>2</sub>. (c) Sum of KER spectra for delays between 300 and 420 fs in (a).

field strength is  $F_0 = A_0 \omega_{\text{XUV}} = 0.005338$  a.u. corresponding to a peak intensity of  $1 \times 10^{12}$  W/cm<sup>2</sup>. The central frequency is  $\omega_{\text{XUV}} = 2.14$  a.u. and the pulse duration is  $T_{\text{XUV}} = 60$  fs.

In Fig. 5.4, we show the nuclear KER spectra following triple ionization of Ne<sub>2</sub>. Our spectra look quite similar to the spectra obtained by the experiment in Ref. [62]. The two most important features are reproduced by our simulation: the energy decreasing branch which is

directly related to the ICD process from  $\text{Ne}_2^+(1s^{-1})$  to  $\text{Ne}_2^{2+}(2p^{-2})$  and the delay-independent high energy branch centered at about 9 eV. By conducting a trajectory and wave packet analysis (we do not show the results here), we find the origins of the two branches. The signals at the energy decreasing branch comes from the nuclear wave packets evolving along the repulsive potential energy curve for the  $\text{Ne}_2^+$  following an ICD from  $\text{Ne}_2^+$  are later photoionized to  $\text{Ne}_2^{3+}$  by the probe pulse. Thus, if the pump probe delay is larger, then there is a longer time for the nuclear wave packets moving to larger internuclear distances in  $\text{Ne}_2^+$ . This finally results in coincident  $\text{Ne}^+$  and  $\text{Ne}^{2+}$  signals at smaller KER values. The high energy branch is from the triple ionization taking place within a short time, to say, within either the pump or probe pulse. Apart from that, we can also observe the similarity that there are more signals at delay close to 0 due to the constructive interference between the pump and probe pulse. We can also observe discrepancies between our results and the experimental results:

- the ratio of the signals between the low and high energy peaks in Fig. 5.4(c), which come from the energy decreasing branch and the high energy branch in Fig. 5.4(a), respectively, is overestimated
- the extracted lifetime in Fig. 5.4(b), i.e., 372 fs, is over two times larger than that extracted from the experimental spectra, i.e.,  $150 \pm 50$  fs.

It is known to us that the ICD lifetime of an excited state can be approximated by the inverse of the ICD rate of the excited state. Thus, the discrepancy of the extracted ICD lifetimes between our simulation and the experiment clearly shows that the ICD rates from the two excited states in  $\text{Ne}_2^+$ , which is taken from Ref. [123] by the complex absorbing potential method, is underestimated by a factor of around 3 for the internuclear distances where the nuclear wave packets evolve along the potential energy curves for these two excited states. To confirm this, in Fig. 5.5, we show the similar results as in Fig. 5.4(b) by using new ICD rates which is 3 times larger than the rates in Ref. [123]. We can see that the new extracted lifetime, i.e., 167 fs, is much closer to the counterpart extracted from the experiment.

5.2. Nuclear KER spectra following triple ionization of  $\text{Ne}_2$  interacting with coherent XUV pulse

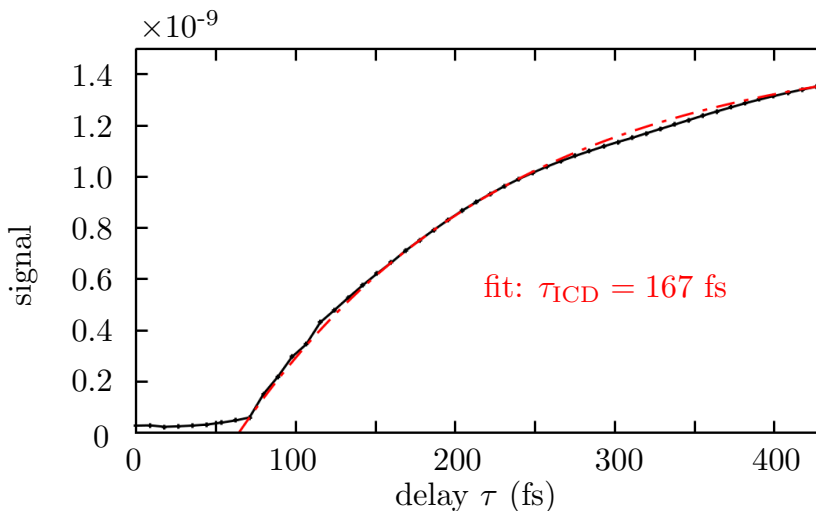


Figure 5.5: Yields of  $\text{Ne}^{2+}$  and  $\text{Ne}^+$  pairs similar as Fig. 5.4(b) when the ICD rates are three times larger.

Now we have a closer look at the low energy peak at around 5 eV and the high energy peak at around 9 eV Fig. 5.4(c). Compared with the ratio of the signals between the low and high energy peaks obtained in the experiment, our ratio indicates that the high (low) energy branches in Fig. 5.4 are relatively underestimated (overestimated) in our calculation. We can see that as the delay is increased, the signals at the energy decreasing branch would be increased until at a certain delay the signals saturate since the wave packets in the excited states in  $\text{Ne}_2^+$  are entirely prompted to the two-site outer-valence vacancy states in  $\text{Ne}_2^{2+}$  via ICD. While in the high energy branch, the signals at around 9 eV remain almost the same for delays larger than 250 fs. In fact, there are two channels that mainly result in the signals at the high energy branches, i.e.,

- the first photoionization by the pump (probe) pulse, a following fast ICD to  $\text{Ne}_2^{2+}$ , and the second photoionization by the pump (probe) pulse
- the first photoionization by the pump (probe) pulse, the second photoionization by the pump (probe) pulse and the following ICD to  $\text{Ne}_2^{3+}$

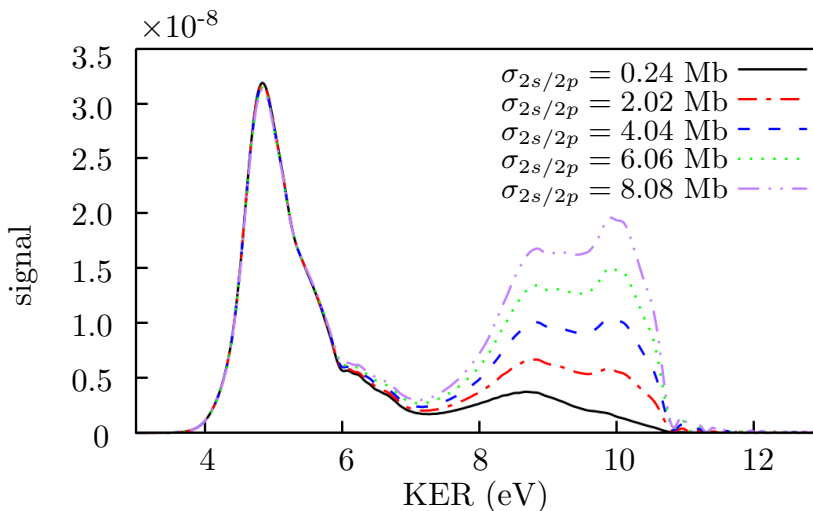


Figure 5.6: Nuclear KER spectra under different photoionization cross sections  $\sigma_{2s/2p}$  from the  $2^2\Sigma_g^+$  and  $2^2\Sigma_u^+$  states to  $\text{Ne}_2^{2+}$  at  $\tau = 400$  fs when the ICD rates are three times larger.

The intensities of the signals are directly related to the photoionization cross sections from  $\text{Ne}_2^+(1s^{-1})$  to  $\text{Ne}_2^{2+}(2p^{-2})$  and from  $\text{Ne}_2^{2+}(2p^{-2})$  to  $\text{Ne}_2^{3+}(2p^{-3})$ . In Fig. 5.6, we show the coincident  $\text{Ne}^+$  and  $\text{Ne}^{2+}$  KER spectra for five different photoionization cross sections from  $\text{Ne}_2^+(1s^{-1})$  to  $\text{Ne}_2^{2+}(1s^{-1}2p^{-1})$  at a very large delay. We take an example of a delay of 400 fs here and the obtained spectra would resemble the integrated spectra for delays between 300 fs and 420 fs as it is shown in Fig. 5.4(a) that the nuclear KER spectra nearly do not change at this delay region. The other laser parameters are same as that in Fig. 5.4. We can clearly see that the larger the photoionization cross sections are, the more important the second ICD channel is, and the more important the high energy branches would be. When the photoionization cross sections from  $\text{Ne}_2^+(1s^{-1})$  to  $\text{Ne}_2^{2+}(1s^{-1}2p^{-1})$  are taken to be 6.06 Mb, the ratio between the low and high energy peaks is around 2, which is close to the ratio obtained in Ref. [62]. Apart from that, when we increase the photoionization cross sections, a new energy peak at around 10 eV becomes more and more important, which do not appear in the experiment.

As we mentioned before, the photoionization cross from  $\text{Ne}_2^{2+}(2p^{-2})$



## 5.2. Nuclear KER spectra following triple ionization of Ne<sub>2</sub> interacting with coherent XUV pulse

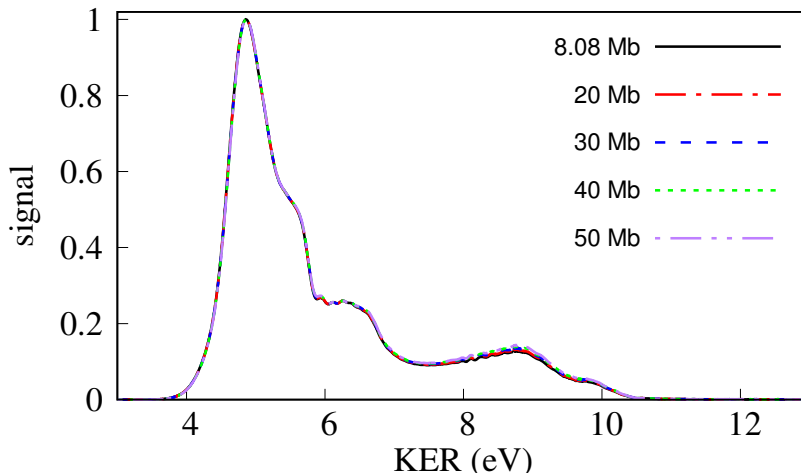


Figure 5.7: Nuclear KER spectra following triple ionization of Ne<sub>2</sub> at a 400-fs delay when the photoionization cross sections are taken 8.08, 20, 30, 40 and 50 Mb, respectively.

to Ne<sub>2</sub><sup>3+</sup>(2p<sup>-3</sup>) is approximated by the photoionization cross section from Ne<sup>+</sup>(2p<sup>-1</sup>) to Ne<sup>2+</sup>(2p<sup>-2</sup>). Actually, as we will show in the following, the ratio of the signals between the low and high energy peak is, to some extent, not relevant to the photoionization cross sections from Ne<sub>2</sub><sup>2+</sup>(2p<sup>-2</sup>) to Ne<sub>2</sub><sup>3+</sup>(2p<sup>-3</sup>). For example, the nuclear KER spectra following triple ionization of Ne<sub>2</sub> at the 400-fs delay for five different photoionization cross sections from Ne<sub>2</sub><sup>2+</sup>(2p<sup>-2</sup>) to Ne<sub>2</sub><sup>3+</sup>(2p<sup>-3</sup>) are presented in Fig. 5.7. To avoid the interferences from the second triple ionization channel, the results in Fig. 5.7 are obtained by only including the first triple ionization channel, i.e., first photoionization, then ICD and second photoionization. Thus, the almost identical five curves clearly show us that the choice of the photoionization cross sections from Ne<sub>2</sub><sup>2+</sup> to Ne<sub>2</sub><sup>3+</sup> has nothing to do with the discrepancy of the experimental and theoretical ratios of the signals between the low and high energy peaks.

As a result, based on the above analysis, we know that the discrepancies between the simulation and the experiment comes from the underestimated ICD rates and photoionization cross sections from Ne<sub>2</sub><sup>+</sup> to Ne<sub>2</sub><sup>2+</sup>. We show in Fig. 5.8 the nuclear KER spectra following triple

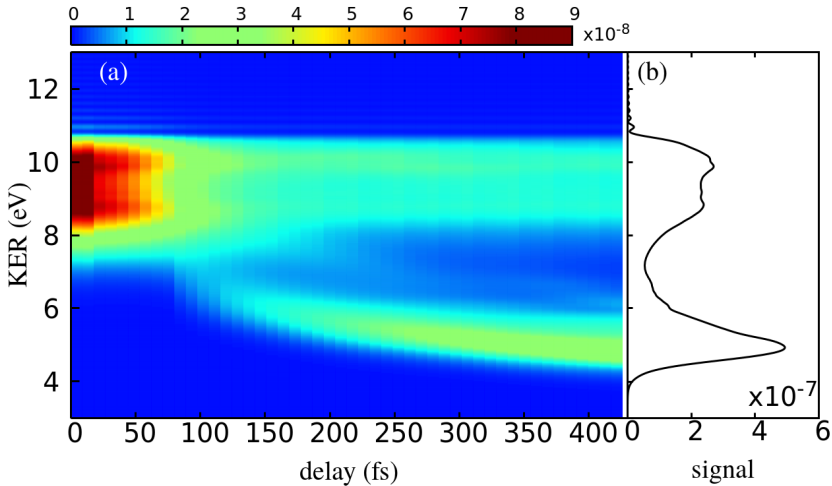


Figure 5.8: (Nuclear KER spectra as a function of delay (a) and sum of the nuclear KER spectra for delays between 300 and 420 fs (b) following triple ionization of  $\text{Ne}_2$  when interacting with coherent laser pulses. The laser parameters are same as Fig. 5.4. While the ICD rates are three times larger than that in Fig. 5.4 and the photoionization cross section from  $\text{Ne}_2^+$  to  $\text{Ne}_2^{2+}$  are taken as 6.06 Mb.

ionization of  $\text{Ne}_2$  when we take the ICD rates three times larger and the photoionization cross sections from  $\text{Ne}_2^+$  to  $\text{Ne}_2^{2+}$  are increased to 6.06 Mb. The laser parameters are identical to Fig. 5.4. We do not show here the integrated signals from 3 to 7 eV as a function of delay, which is similar to Fig. 5.4(c), since it is quite similar to Fig. 5.5 because of the same ICD rates are employed. Compared with Fig. 5.4, even though we have a better ratio of the signals between the low and high energy peaks, we have also obtained relatively much larger signals at delays smaller than 70 fs due to the constructive coherence between the pump and probe pulses. The intensities of the signals at these small delays, as we show in the next section, would be not so significant when chaotic pump and probe pulses are applied because of the reduced coherence time of the pulses.

### 5.3 Nuclear KER spectra following triple ionization of $\text{Ne}_2$ interacting with chaotic XUV pulses

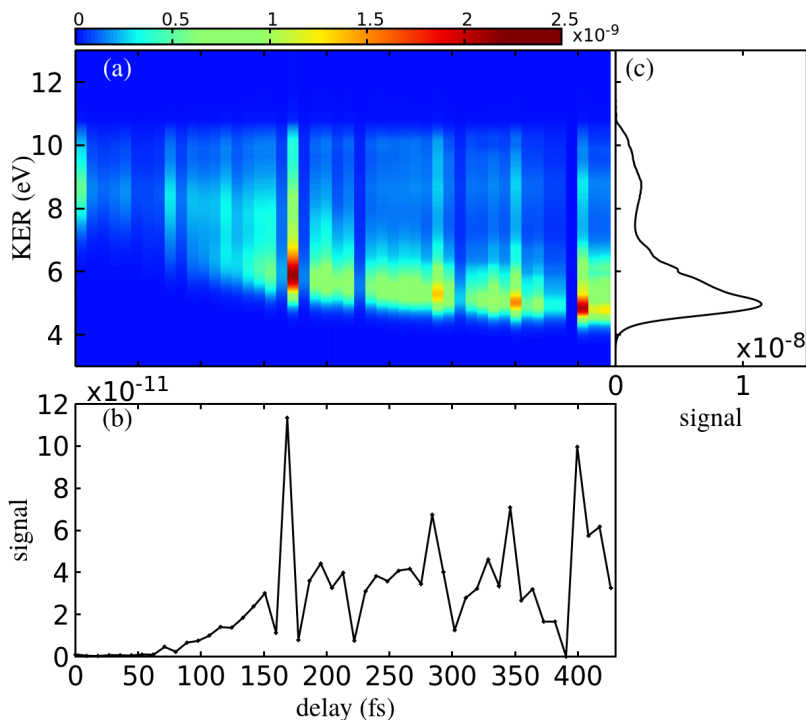


Figure 5.9: (a) Calculated nuclear KER spectra for coincident  $\text{Ne}^{2+}$  and  $\text{Ne}^+$  fragments following triple ionization of  $\text{Ne}_2$  as a function of delay  $\tau$  when the applied laser pulses are modeled by the partial coherence method. (b)  $\text{Ne}^{2+}$  and  $\text{Ne}^+$  yields integrated over all KERs for all the delays in (a). (c) Sum of nuclear KER spectra for delays between 300 and 400 fs. The ICD rates and photoionization cross sections are same as Fig. 5.4.

In this section, we present the results for  $\text{Ne}_2$  interacting with chaotic XUV pulses modeled by the partial coherence method which has been described in detail before. The laser parameters are same as Fig. 5.3 and the pump and probe pulses are identical. The other

parameters such as the ICD rates and the photoionization cross sections are taken originally, i.e., same as Fig. 5.4. In Fig. 5.9(a), we show the similar nuclear KER spectra, i.e., following triple ionization of  $\text{Ne}_2$  by applying the chaotic pulses. Due to the fact that the XUV pulses are different from shot to shot, the XUV pulse is modeled at each delay. This is the reason the nuclear KER spectra in Fig. 5.9(a) as a function of delay is not as smooth as the coherent case. Similarly, we can observe the high energy branch centered around 9 eV and the energy decreasing branch. Similar to Fig. 5.4(c), we have obtained a similar ratio of the signals between the low and high energy peaks in Fig. 5.9(c). Because of the variations of the signals originating from the random noises in Fig. 5.9(b), it is different to extract the ICD lifetime from Fig. 5.9(b). Extraction of the lifetime would be possible only if we average the nuclear KER spectra for many realizations.

Finally, we run a simulation where we take the new ICD rates which are three times larger than the original rates and assume new photoionization cross sections of 6.06 Mb. The corresponding results are shown in Fig. 5.10. Similar to Fig. 5.9(a), the energy decreasing branch and the high energy branch are reproduced. Apart from that, just as expected, we can clearly observe an enhancement of the high energy branch in Fig. 5.10(a) compared with Fig. 5.9(a). Similar to the coherent case in Fig. 5.8(c), a broadening of the high energy peak is also observed.

## 5.4 Concluding remarks

In this chapter, we have taken the example of  $\text{Ne}_2$  to study the nuclear dynamics in weakly bounded clusters. Due to the relatively weak interaction between the constituent atoms in clusters, new electronic decay channels, such as the ICD process, become possible in weakly bounded clusters. The ICD process is an electron decay process where after removing an inner-valence electron from one atom in the cluster, the remaining cation is highly excited and thus can decay to more stable states by emitting another electron. Impressed by a recent XUV-pump-XUV-probe experiment [62], we have investigated the ICD processes in  $\text{Ne}_2$  by applying the MCWP approach to obtain the nuclear KER spectra following triple ionization of  $\text{Ne}_2$ . The involved triple ioniza-

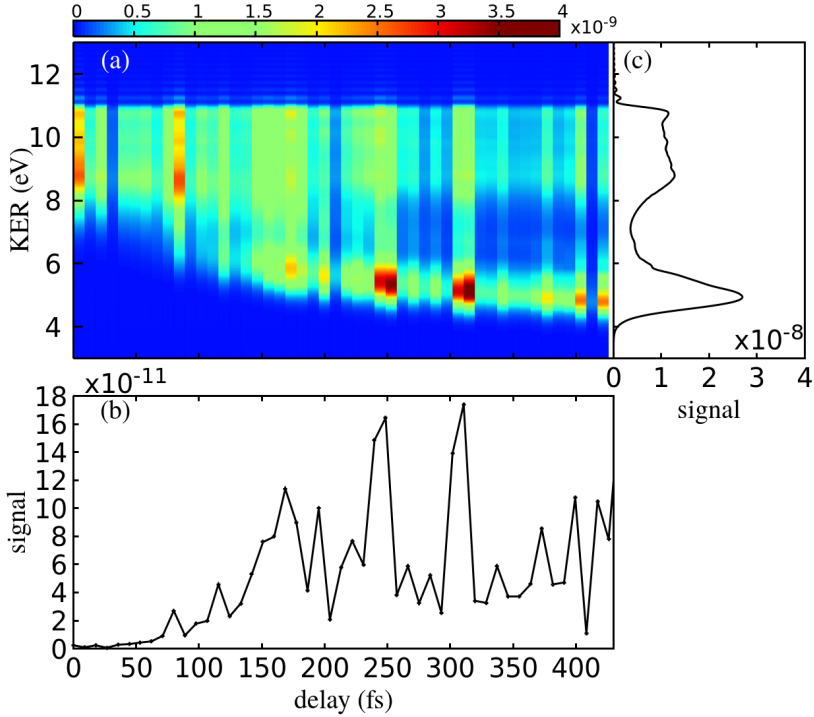


Figure 5.10: Similar results as Fig. 5.9 where the  $R$ -dependent ICD rates are three times larger and the photoionization cross sections from  $\text{Ne}_2^+$  to  $\text{Ne}_2^{2+}$  are 6.06 Mb.

tion process is as follows: one  $2s$  inner-valence electron is first removed from  $\text{Ne}_2$  by absorbing one photon from the XUV pulse, then the second ionization takes the remaining  $\text{Ne}_2^+$  to  $\text{Ne}_2^{2+}$  either via  $\text{Ne}_2^+(1s^{-1})$  to  $\text{Ne}_2^{2+}(1s^{-1}2p^{-1})$  by the second photoionization or via  $\text{Ne}_2^+(1s^{-1})$  to  $\text{Ne}_2^{2+}(2p^{-2})$  by ICD, and the third ionization takes  $\text{Ne}_2^{2+}(1s^{-1}2p^{-1})$  or  $\text{Ne}_2^{2+}(2p^{-2})$  to  $\text{Ne}_2^{3+}(2p^{-3})$  by ICD or the second photoionization. We have obtained the nuclear KER spectra following the above mentioned triple ionization of  $\text{Ne}_2$  and reproduced the two important features, i.e., the high energy branch and the energy decreasing branch in the nuclear KER spectra obtained by that experiments. Apart from that, an analysis of the discrepancies between our simulation and the experiment, i.e., the extracted ICD lifetime and the ratio of the signals

between the low and high energy peaks in the nuclear KER spectra at large delays, conveys us that the ICD rates obtained by the complex absorbing method in Ref. [123] are underestimated by over two times and we can make a more accurate estimate of the photoionization cross sections from  $\text{Ne}_2^+$  to  $\text{Ne}_2^{2+}$ .

---

## Summary and outlook

In this thesis, we have applied the MCWP approach to investigate the nuclear dynamics following ionization and excitation in small molecules and weakly bound clusters through interacting with intense laser pulses. We have presented a detailed description of the implementation of the MCWP approach and its equivalence to the master equation in the Lindblad form in Chapter 3. In Chapter 4, we mainly studied the dissociative double ionization of  $\text{H}_2$ . We first studied the influences of parameters including the central wavelength, pulse duration, peak intensity and nuclear mass on the nuclear KER spectrum following full break-up of  $\text{H}_2$  interacting with single IR laser pulses. Besides, we showed the unique possibility of the MCWP approach by conducting a trajectory analysis to a given feature in a nuclear KER spectrum. Then we investigated the nuclear dynamics in the singly excited states in  $\text{H}_2$  by using the XUV-pump-IR-probe spectroscopy. After that, we studied the nuclear dynamics following single ionization of  $\text{H}_2$  either via photoionization or autoionization from the doubly excited states when exposed to XUV pulses. In Chapter 5, we extended the MCWP approach to investigate triple ionization of the neon dimer to study the ICD process in  $\text{Ne}_2$  by using XUV-pump-XUV-probe spectroscopy. We have reproduced the nuclear KER spectra following triple ionization of  $\text{Ne}_2$  obtained by a recent experiment [62], which is beyond the capability of the other quantum methods.

Throughout this thesis, we solve the simplified one-dimensional coupled equations for the motion of the nuclei since we assume the

molecule and cluster is rotational frozen. We can later take the rotational motion of the nuclei into consideration by solving the more complicated three-dimensional equations for the nuclear motion. Besides, the laser polarization directions are assumed to be parallel to the molecular axis and only the transition from the states of  $\Sigma$  symmetries to the states of  $\Sigma$  symmetries are involved. When there are electric field components at the directions perpendicular to the molecular axis, for example, circularly or elliptically polarized laser pulses, other transitions from the states of a given symmetry to the states of different symmetries should be considered.

The present study of the influence of the doubly excited states on the nuclear KER spectra is not sufficient. On the one aspect, there are some discrepancies between our simulation and the results obtained by the experiment and another theoretical method. We should put more efforts on figuring out the origins of the discrepancies. On the other aspect, we have only studied the interaction of  $H_2$  with single XUV pulses. An extended study of the interaction of  $H_2$  with laser pulses in a pump-probe setup is worthy to carry out to map out the nuclear dynamics from the nuclear KER spectra as a function of delay.

Apart from the ICD process studied in Chapter 5, we can apply the MCWP method to investigate other electronic decay processes, such as the ETMD process, in weakly bounded clusters. For the ETMD process, the inner valence hole in one atom is filled by one outer valence electron in its neighboring atom and the energy released by this transition supports to remove another electron from the neighboring atom. Different from ICD, after ETMD taking place, there is no hole in the first atom and there are two outer-valence holes in the second atom. Thus, there is no Coulomb explosion between the two atoms and the remaining ion may remain weakly bounded. As a result, one can apply a similar XUV-pump-XUV-probe setup as applied in the ICD case to study the nuclear dynamics within an ETMD process by obtaining the nuclear KER spectra following triple ionization of a weakly bound cluster.



# Part II

## Publications

---

# My First Paper

Paper I. PHYSICAL REVIEW A 94, 063402 (2016)

*Title:*

**Laser-induced dissociative ionization of H<sub>2</sub> from the near-infrared to the mid-infrared regime**

*Authors: Qingli Jing and Lars Bojer Madsen*

DOI: <https://doi.org/10.1103/PhysRevA.94.063402>

Reprinted with permission from the American Physical Society. Copyright (2016) by the American Physical Society.

My contribution to this publication: (1) implementation of the theoretical calculations and (2) preparation of the manuscript (with figures).

**Laser-induced dissociative ionization of H<sub>2</sub> from the near-infrared to the mid-infrared regime**

Qingli Jing and Lars Bojer Madsen

*Department of Physics and Astronomy, Aarhus University, 8000 Aarhus C, Denmark*

(Received 6 October 2016; published 2 December 2016)

We apply the Monte Carlo wave packet (MCWP) approach to investigate the kinetic energy release (KER) spectra of the protons following double ionization in H<sub>2</sub> when interacting with laser pulses with central wavelengths ranging from the near-infrared (IR) (800 nm) to the mid-IR (6400 nm) regions and with durations of 3–21 laser cycles. We uncover the physical origins of the peaks in the nuclear KER spectra and ascribe them to mechanisms such as ionization following a resonant dipole transition, charge-resonance-enhanced ionization, and ionization in the dissociative limit of large internuclear distances. For relatively large pulse durations, i.e., for 15 or more laser cycles at 3200 nm and 10 or more at 6400 nm, it is possible for the nuclear wave packet in H<sub>2</sub><sup>+</sup> to reach very large separations. Ionization of this part of the wave packet results in peaks in the KER spectra with very low energies. These peaks give direct information about the dissociative energy in the  $2p\sigma_u$  potential energy curve of H<sub>2</sub><sup>+</sup> at the one- and three-photon resonances between the  $2p\sigma_u$  and  $1s\sigma_g$  curves in H<sub>2</sub><sup>+</sup>. With the MCWP approach, we perform a trajectory analysis of the contributions to the KER peaks and identify the dominant ionization pathways. Finally, we consider a pump-probe scheme by applying two delayed pulses to track the nuclear dynamics in a time-resolved setting. Low-energy peaks appear for large delays and these are used to obtain the  $2p\sigma_u$  dissociative energy values at the one-photon resonance between the  $2p\sigma_u$  and  $1s\sigma_g$  curves in H<sub>2</sub><sup>+</sup> for different wavelengths.

DOI: [10.1103/PhysRevA.94.063402](https://doi.org/10.1103/PhysRevA.94.063402)**I. INTRODUCTION**

The significant advances made in femtosecond laser technology have opened the possibility of controlling chemical reactions with laser light [1–3]. When exposing molecules to intense laser pulses, strong interaction between molecules and the external electromagnetic field may give rise to electronic excitation or even result in ionization. Nuclear dynamics is hence often induced because of the interplay between the nuclei and electrons. A good example is the process of dissociative ionization [4,5], a process in which dissociation is induced as a result of the removal of one or more electrons. Laser-induced dissociative ionization has received considerable interest in the past two decades [6–8]. Thanks to the fast developments in imaging techniques such as COLTRIMS [9] and VMI spectrometers [10], it is now possible to measure the kinetic energy of the ionic fragments or the liberated electrons or both. By analyzing the kinetic energy release (KER) spectra of the ionic fragments, information about the ionization process can be obtained [11]. For example, the processes of charge-resonance-enhanced ionization (CREI) [12,13] and resonance-enhanced multiphoton ionization [14,15] both manifest themselves through the occurrence of characteristic peaks in the nuclear KER spectra [16]. Different from the mechanism of resonance-enhanced multiphoton ionization, for one-electron system like H<sub>2</sub><sup>+</sup>, CREI results from lowering the internal barrier between the double wells at certain critical internuclear separations in the presence of a strong field, along with the creation of a pair of field-dressed charge-resonant states.

In parallel to the advances in experimental techniques, many theoretical methods [17–19] have been developed and proven to work very well in describing a range of phenomena associated with the interaction of molecules and light. Among these methods, the Monte Carlo wave packet (MCWP) approach [20,21] performs well when describing the laser-induced dissipative dynamics. Especially in previous works

on H<sub>2</sub> [22,23], and O<sub>2</sub> [24], where the nuclear KER spectra were of main concern, the simulations agreed very well with the measurements. This approach, like many others, is devoted to solving the time-dependent Schrödinger equation (TDSE), but the problem is greatly simplified because the electronic degrees of freedom are treated in an effective description. At the same time, the Markov approximation [25] is applied, which means that the flow of electrons from the molecular systems to the surroundings is unidirectional and irreversible. The loss of electrons is encoded in jump operators, which are responsible for jumps among different Hilbert spaces and constitute a non-Hermitian part of the total Hamiltonian. The non-Hermitian Hamiltonian implies that the norm of the system is decreasing over time. The drop of the norm over time is controlled by the instantaneous ionization rates [26,27] of the system. If the ionization rates depend on the nuclear configuration, wave-packet motion is induced in the neutral molecule. Inducing nuclear dynamics in this way is called Lochfraß [28–30] and this phenomenon is an integrated part of the MCWP simulations.

In the present MCWP approach to dissociative ionization, the jumps between different charge states and associated Hilbert spaces are described by ionization rates. While the evolution of the system within a given charge state is coherent, the rate treatment of the ionization step means that coherence between the remaining cation and the ionized electron is lost. Also we have no knowledge of the energy distribution of the outgoing electron.

Recently there has been a shift in strong-field physics toward the use of mid-infrared (IR) driving wavelengths [31], e.g., to image molecular structures by light-induced electron diffraction [32,33] and to greatly increase the photon energies of high-harmonic generation [34]. The interaction between the mid-IR laser pulses and molecules can be treated in the quasistatic regime. The systematic investigation of the behavior of the nuclear KER spectra with increasing wavelength from

the near-IR region to the mid-IR region and the underlying physics when going to longer wavelengths is the topic of the present work. The large wavelengths of the intense IR laser pulses make the ionization dynamics of molecules enter the regime of tunneling ionization [35–38]. Studying the peaks in the KER spectra at mid-IR wavelengths can help us obtain detailed knowledge of the nuclear motion, as will be discussed below. As a characteristic trend in the spectra, we see a shift toward lower KER values with increasing wavelength.

The paper is organized as follows. In Sec. II, we review how to apply the MCWP method to simulate dissociative ionization in  $H_2$ . In Sec. III, we discuss the KER spectra obtained for  $H_2$  exposed to laser pulses with different wavelengths and pulse durations. In Sec. IV, the nuclear KER spectra of  $H_2$  interacting with pump-probe pulses with delays are analyzed. Sec. V concludes. Atomic units ( $\hbar = e = m_e = a_0 = 1$ ) are used throughout unless stated otherwise.

## II. MCWP APPROACH FOR DISSOCIATIVE IONIZATION OF $H_2$

The MCWP approach for dissociative ionization was described in detail elsewhere [21–24,40], so the description here is brief. The dissipative dynamics of a diatomic molecule interacting with laser light can be described by the TDSE

$$i\partial_t|\Psi(t)\rangle = H(t)|\Psi(t)\rangle = \left(H_s - \frac{i}{2} \sum_m C_m^+ C_m\right)|\Psi(t)\rangle, \quad (1)$$

with the Hermitian Hamiltonian

$$H_s = T_N + V_N + V_{eN} + T_e + V_{ee} + V_I(t), \quad (2)$$

where  $T_N$  is the kinetic energy operator for the nuclei,  $T_e$  the kinetic energy for the electrons,  $V_N$  the nuclear repulsion,  $V_{eN}$  the nuclei-electron interaction,  $V_{ee}$  the electron-electron interaction, and  $V_I(t)$  the laser-matter interaction. Within the Born-Oppenheimer approximation, the total state  $|\Psi(t)\rangle$  can be expanded as

$$|\Psi(t)\rangle = \sum_m \int d\vec{R} X_m(\vec{R}, t) |\phi_{R,m}^{\text{el}}\rangle \otimes |\vec{R}\rangle, \quad (3)$$

in which  $X_m(\vec{R}, t)$  is the nuclear wave packet and  $|\vec{R}\rangle$  refers to the position eigenkets of the nuclear coordinate. The electronic basis states  $|\phi_{R,m}^{\text{el}}\rangle$  can be obtained by solving the time-independent Schrödinger equation with parametric dependence on the internuclear separation  $\vec{R}$ :

$$(T_e + V_{ee} + V_{eN} + V_N) |\phi_{R,i}^{\text{el}}\rangle = E_{\text{el},i}(R) |\phi_{R,i}^{\text{el}}\rangle, \quad (4)$$

where  $E_{\text{el},i}(R)$  is the corresponding electronic potential energy curve. The four electronic potential energy curves included in our MCWP calculations are shown in Fig. 1. These are the  $(1s\sigma_g)^2$  curve in  $H_2$ , the  $1s\sigma_g$  and  $2p\sigma_u$  curves in  $H_2^+$ , and the doubly ionized Coulombic curve in  $H_2^{++}$ , for short denoted  $h$ ,  $g$ ,  $u$ , and  $c$ , respectively. These curves were previously shown to be sufficient to capture the dynamics responsible for the KER spectra [21–23]. The jump operators  $C_m$  in Eq. (1) constitute a non-Hermitian term in the total Hamiltonian. This term is responsible for the jumps among the different Hilbert

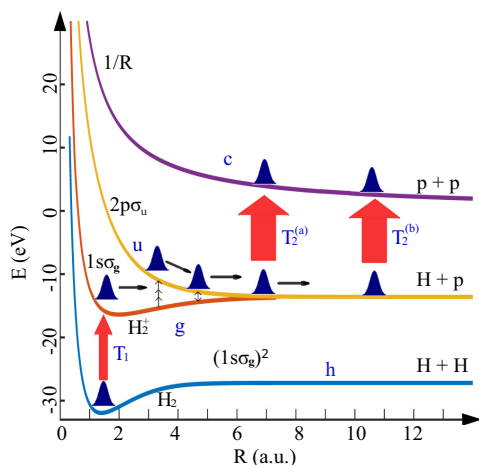


FIG. 1. Sketch of four field-free Born-Oppenheimer electronic potential energy curves [39]. These curves are the  $(1s\sigma_g)^2$  ground-state curve in  $H_2$  labeled by  $h$ , the  $1s\sigma_g$  and  $2p\sigma_u$  curves in  $H_2^+$  labeled by  $g$  and  $u$ , respectively, and the  $1/R$  Coulombic curve labeled by  $c$ . A particular realization of a quantum trajectory with the MCWP approach is also shown: At some instant  $T_1$ , the first ionization occurs and the neutral wave packet is promoted to the singly ionized system where coherent evolution takes place. At some later instant  $T_2^j$  ( $j = a, b$ ), the second ionization occurs and then the nuclei undergo Coulomb repulsion. The final energy of the protons depends on the instants  $T_1, T_2^j$ .

spaces of  $H_2$ ,  $H_2^+$ , and  $H_2^{++}$ ,

$$C_m = \int d\vec{R} \sqrt{\Gamma_m(\vec{R}, t)} |\phi_{R,n}^{\text{el}}\rangle \langle \phi_{R,m}^{\text{el}}| \otimes |\vec{R}\rangle \langle \vec{R}|, \quad (5)$$

where  $\Gamma_m(\vec{R}, t)$  is the ionization rate from the  $m$  ( $h$ ,  $g$ , or  $u$ ) state to the  $n$  ( $g$ ,  $u$ , or  $c$ ) state and depends on the instantaneous value of the field strength. In this work, the ionization rate responsible for the ionization of  $H_2$  is calculated using the weak-field asymptotic theory of Ref. [37]. The ionization rates for the ionization of the cation are obtained by interpolating the results published in Ref. [41].

By substituting Eqs. (3)–(5) into Eq. (1) and using the ansatz  $X_m(\vec{R}, t) = \frac{1}{R} K_m(R, t) W_m(\theta, \phi, t)$ , the time evolution of the radial wave function  $K_m(R, t)$  can be obtained. As the molecule is assumed rotationally frozen during the interaction with the femtosecond laser pulse, the angular parts of the nuclear wave function  $W_m(\theta, \phi, t)$  can be expressed as  $W_m(\theta, \phi, t) = \frac{1}{\sqrt{4\pi}} \delta(\theta - \theta_0) \delta(\phi - \phi_0)$  with  $\theta_0$  and  $\phi_0$  specifying the internuclear orientation. In the calculations below, we consider the case where the molecule is aligned with the linear polarization of the external field, i.e.,  $\theta_0 = 0^\circ$  and  $\phi_0 = 0^\circ$ , where the latter can be arbitrary because of symmetry.

The simulation procedure of the MCWP technique is outlined in the following (see also Refs. [21–23]). The nuclear wave function first evolves in the neutral system with its norm square decreasing because of the non-Hermitian term in the

Hamiltonian. At each time step, the drop in the norm square is compared with a random number (between 0 and 1), which determines whether the jump from one Hilbert space to another takes place or not. If the drop in the norm square is larger than the random number, ionization occurs and thus the wave function jumps, is renormalized, and then evolves in the new Hilbert space, otherwise, ionization cannot occur and the wave function needs to be renormalized in the neutral system. The comparison between the drop in the norm square and a random number continues until the first jump occurs. Similarly, whether the second jump takes place or not is controlled by comparing the drop in the norm square of the nuclear wave function in  $H_2^+$  with a new random number (between 0 and 1). The difference compared to the first jump is that there are two pathways for the second jump to the doubly ionized system, from the  $g$  state curve and from the  $u$  state curve, which means that another random number (between 0 and 1) should be introduced to decide which pathway to choose. As a result, a nuclear wave function after emitting two electrons is obtained stochastically, with the first jump occurring at some instant of time  $T_1$  and the second jump at some instant of later time  $T_2$  (Fig. 1). The nuclear wave packet after two jumps  $K_c(R, T_2)$  holds all the information of the nuclei. For example, the nuclear kinetic energies can be obtained by projecting the wave packet on Coulomb waves  $K_E(R)$ ,

$$E_m^{\text{KER}}(T_1, T_2) = \left| \int K_E(R) K_c(R, T_2) dR \right|^2, \quad (6)$$

with  $m = g, u$ .

Equation (6) only gives the KER signal for one stochastic event occurring at specific  $T_1$  and  $T_2$ . We refer to such a specific realization of jump times and dynamics as a quantum trajectory. The total nuclear KER spectra of the dissociative ionization process can be obtained by averaging over all the stochastic events. In the present case of dissociative double ionization, the computational effort can, however, be dramatically reduced through eliminating all the random numbers by applying a completely deterministic approach. To this end, the two jumps which are dressed with probabilities are assumed to take place at every time step. Actually, the probability for each jump is proportional to the drop in the norm square at that jump time. This is reasonable because the larger the drop in the norm square, the more likely it is for a jump to occur. Summing over all the weighted events, the nuclear KER spectra can be obtained from the formula,

$$E_{\text{tot}}^{\text{KER}} = \sum_{T_1, T_2} P_1 P_{12} \sum_{m=g, u} P(m|\{T_1, T_2\}) E_m^{\text{KER}}(T_1, T_2). \quad (7)$$

In the above equation,  $P_1 = -d(N_h(t))/dt$  is the probability density for the first jump with  $N_h(t)$  representing the norm square of the nuclear wave function of the  $h$  state;  $P_{12} = -d(N_g(t) + N_u(t))/dt$  is the conditional probability density of the second jump for a given first jump with  $N_g(t)$  and  $N_u(t)$  representing the norm square of the nuclear wave function of the  $g$  state and the  $u$  state, respectively; and  $P(m|\{T_1, T_2\}) = \langle \Psi | C_m^\dagger C_m | \Psi \rangle / \langle \Psi | C_g^\dagger C_g + C_u^\dagger C_u | \Psi \rangle$  is the conditional probability density from the  $m$  ( $g$  or  $u$ ) state for given first and second jump times (see also Ref. [40]).

As shown in Fig. 1, the initial nuclear wave function is assumed to be the ground state of the  $(1s\sigma_g)^2$  potential energy

curve of  $H_2$ . The applied laser pulse with the polarization axis parallel to the molecular axis first kicks out the first electron and then induces nuclear motion in the two potential energy curves of the  $H_2^+$  system. Meanwhile, there is electronic dipole coupling between the  $1s\sigma_g$  and  $2p\sigma_u$  states. Finally, the nuclei experience Coulomb repulsion after emitting the second electron. Thus the nuclei pick up energy from two terms, one is the dissociative kinetic energy in the singly ionized system and the other is the Coulomb repulsion energy in the doubly ionized system. The time-dependent Hamiltonian, including the non-Hermitian part representing the interaction between states in different Hilbert spaces as well as the electronic dipole coupling between states within a given Hilbert space, originates from the external laser field. As a result and as shown in the next section, the kinetic energy is closely related to the parameters of the applied laser pulse, such as peak intensity, wavelength, and pulse duration.

Numerically, within each Hilbert space, we solve the TDSE by applying the split-operator method [42] on the short-time propagator, i.e.,

$$U(t + \Delta t, t) = \exp\left(-iT_N \frac{\Delta t}{2}\right) \exp\left[-iV\left(R, t + \frac{\Delta t}{2}\right) \Delta t\right] \times \exp\left(-iT_N \frac{\Delta t}{2}\right). \quad (8)$$

Obviously, it is the term  $V(R, t)$  that determines how the wave packet evolves in each Hilbert space. For example, in  $H_2^+$ , the  $2 \times 2$  matrix representation of  $V(R, t)$  is  $V_{ij}(R, t) = E_{\text{el},i}(R) \delta_{ij} - i\Gamma_i(R, t)/2\delta_{ij} + \beta D_{ij}(R) F(t)$  ( $i, j = g, u$ ), where  $\beta = 1 + 1/(2m_p + 1)$  with  $m_p$  the proton mass,  $F(t)$  is the electric field, and  $D_{ij}(R)$  is the electronic dipole moment function between  $i$  and  $j$  states along the direction  $\hat{e}$  of the linear polarization, i.e.,  $D_{ij}(R) = -\langle \phi_{R,i}^{\text{el}} | \vec{r} \cdot \hat{e} | \phi_{R,j}^{\text{el}} \rangle$ . We use the explicit expression for  $D_{gu}(R) = \frac{R}{2\sqrt{1 - [(1+R+R^2/3)e^{-R}]^2}} - \frac{1}{(2+1.4R)}$  given in Ref. [43]. The size of our simulation box is 40.96. The time step  $\Delta t$  is 0.1 and the spatial step  $\Delta R$  is 0.02. The operators  $\exp(-iT_N \frac{\Delta t}{2})$  and  $\exp[-iV(R, t + \frac{\Delta t}{2}) \Delta t]$  are diagonal in the momentum and position representations, respectively, thus a fast-Fourier-transform algorithm is applied in the implementation.

### III. WAVELENGTH AND PULSE DURATION DEPENDENCE OF KER SPECTRA FOR $H_2$ INTERACTING WITH A SINGLE LASER PULSE

In this section, we simulate the process of dissociative double ionization of ground-state  $H_2$  interacting with single laser pulses. The calculated proton KER spectra for different wavelengths (ranging from 800 to 6400 nm) and pulse durations (ranging from 3 to 21 laser cycles) are shown in Fig. 2. In our calculation, the laser pulses are of Gaussian shape, and the pulse durations are expressed in terms of the number of laser cycles within the FWHM of the intensity profile of the applied laser pulses. The laser intensity of  $6 \times 10^{13}$  W/cm<sup>2</sup> is chosen to be similar to the one in the experiment of Ref. [44]. If there are specific internuclear positions from which a significant part of the second ionization takes place, distinctive peaks occur in the nuclear KER spectra.

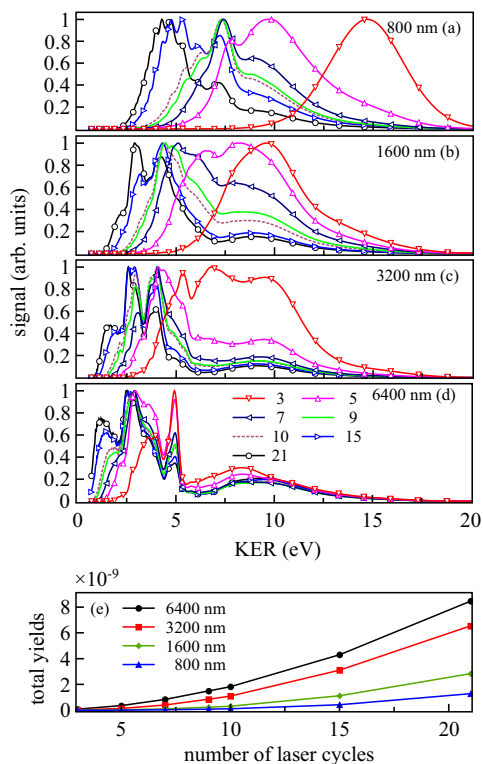


FIG. 2. (a)–(d) Renormalized nuclear KER spectra after double ionization of  $\text{H}_2$  interacting with laser pulses with different wavelengths ranging from 800 to 6400 nm and with different FWHM pulse durations ranging from 3 to 21 laser cycles. All the pulses have a peak intensity of  $6 \times 10^{13} \text{ W/cm}^2$ . (e) Total yields of protons in units of ionization probability per molecule as a function of the number of laser cycles for several wavelengths.

These peaks mostly come from events in  $\text{H}_2^+$  which occur at internuclear separations with a resonant one- or three-photon dipole coupling between the  $1s\sigma_g$  and  $2p\sigma_u$  curves, or at the separations of CREI [12, 13], or in the dissociative limit beyond the CREI distances. When we look at Fig. 2 from the top to the bottom, we see in general that the KER spectra move toward lower kinetic energies with increasing duration of the laser pulses. This behavior occurs because the larger the duration of the pulse, the more likely it is for the nuclei to dissociate to larger separations with correspondingly smaller repulsive Coulomb energy. Moreover, when interacting with laser pulses with the same duration, for example, 10 laser cycles at 800 nm and 5 laser cycles at 1600 nm, even though the individual peaks are shifted because of the different positions for the resonant electronic dipole coupling in  $\text{H}_2^+$ , the overall widths of the KER spectra windows look quite similar.

We will now identify the most prominent peaks in the spectra in Fig. 2. The special KER peak around 9 eV visible in Figs. 2(a)–2(d), is a signature of the outer turning point of the nuclear wave packet evolving along the  $1s\sigma_g$  Born-Oppenheimer (BO) potential energy curve in  $\text{H}_2^+$ . The peak is nearly independent of the laser pulse and is in nice agreement with the classical estimate of the Coulomb repulsion energy of  $1/R_{\text{tp}} \sim 1/3$  (9.1 eV), with  $R_{\text{tp}} \sim 3$  the outer turning point of the wave packet along the  $1s\sigma_g$  potential energy curve, when the initial nuclear wave packet is assumed to be that of the ground state of the  $(1s\sigma_g)^2$  curve with an equilibrium internuclear separation of 1.4.

For a fixed wavelength, several peaks in the KER spectra are more or less at similar positions for different numbers of laser cycles within the FWHM intensity duration. This behavior is a signature of the fact that the positions of the resonant electronic one- and three-photon dipole couplings are the same for these laser pulses. Moreover, there are clear signatures of CREI [13] in the spectra. CREI takes place at internuclear separations around  $R = 7$  and  $R = 11$  [41] at this laser peak intensity, and gives rise to Coulomb repulsive energies of 3.9 and 2.5 eV. When the wavelength is larger, the distances between positions for the one- or three-photon resonance and positions for CREI are smaller, and thus the dissociative kinetic energy picked up along the  $2p\sigma_u$  curve before the CREI positions is becoming smaller. The peaks around 3 eV (smaller than the Coulomb repulsion at  $R = 7$ ) in Figs. 2(b)–2(d) is a signature of CREI around  $R = 11$ , while in Fig. 2(a) the pulse durations are too short to allow a substantial portion of the nuclear wave packet to reach  $R = 11$  during the pulse.

When interacting with laser pulses with larger wavelengths, see Figs. 2(c) and 2(d), some pronounced new energy peaks appear around 1.5 eV when the number of laser cycles is larger than 15 (10) for 3200 nm (6400 nm). These peaks occur because the nuclear wave packet can move farther during the longer pulse and be ionized at separations beyond the positions of CREI. These low-energy peaks are of the same origin as the  $< 2$  eV peak monitored in a previous pump-probe experiment [45]. The low-energy peaks for 15 and 21 laser cycles at 6400 nm are at about 1.5 eV and 1.2 eV, respectively. We benefit from the stochastic sampling within the MCWP approach and carry out a trajectory analysis of these two peaks. The contributions from different trajectories are shown in Fig. 3. The ionization rate from the  $2p\sigma_u$  state to the doubly ionized molecule is at least one order of magnitude larger than that from the  $1s\sigma_g$  state for  $R \geq 3$  [41]. Moreover, only a very small part of the nuclear wave packet reaches distances  $R > 3$  via evolution on the  $1s\sigma_g$  curve. Thus the nuclear wave packet evolving along the  $2p\sigma_u$  curve contributes much more to the low-energy KER peaks. As a result, only trajectories where the second jump takes place from the  $2p\sigma_u$  state are shown in Fig. 3. A clear oscillatory dependence of the signal on the second jump time  $T_2$  can be observed. This is because all the first jumps take place at the field extrema and there are enhancements when the second jumps occur near field extrema. The time differences between the second and first jumps are the evolution times within the  $\text{H}_2^+$  system. The evolution times for the most prominent events (marked by red dots) for 21 and 15 laser cycles are about 6190 (150 fs) and 4420 (108 fs), which correspond to 7 and 5 laser cycles, respectively.

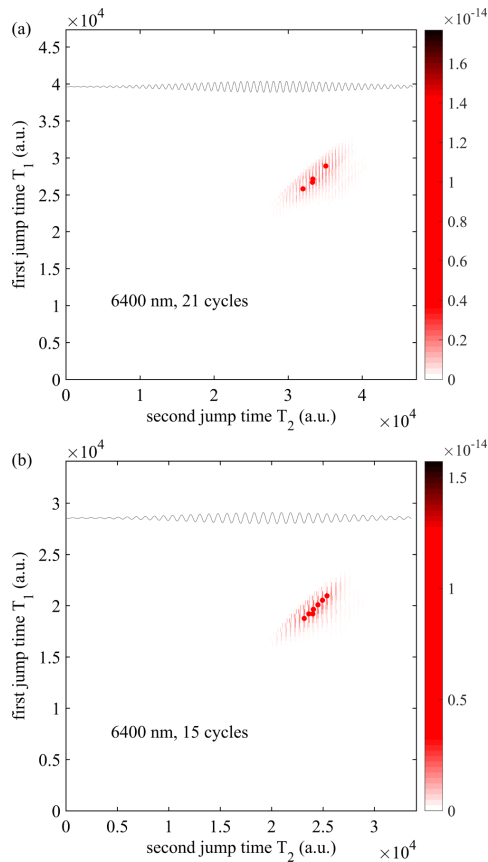


FIG. 3. Contributions from different trajectories to the low-energy peak around (a) 1.2 eV in Fig. 2(d) when interacting with a pulse with 21 laser cycles at 6400 nm, and (b) 1.5 eV in Fig. 2(d) when interacting with a pulse with 15 laser cycles at 6400 nm. The red dots mark the trajectories that give the largest contributions. The laser pulses are indicated by the grey lines and the parameters are as in Fig. 2(d).

In this manner, the MCWP approach allows us to find the typical time spent in the  $\text{H}_2^+$  system, i.e., the time needed to ionize  $\text{H}_2^+$ , for each particular feature in the KER spectra. These times are long enough for the nuclear wave packets to reach quite large internuclear separations ( $R > 20$ ) along the dissociative  $2p\sigma_u$  potential energy curve. As we will now show, the difference [2 laser cycles for the two peaks at 1.2 and 1.5 eV in Fig. 2(d)] between the two evolution times allows us to obtain the dissociative kinetic energy  $E_d$  for the low-energy peaks.

One can see from Fig. 1 that there is nearly no variation in the  $2p\sigma_u$  potential energy curve when  $R > 8$ . Thus the dissociative kinetic energies of the low-energy protons are

almost the same in spite of different numbers of laser cycles and ionization from different internuclear separations larger than 8. We can therefore estimate the dissociation energies in the following way. We consider two equations  $E_d + 1/R_{21} = 1.2$  eV and  $E_d + 1/R_{15} = 1.5$  eV, with  $R_{21}$  and  $R_{15}$  denoting the positions where the second ionization takes place when interacting with laser pulses with 21 and 15 laser cycles, respectively. In combination with the use of the relations  $E_d = \frac{1}{2}mv^2$  and  $vt = R_{21} - R_{15}$ , valid at  $R > 8$ , we obtain the dissociative kinetic energies along the  $2p\sigma_u$  potential energy curve from both the positions of the one- and three-photon resonances between the  $2p\sigma_u$  and  $1s\sigma_g$  curves. In these equations,  $v$  is the velocity corresponding to  $E_d$ ,  $m$  here is the reduced mass of the nuclei, and  $t$  is the evolution time difference for the 1.5 and 1.2 eV peaks. By substituting the evolution time difference of 2 laser cycles into the above equations, two physical solutions of the dissociative kinetic energy are obtained. One is 0.12 eV corresponding to the dissociative kinetic energy via the one-photon resonance. The other is 0.47 eV which corresponds to the dissociative kinetic energy after the three-photon resonance. Thus the potential energies at the one- and three-photon resonances can be expected as  $-13.6 + 0.12 = -13.48$  eV and  $-13.6 + 0.47 = -13.13$  eV, where  $-13.6$  eV is the energy of the dissociation limit. Both the energies obtained are quite close to the energies in the  $2p\sigma_u$  curve of  $-13.46$  and  $-13.24$  eV at the one- and three-photon resonances as listed in Table I. In a similar way, we can obtain the potential energies of the  $2p\sigma_u$  curve at the one- and three-photon resonances between the  $2p\sigma_u$  and  $1s\sigma_g$  curves for 3200 nm.

A detailed analysis of the KER spectra in Fig. 2 is conducted in the following with reference to Table I. The four processes shown in Fig. 4 are expected to play an important role for the final nuclear KER spectra. They represent enhanced ionization at the two CREI positions after the one- and three-photon resonant dipole coupling between the  $1s\sigma_g$  and the  $2p\sigma_u$  states in  $\text{H}_2^+$  at smaller internuclear distances. In principle, ionization at the one- and three-photon resonances should also result in peaks close to their Coulomb repulsion energies since the dissociative kinetic energy is much smaller for these two cases. To better understand the origin of the peaks in Fig. 2, the positions of the one-photon resonance,  $R_1$ , and the three-photon resonance,  $R_3$ , are given in Table I for several wavelengths. In addition, the potential energies in the  $2p\sigma_u$  potential energy curve ( $E_{u1}$  and  $E_{u3}$ ) and in the Coulomb potential energy curve for  $\text{H}_2^{++}$  at  $R_1$  and  $R_3$  are given.

When the wavelength is 800 nm, as expected from Table I, there should be some enhancement in the proton yields at around 8.3, 5.7, 6.6, 5.36, 4.63, and 3.4 eV. They result from enhanced ionization at the three-photon resonance and the one-photon resonance as well as from the four processes pictured in Fig. 4. In Fig. 2(a), the peaks around 4.7 eV mainly come from enhanced ionization at the CREI position of  $R = 7$  via the one-photon resonance, which can be verified by the following process: The dissociative kinetic energy is  $13.43 - 12.69 = 0.74$  eV, which is the difference in the  $2p\sigma_u$  potential energy curve between  $R_3 = 3.28$  and  $R = 7$ . Adding this kinetic energy to the Coulomb repulsion energy  $1/7$  (3.89 eV) at  $R = 7$ , the total kinetic energy of the proton is 4.63 eV. Similarly, the peaks around 5.3 eV in Fig. 2(a) can be

TABLE I. Data used for the analysis of the nuclear KER spectra following dissociative double ionization of  $H_2$ . The 750 nm case will be considered in Sec. IV. Here  $\omega$  denotes the laser angular frequency.  $R_1$  and  $R_3$  are the positions of the one- and three-photon resonances between the  $2p\sigma_u$  and  $1s\sigma_g$  curves in  $H_2^+$ , respectively.  $E_{u1}$  and  $E_{u3}$  are the corresponding potential energies in the  $2p\sigma_u$  potential energy curve at  $R_1$  and  $R_3$ .  $a_0$  is the Bohr radius.

| $\lambda$ (nm) | $h\omega$ (eV) | $R_1(a_0)$ | $R_3(a_0)$ | $E_{u1}$ (eV) | $E_{u3}$ (eV) | $1/R_1$ (eV) | $1/R_3$ (eV) |
|----------------|----------------|------------|------------|---------------|---------------|--------------|--------------|
| 800            | 1.55           | 4.74       | 3.28       | -12.69        | -10.7         | 5.7          | 8.3          |
| 1600           | 0.775          | 5.64       | 4.22       | -13.14        | -12.23        | 4.8          | 6.4          |
| 3200           | 0.388          | 6.5        | 5.12       | -13.35        | -12.91        | 4.2          | 5.3          |
| 6400           | 0.194          | 7.32       | 6          | -13.46        | -13.24        | 3.7          | 4.5          |
| 750            | 1.653          | 4.67       | 3.19       | -12.63        | -10.47        | 5.82         | 8.53         |

related to enhanced ionization at the CREI position of  $R = 11$  via the three-photon resonance, which are quite close to the expected  $2.89 + 2.47 = 5.36$  eV. The peaks around 7.3 eV are indeed from the combined contributions from at least two processes. These are enhanced ionization at the three-photon resonance (8.3 eV) and at the CREI position of  $R = 7$  via the three-photon resonance (6.6 eV). These two relative broad peaks may give a peak at around  $(8.3 + 6.6) / 2 = 7.45$  eV. The peaks around 6.2 eV are mainly from the combination of enhanced ionization at the one-photon resonance (5.7 eV) and at the CREI position of  $R = 7$  via the three-photon resonance (6.6 eV).

When the wavelength is 1600 nm, Table I and reasoning as in the 800 nm case above shows that enhancements around 6.4, 4.8, 4.2, 3.0, 5.1, and 3.9 eV are expected to appear in the spectra shown in Fig. 2(b). As a result, the peaks around 6.4 eV mainly come from enhanced ionization via the three-photon resonance. The peaks around 5 eV are mainly from enhanced ionization via the one-photon resonance and enhanced ionization at  $R = 7$  after the three-photon resonance. The peaks around 4.3 eV are mainly from enhanced ionization

at the CREI position of  $R = 7$  and enhanced ionization at  $R = 11$  via the three-photon resonance. Besides, large ionization at the CREI position of  $R = 11$  through the one-photon resonance leads to the peaks around 3 eV.

As the wavelength increases to 3200 nm, the expected enhancements in the spectra are around 5.3, 4.2, 4.0, 2.8, 4.4, and 3.2 eV, respectively (Table I). The ionization at the three-photon resonance can result in peaks around 5.3 eV. The peaks around 4.0 eV mainly come from large ionization at the one-photon resonance or at the CREI position of  $R = 7$  via the one-photon resonance or even from enhanced ionization at  $R = 7$  after the three-photon resonance. The peaks around 2.6 eV come from large ionization at the CREI position of  $R = 11$  after the one-photon resonance, while the peaks around 3 eV are from enhanced ionization at  $R = 11$  after the three-photon resonance. Further increasing the wavelength to 6400 nm, there should be enhancement in the proton yields around five kinetic energies [4.5, 3.7, 2.6, 4.1, and 2.9 eV (Table I)]. There would be no events at  $R = 7$  after the one-photon resonance, because the position of the one-photon resonance  $R = 7.32$  is larger than  $R = 7$ . The one-photon and three-photon resonances give peaks around 3.6 and 4.9 eV. Enhanced ionization at the CREI position of  $R = 11$  from the one- and three-photon resonances gives the respective peaks around 2.6 and 2.9 eV.

All of the plots in Figs. 2(a)–2(d) are renormalized to better observe the common features in the spectra. There are large differences in the proton yields for the pulses. In Fig. 2(e), the total yields of protons as a function of the number of laser cycles under several wavelengths are shown in units of ionization probability per molecule, which are also the units for the nuclear KER spectra below. When the peak intensity of the laser pulse is fixed, the duration of the pulse does influence the total yields. The larger the duration, the larger the yield. Besides, for the same durations, e.g., 10 laser cycles at 1600 nm and 5 laser cycles at 3200, the yields are nearly identical.

#### IV. DELAY DEPENDENCE OF KER SPECTRA FOR $H_2$ INTERACTING WITH TWO PULSES

When molecules interact with two or more laser pulses, dynamics of the nuclei as well as dynamics of the photoelectrons can be studied as a function of the time delay between the pulses. Usually, the first pulse is the pump which stimulates electronic excitation and nuclear motion. The following pulse acts as the probe and is used to detect the nuclear or electronic wave packets. The pump-probe technique has been widely

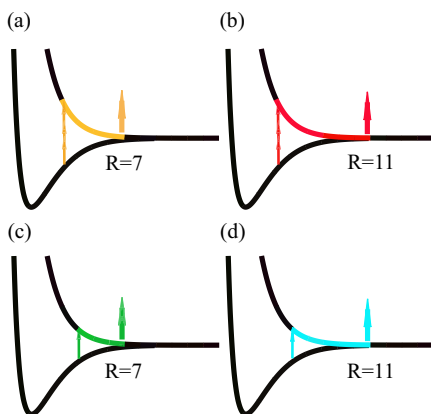


FIG. 4. Sketch of four processes of enhanced ionization at the two CREI positions of  $R = 7$  and  $R = 11$  (denoted by the outermost right arrows in the figures) after one- and three-photon resonance. (a) and (b) CREI at  $R = 7$  and  $R = 11$  after the three-photon resonance. (c) and (d) CREI at  $R = 7$  and  $R = 11$  after the one-photon resonance.



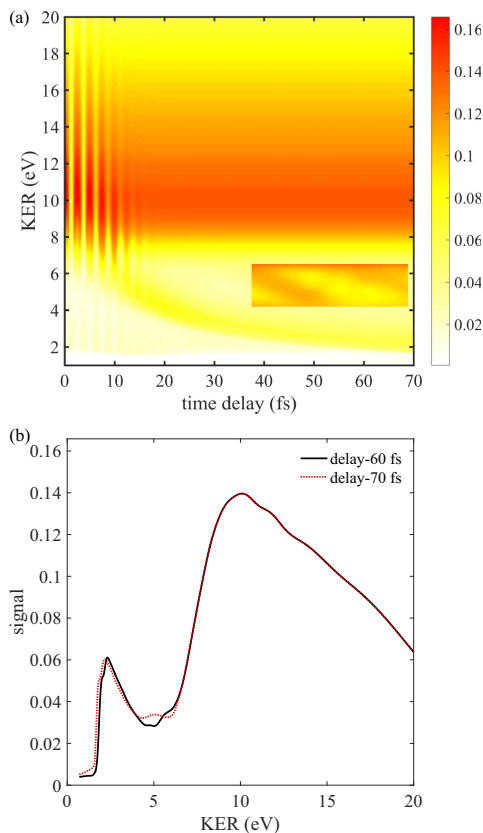


FIG. 5. (a) Nuclear KER distributions as a function of time delay between pump and probe pulses. The peak intensity of the pump (probe) pulse is  $4 \times 10^{14}$  W/cm $^2$  ( $6 \times 10^{13}$  W/cm $^2$ ). The two pulses have the same wavelength (750 nm) and the same duration (3 laser cycles). The data are plotted to the power of 0.2 in order to gain a larger visibility of the structures and after that the signal in the insert was multiplied by a factor of 3. (b) Cuts from (a) before multiplying by a factor 3 at time delays of 60 and 70 fs.

used to study ultrafast dynamics of both electrons and nuclei and we refer the readers to Refs. [11,29,44,46–48] for recent examples in H $_2$ . In Fig. 5(a), we plot the simulated KER distributions as a function of time delay between pump and probe laser pulses with their polarization axes parallel to the molecular axis. To test the performance of our approach, the parameters of the two laser pulses are chosen according to Ref. [48]: The central wavelength and the FWHM duration of the two pulses are 750 nm and 3 laser cycles, respectively. The pump laser has a peak intensity of  $4 \times 10^{14}$  W/cm $^2$  while the probe has a peak intensity of  $6 \times 10^{13}$  W/cm $^2$ . We find a good agreement between Fig. 5(a) and the experimental results of Ref. [48]. In particular, the high-energy branch around 10 eV

and the energy-decreasing branch from 6 to 2 eV for increasing time delay are reproduced.

In Fig. 5(a), the channel with KER around 10 eV mainly comes from double ionization of H $_2$  by the more intense pump pulse. This channel shows no delay dependence when the delay is larger than 20 fs. However, for delays smaller than 20 fs, oscillation of the KER distributions with a period of one laser cycle is observed. This oscillation is a signature of constructive and destructive interference between the two pulses when the two pulses overlap in time. The channel with KER in the 2–6 eV range has a strong delay dependence and is due to the ionization of H $_2^+$  by the relatively weak probe pulse. The main energy-decreasing branch from 6 to 2 eV for increasing delay is a result of the nuclear wave packet moving along the  $2p\sigma_u$  potential energy curve in H $_2^+$ .

In addition, there are two much weaker energy-decreasing branches. A zoom of part of the branches is shown in the insert to the right of Fig. 5(a). These branches can be shown to result from the oscillatory movement of the nuclear wave packet along the  $1s\sigma_g$  potential energy curve in H $_2^+$ : The duration between the first dominant decreasing branch starting at a time delay around 15 fs and the second branch highlighted in the insert is around 20–25 fs corresponding to a full oscillatory motion in the  $1s\sigma_g$  curve.

To extract properties of the  $2p\sigma_u$  potential energy curve, we resort to solving the equations of the dissociative kinetic energy as discussed in Sec. III. We use the peak positions of 2.17 and 2.34 eV for the two low-energy peaks at time delays of 60 and 70 fs [Fig. 5(b)]. With this difference in evolution time of 10 fs, we obtain the dissociative kinetic energy of about 0.93 eV. Thus the  $2p\sigma_u$  potential energy at the one-photon resonance position for 750 nm is about  $-13.6 + 0.93 = -12.67$  eV, which is very close to the expectation of  $-12.63$  eV from Table. I.

As the wavelength of the laser pulses becomes larger, more structures in the KER spectra are expected, since the larger laser duration can activate more ionization pathways. In Fig. 6(a), we plot the KER distributions as a function of delay, when the wavelengths of both pulses are 1600 nm while the other parameters are as in Fig. 5. Processes similar to the ones in Fig. 5(a) can be seen in Fig. 6(a), for example, interference between the two pulses at time delays shorter than 30 fs and movement of the nuclear wave packet along the  $2p\sigma_u$  potential energy curve (branch decreasing from 5 eV). Three peaks around 10 eV are observed. The origin of these peaks is discussed below. As shown in Fig. 6(b), when the delay is 140 fs, the low-energy peak of the KER spectra is around 1.2 eV, and when the delay is 80 fs, the low-energy peak of the KER spectra is around 1.75 eV. By solving similar equations as in Sec. III, we obtain a dissociative kinetic energy of 0.42 eV, which is used to obtain the potential energy along the  $2p\sigma_u$  curve at the one-photon resonance position for 1600 nm. The result of  $-13.6 + 0.42 = -13.18$  eV is in very good agreement with the energy of  $-13.14$  eV from Table. I.

A trajectory analysis can help to clearly identify how the peaks in Fig. 6(b) are formed. In Fig. 7, contributions from different trajectories to the four peaks (8.5, 9.8, 13, and 1.4 eV) in the KER spectra when the delay is 122 fs in Fig. 6(b) are shown. As in Fig. 3, a periodical dependence of the signal with the second jump time  $T_2$  is clearly seen. The three peaks around 8.5, 9.8, and 13 eV are mainly from double ionization

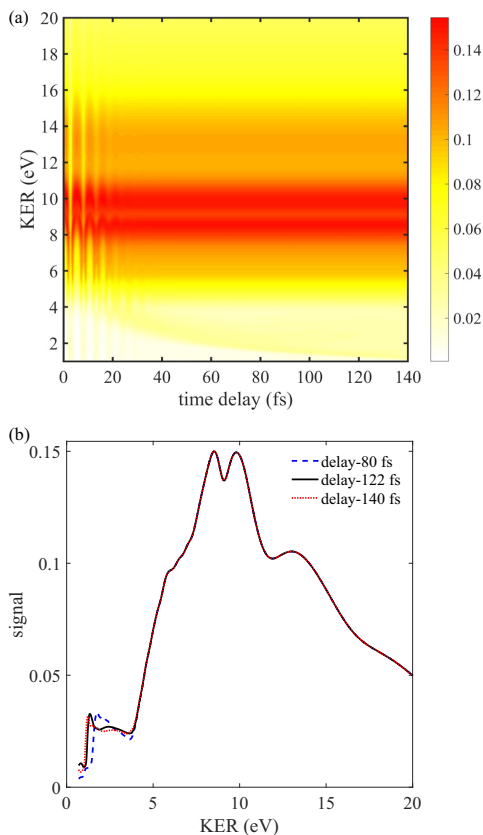


FIG. 6. (a) Nuclear KER distributions as a function of time delay between pump and probe pulses. The peak intensity of the pump (probe) pulse is  $4 \times 10^{14}$  W/cm<sup>2</sup> ( $6 \times 10^{13}$  W/cm<sup>2</sup>). Both the wavelengths are 1600 nm and the duration of both pulses is 3 laser cycles. The data are plotted to the power of 0.2 in order to gain a larger visibility of the structures. (b) Cuts from (a) at time delays of 80, 122, and 140 fs.

induced by the pump pulse alone: The signals around 13 eV mainly come from trajectories in which the evolution time in H<sub>2</sub><sup>+</sup> (difference between the first and second jump times) is about half a laser cycle; the signals around 9.8 eV are from trajectories where the evolution time is around one laser cycle; and the signals around 8.5 eV are from trajectories where the evolution time is about one and a half laser cycles. The low-energy peak around 1.4 eV is from trajectories where the first ionization is induced by the pump pulse and the second by the probe pulse. In this manner, as was the case in Sec. III, the MCWP approach offers a very direct look into the time scale of the ionization dynamics associated with a given feature in the KER spectra. In Fig. 7, we also notice that the first jumps mainly occur at the same time around 750 (18.3 fs) for the three

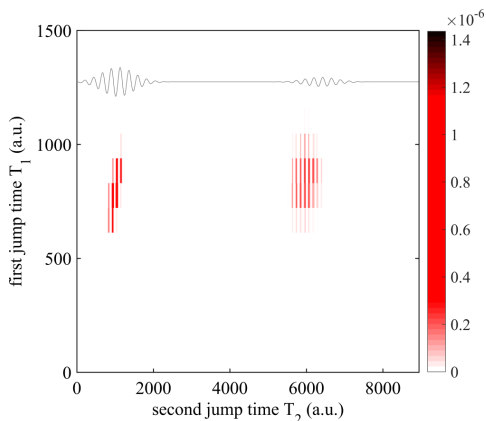


FIG. 7. Contributions from different trajectories to the four peaks (8.5, 9.8, 13, and 1.4 eV) in the KER spectra in Fig. 6(b) when the delay is 122 fs. The distributions in the small  $T_2 \sim 1000$  range result in three high-energy peaks around 8.5, 9.8, and 13 eV while the distributions in the large  $T_2 \sim 6000$  range give the low-energy peak around 1.4 eV. The two pulses are also shown by the grey line in the top of the figure. To show the distributions clearly in a single figure, signals for  $T_2 \sim 6000$  have been multiplied by a factor of 5000.

high-energy peaks. The pump field is so strong that nearly all of the singly ionized molecules would be further ionized in two laser cycles.

The evolution of the wave packet could be quite different when the wavelengths of the two pulses are different. In Fig. 8,

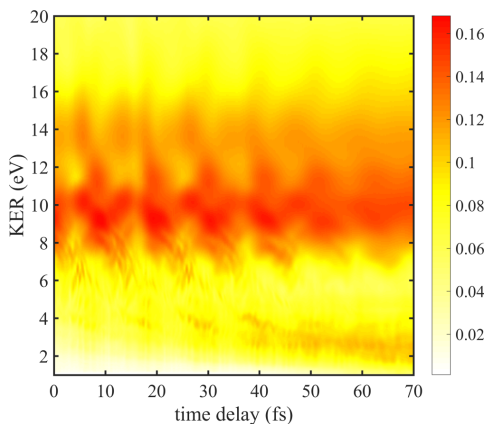


FIG. 8. Nuclear KER distributions as a function of time delay between the pump and probe pulses. The peak intensity of the pump (probe) pulse is  $4 \times 10^{14}$  W/cm<sup>2</sup> ( $6 \times 10^{13}$  W/cm<sup>2</sup>). The pump (probe) wavelength is 800 nm (6400 nm). The duration of both pulses is 3 laser cycles. The data are plotted to the power of 0.2 in order to gain a larger visibility of the structures.

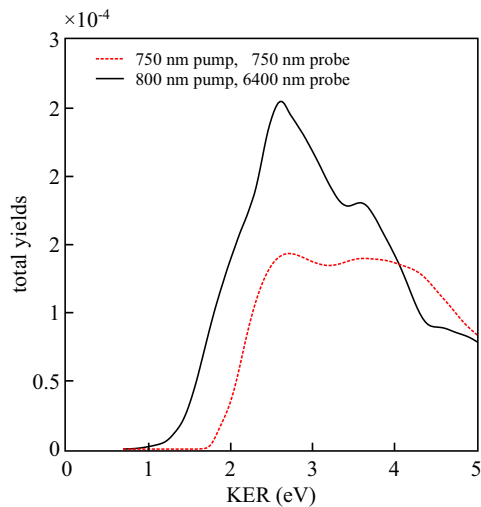


FIG. 9. Total KER spectra integrated over all delays and shown as a function of KER energy. The red dashed line is for Fig. 5 and the black solid line for Fig. 8, respectively.

the nuclear KER spectra of  $H_2$  interacting with two pulses with different wavelengths are shown. The central wavelength of the pump pulse is 800 nm and that of the probe pulse is 6400 nm. They both contain three laser cycles. Because the probe pulse is much longer, there are more structures and more yields in the KER spectra mainly induced by the probe pulse. Even when the delay reaches almost 70 fs, the overlap between the two pulses still plays a role in the final KER spectra, as is seen from the delay dependence of the 10 eV channel. Moreover, there are more structures around the large kinetic energy channel at small delays because the effective duration of the pump pulse is becoming larger. Because of the complicated structures in the energy-decreasing branch (from 5 to 2 eV) in Fig. 8, the low-energy peaks in this case are not used to obtain the dissociative kinetic energy after the one-photon resonance.

The pronounced energy-decreasing branch in Fig. 8 is, however, useful for extracting information about CREI. The total KER spectra integrated over all delays in Figs. 5 and 8 are shown in Fig. 9, which shows a clear signature of the presence of the enhanced ionization. For both cases, the peaks around 3.6 eV mainly come from ionization at the CREI position of  $R = 11$  after the one-photon resonance between the  $2p\sigma_u$  and  $1s\sigma_g$  curves in  $H_2^+$ , while the energy-decreasing branch around 2.6 eV for delays larger than  $\sim 40$  fs represents nuclear KER spectra resulting from ionization from  $R > 11$ . In theory, there should be peaks around 4.6 eV because of large ionization around the other CREI position at  $R = 7$  after the one-photon resonance between the  $2p\sigma_u$  and  $1s\sigma_g$  curves in  $H_2^+$ . However, they are not as clear as the peaks around 3.6 eV. A possible cause is that the enhanced ionization at around  $R = 7$  results in

a broader energy peak than that at around  $R = 11$  because there is a larger relative change in the Coulomb repulsion energy at smaller internuclear distances than at larger internuclear distances for a given  $\Delta R$ .

The above discussion shows how the wavelength, pulse duration, as well as delay of the laser pulses determine the nuclear KER spectra. The dynamics of the nuclear wave packets can be extracted when these parameters are well chosen. The ionization induced by the probe pulse after the one-photon resonance resulting from the pump pulse largely contributes to the energy-decreasing branch of the KER spectra. This delay-dependent channel will be more pronounced if the duration or the intensity of the probe pulse is increased. Meanwhile, when increasing the duration of the laser pulses, CREI would also show up more clearly on the averaged spectra integrated over all delays.

## V. SUMMARY AND CONCLUSION

We calculated the nuclear KER spectra of  $H_2$  interacting with laser pulses with central wavelengths ranging from the near-IR regime to the mid-IR regime. With increasing wavelength, we observe a shift in the nuclear kinetic energy distribution toward lower energies. A detailed analysis of the peaks in the KER spectra was carried out. Some of the peaks are from ionization taking place at the one- or three-photon resonance between the  $1s\sigma_g$  and  $2p\sigma_u$  curves in the  $H_2^+$  system. Others are from CREI after the one- and three-photon resonances, or from a combination of these processes. Both for the cases of a single laser pulse and for two time-delayed pulses, characteristic low-energy peaks were observed when the duration or the delay of the pulses is large, e.g., for a single pulse with 21 laser cycles at 6400 nm and for two pump-probe pulses at 1600 nm with delay of 122 fs. The main physical origin of the low-energy peaks is ionization occurring at instants of field extrema when the nuclear wave packet has reached separations beyond the CREI position of  $R = 11$ . For the single-pulse case, the low-energy peak is a result of ionization after dissociation via the one- and three-photon resonances between the  $1s\sigma_g$  and  $2p\sigma_u$  states. For the two pulse case, it mainly originates from ionization following dissociation via the one-photon resonance between the two states. In the pump-probe simulation, by integrating the KER spectra with all delays, the effect of CREI was shown in the KER spectra. We also showed how to extract the dissociative energies of the  $2p\sigma_u$  curve in  $H_2^+$  following excitation at the one- or three-photon resonances at 750, 1600, and 6400 nm. Finally, we illustrated in a few selected cases how the MCWP approach allows a trajectory analysis helping with the identification of dominant breakup pathways including an assessment of typical durations between the ionization events forming the characteristic features in the KER spectra.

## ACKNOWLEDGMENTS

We thank Lun Yue for help with numerical issues. The numerical results presented in this work were obtained at the Centre for Scientific Computing, Aarhus. This work was supported by the European Union Horizon 2020 research

and innovation program under the Marie Skłodowska-Curie Grant Agreement No. 641789 MEDEA (Molecular Electron Dynamics Investigated by Intense Fields and Attosecond

Pulses), the European Research Council StG (Project No. 277767-TDMET), and the VKR Center of Excellence, QUSCOPE.

- 
- [1] L. Zhu, V. Kleiman, X. Li, S. P. Lu *et al.*, Coherent laser control of the product distribution obtained in the photoexcitation of HI, *Science* **270**, 77 (1995).
- [2] A. H. Zewail, Femtochemistry: Atomic-scale dynamics of the chemical bond, *J. Phys. Chem. A* **104**, 5660 (2000).
- [3] I. V. Hertel and W. Radloff, Ultrafast dynamics in isolated molecules and molecular clusters, *Rep. Prog. Phys.* **69**, 1897 (2006).
- [4] D. Rapp, P. Englander-Golden, and D. D. Briglia, Cross sections for dissociative ionization of molecules by electron impact, *J. Chem. Phys.* **42**, 4081 (1965).
- [5] K. Codling and L. J. Frasinski, Dissociative ionization of small molecules in intense laser fields, *J. Phys. B: At., Mol. Opt. Phys.* **26**, 783 (1993).
- [6] S. Chelkowski, C. Foisy, and A. D. Bandrauk, Electron-nuclear dynamics of multiphoton  $H_2^+$  dissociative ionization in intense laser fields, *Phys. Rev. A* **57**, 1176 (1998).
- [7] J. H. Posthumus, The dynamics of small molecules in intense laser fields, *Rep. Prog. Phys.* **67**, 623 (2004).
- [8] L. Yue and L. B. Madsen, Dissociation and dissociative ionization of  $H_2^+$  using the time-dependent surface flux method, *Phys. Rev. A* **88**, 063420 (2013).
- [9] T. Jahnke, A. Czasch, M. S. Schöffler, S. Schössler, A. Knapp, M. Kász, J. Titze, C. Wimmer, K. Kreidi, R. E. Grisenti, A. Staudte, O. Jagutzki, U. Hergenbahn, H. Schmidt-Böcking, and R. Dörner, Experimental Observation of Interatomic Coulombic Decay in Neon Dimers, *Phys. Rev. Lett.* **93**, 163401 (2004).
- [10] L. Strüder, S. Epp, D. Rolles, R. Hartmann, P. Holl, G. Lutz, H. Soltau, R. Eckart, C. Reich, K. Heinzinger *et al.*, Large-format, high-speed, X-ray pnCCDs combined with electron and ion imaging spectrometers in a multipurpose chamber for experiments at 4th generation light sources, *Nucl. Instrum. Methods Phys. Res. A* **614**, 483 (2010).
- [11] U. Thumm, T. Niederhausen, and B. Feuerstein, Time-series analysis of vibrational nuclear wave-packet dynamics in  $D_2^+$ , *Phys. Rev. A* **77**, 063401 (2008).
- [12] A. D. Bandrauk and J. Ruel, Charge-resonance-enhanced ionization of molecular ions in intense laser pulses: Geometric and orientation effects, *Phys. Rev. A* **59**, 2153 (1999).
- [13] T. Zuo and A. D. Bandrauk, Charge-resonance-enhanced ionization of diatomic molecular ions by intense lasers, *Phys. Rev. A* **52**, R2511 (1995).
- [14] B. Yang, M. Saeed, L. F. DiMauro, A. Zavriyev, and P. H. Bucksbaum, High-resolution multiphoton ionization and dissociation of  $H_2$  and  $D_2$  molecules in intense laser fields, *Phys. Rev. A* **44**, R1458 (1991).
- [15] A. Apalategui and A. Saenz, Multiphoton ionization of the hydrogen molecule  $H_2$ , *J. Phys. B: At., Mol. Opt. Phys.* **35**, 1909 (2002).
- [16] S. Chelkowski, A. D. Bandrauk, A. Staudte, and P. B. Corkum, Dynamic nuclear interference structures in the Coulomb explosion spectra of a hydrogen molecule in intense laser fields: Reexamination of molecular enhanced ionization, *Phys. Rev. A* **76**, 013405 (2007).
- [17] J. Caillat, J. Zanghellini, M. Kitzler, O. Koch, W. Kreuzer, and A. Scrinzi, Correlated multielectron systems in strong laser fields: A multiconfiguration time-dependent Hartree-Fock approach, *Phys. Rev. A* **71**, 012712 (2005).
- [18] J. L. Sanz-Vicario, H. Bachau, and F. Martín, Time-dependent theoretical description of molecular autoionization produced by femtosecond XUV laser pulses, *Phys. Rev. A* **73**, 033410 (2006).
- [19] F. Calegari, D. Ayuso, A. Trabattoni, L. Belshaw, S. De Camillis, S. Anumula, F. Frassetto, L. Poletto, A. Palacios, P. Decleva, J. B. Greenwood, F. Martín, and M. Nisoli, Ultrafast electron dynamics in phenylalanine initiated by attosecond pulses, *Science* **346**, 336 (2014).
- [20] J. Dalibard, Y. Castin, and K. Mølmer, Wave-Function Approach to Dissipative Processes in Quantum Optics, *Phys. Rev. Lett.* **68**, 580 (1992).
- [21] H. A. Leth, L. B. Madsen, and K. Mølmer, Monte Carlo Wave Packet Theory of Dissociative Double Ionization, *Phys. Rev. Lett.* **103**, 183601 (2009).
- [22] H. A. Leth, L. B. Madsen, and K. Mølmer, Monte Carlo wave packet approach to dissociative multiple ionization in diatomic molecules, *Phys. Rev. A* **81**, 053409 (2010).
- [23] H. A. Leth, L. B. Madsen, and K. Mølmer, Dissociative double ionization of  $H_2$  and  $D_2$ : Comparison between experiment and Monte Carlo wave packet calculations, *Phys. Rev. A* **81**, 053410 (2010).
- [24] H. A. Leth and L. B. Madsen, Dissociative multiple ionization of diatomic molecules by extreme-ultraviolet free-electron-laser pulses, *Phys. Rev. A* **83**, 063415 (2011).
- [25] H.-P. Breuer, E.-M. Laine, J. Piilo, and B. Vacchini, Colloquium: Non-Markovian dynamics in open quantum systems, *Rev. Mod. Phys.* **88**, 021002 (2016).
- [26] M. Vafaee, H. Sabzyan, Z. Vafaee, and A. Katanforoush, Detailed instantaneous ionization rate of  $H_2^+$  in an intense laser field, *Phys. Rev. A* **74**, 043416 (2006).
- [27] G. L. Yudin and M. Y. Ivanov, Nonadiabatic tunnel ionization: Looking inside a laser cycle, *Phys. Rev. A* **64**, 013409 (2001).
- [28] E. Goll, G. Wunner, and A. Saenz, Formation of Ground-State Vibrational Wave Packets in Intense Ultrashort Laser Pulses, *Phys. Rev. Lett.* **97**, 103003 (2006).
- [29] T. Ergler, B. Feuerstein, A. Rudenko, K. Zrost, C. D. Schröter, R. Moshhammer, and J. Ullrich, Quantum-Phase Resolved Mapping of Ground-State Vibrational  $D_2$  Wave Packets via Selective Depletion in Intense Laser Pulses, *Phys. Rev. Lett.* **97**, 103004 (2006).
- [30] J. Förster, E. Plésiat, A. Magaña, and A. Saenz, Imaging of the umbrella motion and tunneling in ammonia molecules by strong-field ionization, *Phys. Rev. A* **94**, 043405 (2016).
- [31] B. Wolter, M. G. Pullen, M. Baudisch, M. Sclafani, M. Hemmer, A. Senftleben, C. D. Schröter, J. Ullrich, R. Moshhammer, and J. Biegert, Strong-Field Physics with Mid-IR Fields, *Phys. Rev. X* **5**, 021034 (2015).

- [32] C. I. Blaga, J. Xu, A. D. DiChiara, E. Sistrunk, K. Zhang, P. Agostini, T. A. Miller, L. F. DiMauro, and C. D. Lin, Imaging ultrafast molecular dynamics with laser-induced electron diffraction, *Nature* **483**, 194 (2012).
- [33] M. Meckel, D. Comtois, D. Zeidler, A. Staudte, D. Pavičić, H. C. Bandulet, H. Pépin, J. C. Kieffer, R. Dörner, D. M. Villeneuve, and P. B. Corkum, Laser-induced electron tunneling and diffraction, *Science* **320**, 1478 (2008).
- [34] T. Popmintchev, M.-C. Chen, D. Popmintchev, P. Arpin, S. Brown, S. Ališauskas, G. Andriukaitis, T. Balčiunas, O. D. Mücke, A. Pugzlys, A. Baltuška, B. Shim, S. E. Schrauth, A. Gaeta, C. Hernández-García, L. Plaja, A. Becker, A. Jaron-Becker, M. M. Murnane, and H. C. Kapteyn, Bright coherent ultrahigh harmonics in the keV X-ray regime from mid-infrared femtosecond lasers, *Science* **336**, 1287 (2012).
- [35] X.-M. Tong, Z. X. Zhao, and C.-D. Lin, Theory of molecular tunneling ionization, *Phys. Rev. A* **66**, 033402 (2002).
- [36] X. Urbain, B. Fabre, E. M. Staiçu-Casagrande, N. de Ruette, V. M. Andrianarijaona, J. Jureta, J. H. Posthumus, A. Saenz, E. Baldit, and C. Cornaggia, Intense-Laser-Field Ionization of Molecular Hydrogen in the Tunneling Regime and its Effect on the Vibrational Excitation of  $H_2^+$ , *Phys. Rev. Lett.* **92**, 163004 (2004).
- [37] O. I. Tolstikhin, T. Morishita, and L. B. Madsen, Theory of tunneling ionization of molecules: Weak-field asymptotics including dipole effects, *Phys. Rev. A* **84**, 053423 (2011).
- [38] J. Svensmark, O. I. Tolstikhin, and L. B. Madsen, Theory of dissociative tunneling ionization, *Phys. Rev. A* **93**, 053426 (2016).
- [39] P. J. Lindstrom and W. G. Mallard, NIST Chemistry Webbook, NIST Standard Reference 69, June 2005, National Institute of Standards and Technology, Gaithersburg MD, <http://webbook.nist.gov>.
- [40] H. A. Leth, Dissociative ionization. A study using the Monte Carlo wave packet approach, Ph.D. dissertation, Aarhus University, 2011.
- [41] M. Plummer and J. F. McCann, Field-ionization rates of the hydrogen molecular ion, *J. Phys. B: At., Mol. Opt. Phys.* **29**, 4625 (1996).
- [42] M. Feit, J. Fleck, and A. Steiger, Solution of the Schrödinger equation by a spectral method, *J. Comput. Phys.* **47**, 412 (1982).
- [43] J. T. Lin and T. F. Jiang, Photodissociation of  $H_2^+$  in intense chirped laser fields, *Phys. Rev. A* **63**, 013408 (2000).
- [44] A. Staudte, D. Pavičić, S. Chelkowski, D. Zeidler, M. Meckel, H. Niikura, M. Schöffler, S. Schössler, B. Ulrich, P. P. Rajeev, T. Weber, T. Jahnke, D. M. Villeneuve, A. D. Bandrauk, C. L. Cocke, P. B. Corkum, and R. Dörner, Attosecond Stroboscopic Two-Surface Population Dynamics in Dissociating  $H_2^+$ , *Phys. Rev. Lett.* **98**, 073003 (2007).
- [45] H. Niikura, D. M. Villeneuve, and P. B. Corkum, Controlling vibrational wave packets with intense, few-cycle laser pulses, *Phys. Rev. A* **73**, 021402(R) (2006).
- [46] I. A. Bocharova, H. Mashiko, M. Magrakvelidze, D. Ray, P. Ranitovic, C. L. Cocke, and I. V. Litvinyuk, Direct Coulomb-explosion imaging of coherent nuclear dynamics induced by few-cycle laser pulses in light and heavy hydrogen, *Phys. Rev. A* **77**, 053407 (2008).
- [47] A. S. Alnaser, X. M. Tong, T. Osipov, S. Voss, C. M. Maharjan, P. Ranitovic, B. Ulrich, B. Shan, Z. Chang, C. D. Lin, and C. L. Cocke, Routes to Control of  $H_2$  Coulomb Explosion in Few-Cycle Laser Pulses, *Phys. Rev. Lett.* **93**, 183202 (2004).
- [48] H. Xu, F. He, D. Kielpinski, R. T. Sang, and I. V. Litvinyuk, Experimental observation of the elusive double-peak structure in R-dependent strong-field ionization rate of  $H_2^+$ , *Sci. Rep.* **5**, 13527 (2015).

---

# My Second Paper

Paper II. PHYSICAL REVIEW A 97, 043426 (2018)

*Title:*

**Monte Carlo wave-packet approach to trace nuclear dynamics in molecular excited states by XUV-pump–IR-probe spectroscopy**

*Authors: Qingli Jing, Roger Y. Bello, Fernando Martín, Alicia Palacios, and Lars Bojer Madsen*

DOI: <https://doi.org/10.1103/PhysRevA.97.043426>

My contribution to this publication: (1) implementation of the theoretical calculations and (2) preparation of the manuscript (with figures).

## Monte Carlo wave-packet approach to trace nuclear dynamics in molecular excited states by XUV-pump–IR-probe spectroscopy

Qingli Jing,<sup>1</sup> Roger Y. Bello,<sup>2</sup> Fernando Martín,<sup>2,3,4</sup> Alicia Palacios,<sup>2,5</sup> and Lars Bojer Madsen<sup>1</sup>


<sup>1</sup>*Department of Physics and Astronomy, Aarhus University, 8000 Aarhus C, Denmark*

<sup>2</sup>*Departamento de Química, Universidad Autónoma de Madrid, 28049 Madrid, Spain*

<sup>3</sup>*Instituto Madrileño de Estudios Avanzados en Nanociencia, Cantoblanco, 28049 Madrid, Spain*

<sup>4</sup>*Condensed Matter Physics Center, UAM, 28049 Madrid, Spain*

<sup>5</sup>*Institute for Advanced Research in Chemical Sciences, Universidad Autónoma de Madrid, 28049 Madrid, Spain*

 (Received 13 December 2017; revised manuscript received 26 March 2018; published 25 April 2018)

Recent research interests have been raised in uncovering and controlling ultrafast dynamics in excited neutral molecules. In this work we generalize the Monte Carlo wave packet (MCWP) approach to XUV-pump–IR-probe schemes to simulate the process of dissociative double ionization of H<sub>2</sub> where singly excited states in H<sub>2</sub> are involved. The XUV pulse is chosen to resonantly excite the initial ground state of H<sub>2</sub> to the lowest excited electronic state of <sup>1</sup>Σ<sub>u</sub><sup>+</sup> symmetry in H<sub>2</sub> within the Franck-Condon region. The delayed intense IR pulse couples the excited states of <sup>1</sup>Σ<sub>u</sub><sup>+</sup> symmetry with the nearby excited states of <sup>1</sup>Σ<sub>g</sub><sup>+</sup> symmetry. It also induces the first ionization from H<sub>2</sub> to H<sub>2</sub><sup>+</sup> and the second ionization from H<sub>2</sub><sup>+</sup> to H<sup>+</sup> + H<sup>+</sup>. To reduce the computational costs in the MCWP approach, a sampling method is proposed to determine in time the dominant ionization events from H<sub>2</sub> to H<sub>2</sub><sup>+</sup>. By conducting a trajectory analysis, which is a unique possibility within the MCWP approach, the origins of the characteristic features in the nuclear kinetic energy release spectra are identified for delays ranging from 0 to 140 fs and the nuclear dynamics in the singly excited states in H<sub>2</sub> is mapped out.

DOI: [10.1103/PhysRevA.97.043426](https://doi.org/10.1103/PhysRevA.97.043426)

### I. INTRODUCTION

For molecular systems, due to interactions between nuclei and electrons, the electronic dynamics directly induced by the applied laser pulses is usually accompanied by nuclear dynamics. For example, dissociation of molecules can be induced by electronic excitation or ionization [1,2]. Many pioneering works have exploited ultrashort laser pulses to reveal and control the breakup dynamics including ionization and dissociation dynamics in molecules, where the applied laser pulses can be either single laser pulses or two laser pulses in a pump-probe configuration. For instance, 40-fs laser pulses with wavelengths tunable from 800 to 1850 nm were employed to probe the nuclear dynamics in H<sub>2</sub><sup>+</sup> by recollision excitation after tunneling ionization from H<sub>2</sub> [3,4]. Under the same recollision excitation mechanism, carrier-envelope stabilized few-cycle near-IR laser pulses were exploited to achieve electron localization, which is a crucial precondition in realizing control of chemical reaction dynamics, in molecular dissociation of H<sub>2</sub><sup>+</sup> [5]. More efficient control over electron localization in the same system was later realized in several dissociation channels involving recollision excitation and bond-softening mechanisms by using few-cycle [6] or 50-fs two-color [7] mid-IR laser pulses. In addition, by using IR laser pulses with varying

wavelengths, intensities, or pulse durations [8–10], nuclear dynamics in H<sub>2</sub><sup>+</sup> were resolved by studying the nuclear kinetic energy release (KER) spectra following double ionization, i.e., full breakup of H<sub>2</sub> after removal of two electrons.

Pump-probe spectroscopy is powerful in uncovering and controlling ultrafast dynamics taking place in molecules, especially since the emergence of attosecond laser sources. In general, the pump pulse is used to initiate molecular dynamics and the probe pulse is used to take snapshots of the dynamics in real time as a function of the controlled delay. Recently, there has been a considerable amount of work devoted to revealing and controlling ultrafast dynamics in molecules by using XUV-pump–IR-probe spectroscopy. For instance, control over electron localization in dissociation of H<sub>2</sub><sup>+</sup> was achieved by changing the delay between an attosecond pulse train (APT) and a many-cycle IR laser pulse [11,12]. Instead of applying an APT, exploiting a single isolated attosecond pulse as the pump pulse was also able to realize control over electron localization in the same H<sub>2</sub> system [13]. Apart from controlling electron localization, this XUV-IR scenario is especially useful in monitoring the nuclear dynamics in molecular excited states. For example, this scenario was applied to characterize the singly excited molecular dynamics by using the ionization signal [14–16].

For most of the works in the XUV-IR scenario (e.g., Refs. [14–16]) only the single-ionization channel is open, which limits the information about the ultrafast dynamics obtained by the measurements. More information can be obtained if double- or multiple-ionization channels are open. For example, former studies of the double-ionization channel of H<sub>2</sub> due to interaction with intense IR laser pulses have

*Published by the American Physical Society under the terms of the Creative Commons Attribution 4.0 International license. Further distribution of this work must maintain attribution to the author(s) and the published article's title, journal citation, and DOI.*



illustrated that the purely repulsive character of the Coulomb potential can provide an unequivocal identification of the different dissociative ionization pathways [17]. Up to now, there have been few theoretical and experimental works applying the XUV-pump-IR-probe spectroscopy to study the dynamics involved during the double-ionization processes in molecules. For the theoretical part, the difficulty of treating molecular double ionization lies in solving the time-dependent Schrödinger equation (TDSE) to describe both nuclear and electronic dynamics in the presence of two fields and non-perturbative dynamics. Even for the simplest molecules, this task is beyond the capabilities of conventional computers due to the involvement of a huge number of continuum states in the process. As a result, it is very attractive to develop a theory that simplifies the computations while still being accurate. Moreover, ideally, such a theory should facilitate an identification of the main physical mechanisms. To this end, one can resort to the Monte Carlo wave packet (MCWP) approach, which, in the context of strong-field physics, was first presented by Leth *et al.* [10] for the description of nuclear motion in the presence of dissipative electron dynamics. Since then, this methodology has been validated in a number of cases. For example, a detailed account of the theoretical foundation of the MCWP approach and its limitations including its relation to the master equation of the Lindblad form for open quantum systems was presented in Ref. [18] (see also the original works connected to quantum optics problems [19–21]). Later, a very detailed comparison with experimental nuclear KER spectra following interaction with near-infrared pulses was carried out for different wavelengths including pump-probe schemes [22]. The agreement between experiment and theory was excellent. Apart from reproducing experimental results for near infrared wavelengths, this approach was also capable of performing an accurate description of the dissociative multiple-ionization process in the XUV regime [23].

In this work we resolve nuclear dynamics in the singly excited states in  $H_2$  by generalizing the MCWP approach to simulate double ionization of  $H_2$  within XUV-pump-IR-probe schemes. The process of double ionization considered in this work is as follows (Fig. 1). Starting from the ground state of  $H_2$ , i.e., from the  $X^1\Sigma_g^+(v=0)$  state, the nuclear wave packets in the excited electronic states of  $^1\Sigma_u^+$  symmetry are first efficiently launched via a one-photon absorption process caused by the interaction with an ultrashort attosecond XUV pulse. Then a delayed intense femtosecond IR laser pulse strongly couples these excited states of  $^1\Sigma_u^+$  symmetry to the nearby excited states of  $^1\Sigma_g^+$  symmetry. Thus, there are nuclear wave packets evolving along the potential energy curves for the excited states of both  $^1\Sigma_g^+$  and  $^1\Sigma_u^+$  symmetries (Fig. 1). At the same time, substantial ionization from  $H_2$  to  $H_2^+$ , induced by the intense IR laser pulse, occurs from these excited states due to their small ionization potentials. After the first ionization, the remaining part of the IR laser pulse couples the electronic states in  $H_2^+$ , e.g., the  $1s\sigma_g$  and  $2p\sigma_u$  states, and simultaneously the second ionization from  $H_2^+$  to  $H^+ + H^+$  occurs. All these dynamics, including the ionization processes, are modeled by the present approach. Our theory treats the double ionization in a consistent theoretical framework for this attosecond pump-probe KER spectroscopy. By studying the nuclear KER spectra

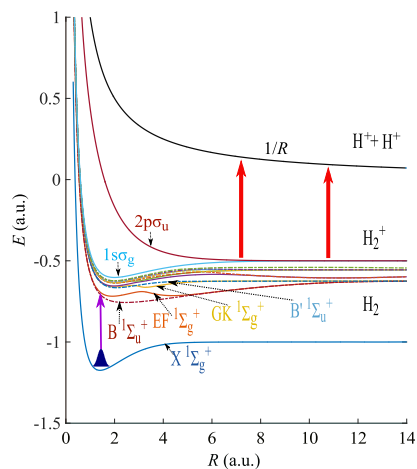


FIG. 1. Born-Oppenheimer potential energy curves as a function of the internuclear distance  $R$ . From the bottom to the top of the figure, the six lowest solid (dashed) curves represent the electronic potential energy curves for the six lowest electronic states of  $^1\Sigma_g^+$  ( $^1\Sigma_u^+$ ) symmetry in  $H_2$  below the  $^2\Sigma_g^+$  ( $1s\sigma_g$ ) curve in  $H_2^+$ . The two lowest potential energy curves in  $H_2^+$ , i.e., the  $1s\sigma_g$  and  $2p\sigma_u$  curves, and the  $1/R$  Coulombic curve of  $H^+ + H^+$  are also shown. The thin (purple) vertical arrow indicates the interaction between the XUV pump pulse and the ground-state molecule and the thick (red) arrows represent ionization from  $H_2^+$  to  $H^+ + H^+$  induced by the IR probe pulse. There is ionization from  $H_2$  to  $H_2^+$  induced by the IR field in spite of no arrow representing this process in the figure.

of the repulsive protons in the double-ionization channel for different pump-probe delays, the nuclear dynamics in the excited states of  $H_2$  can be mapped out. For example, characteristic features in the nuclear KER distribution as a function of the pump-probe delay are analyzed by conducting a trajectory analysis, where the trajectories that contribute the most to the observed features within our MCWP sampling are identified.

This work presents the consideration of utilizing the nuclear KER spectra following double ionization of the prototype  $H_2$  to recover the nuclear dynamics in the singly excited states by using XUV-pump-IR-probe spectroscopy. We hope our findings can stimulate the experimental studies in this scenario. This paper is organized as follows. In Sec. II we describe the application of the MCWP approach and its validation within XUV-pump-IR-probe schemes. In Sec. III the nuclear KER distributions following double ionization of  $H_2$  are obtained for three different pump-pulse durations. Through analyzing the characteristic features in the nuclear KER distributions, the nuclear dynamics in the excited states of  $H_2$  is retrieved. Section IV summarizes. A detailed description of the sampling method is reported in Appendix A and a discussion of nuclear wave packets in  $H_2^+$  from  $B3^1\Sigma_u^+$  is given in Appendix B. Atomic units are used unless otherwise stated.



## II. METHOD

### A. The MCWP approach

The MCWP approach has been thoroughly described in Refs. [10,18,22–26]. In this work we extend it to obtain the nuclear KER spectrum of the protons following double ionization of  $H_2$  in the two-color XUV-pump-IR-probe scheme where singly excited states in  $H_2$  are involved. When we use the MCWP approach to describe double ionization of  $H_2$ , three systems are involved, i.e., the neutral  $H_2$ ,  $H_2^+$ , and  $H_2^{2+}$ . For a specific system containing electrons, due to its interaction with the applied external field, ionization may occur which takes the specific system to the system with one electron less. Meanwhile, the electron removed from the system is now in the continuum states. The MCWP approach regards the integrated influence of the continuum states as the surroundings of a given system. Thus, the unidirectional loss of electrons from a given system to its surroundings can be treated by adding a non-Hermitian term to the system Hamiltonian. For a given system, the Hamiltonian is

$$H = H_s - \frac{i}{2} \sum_m C_m^\dagger C_m. \quad (1)$$

The equivalence of the constructed non-Hermitian Hamiltonian (1) to the Lindblad form master equation for an open system is shown in Ref. [18]. In Eq. (1),  $C_m$  is a jump operator, which specifies the transition from the electronic state  $|\phi_{R,m}^{\text{el}}\rangle$  in a given charge state to the electronic states  $|\phi_{R,n}^{\text{el}}\rangle$  in the system with one electron less [10,18], i.e.,

$$C_m = \sum_n \int d\vec{R} \sqrt{\Gamma_m(\vec{R},t)} M_n(\vec{R},t) |\phi_{R,n}^{\text{el}}\rangle \langle \phi_{R,m}^{\text{el}}| \otimes |\vec{R}\rangle \langle \vec{R}|, \quad (2)$$

where  $|\vec{R}\rangle$  is the position eigenket of the nuclear coordinate and  $\Gamma_m(\vec{R},t)$  is the ionization rate for the molecule when the electron (electrons) is (are) in the  $|\phi_{R,m}^{\text{el}}\rangle$  state. The term  $\sum_n M_n(\vec{R},t) |\phi_{R,n}^{\text{el}}\rangle$  in Eq. (2) represents the field-dressed ground state in the new charge state, which is a linear combination of the field-free electronic states  $|\phi_{R,n}^{\text{el}}\rangle$ . For example, following a quantum jump from  $H_2$ , the expression for  $M_n(\vec{R},t)$  in  $H_2^+$  can be found in Ref. [27]. The above-mentioned electronic states, which have a parametric dependence on the internuclear distance  $\vec{R}$ , can be obtained by solving the time-independent Schrödinger equation of the electronic Hamiltonian  $H_{\text{el}}$  at fixed  $\vec{R}$ , i.e.,  $H_{\text{el}} |\phi_{R,m}^{\text{el}}\rangle = E_m^{\text{el}}(\vec{R}) |\phi_{R,m}^{\text{el}}\rangle$ . Since the influence of the continuum states is integrated in the non-Hermitian term in Eq. (1), the electronic states involved in the jump operator in Eq. (2) are bound states. The electronic Hamiltonian  $H_{\text{el}}$  is related to the system Hamiltonian  $H_s$  through  $H_s = T_N + H_{\text{el}} + V_L(t)$ , where  $T_N$  is the nuclear kinetic energy operator and  $V_L(t) = -\vec{\mu} \cdot \vec{F}(t)$  is the light-molecule interaction operator. In this operator,  $\vec{\mu}$  is dipole operator of the electrons and  $\vec{F}(t) = \vec{F}_{\text{XUV}}(t) + \vec{F}_{\text{IR}}(t)$  is the combination of the electric fields of the applied pump and probe pulses. In this work, both pulses are linearly polarized parallel to the molecular axis. For the XUV pulse, its vector

potential is described by a  $\sin^2$  envelope, i.e.,

$$A_{\text{XUV}}(t) = A_{\text{XUV0}} \sin^2\left(\frac{\pi t}{T_{\text{XUV}}}\right) \sin(\omega_{\text{XUV}} t), \quad (3)$$

where  $T_{\text{XUV}}$  is the XUV pulse duration and  $\omega_{\text{XUV}}$  is the central frequency of the XUV pulse. The instantaneous field strength of the XUV pulse is obtained from the relation  $F_{\text{XUV}}(t) = -dA_{\text{XUV}}(t)/dt$ , where  $A_{\text{XUV0}}$  is its peak field strength. For the time-delayed femtosecond IR laser pulse, the electric field profile is Gaussian, i.e.,

$$F_{\text{IR}}(t) = F_{\text{IR0}} \exp\left(-\frac{2 \ln 2(t - \tau - T_{\text{XUV}}/2)^2}{T_{\text{IR}}^2}\right) \times \cos[\omega_{\text{IR}}(t - \tau - T_{\text{XUV}}/2)], \quad (4)$$

where  $F_{\text{IR0}}$  is the peak field strength,  $\tau$  the time delay between the two pulses,  $\omega_{\text{IR}}$  the central frequency of the IR field, and  $T_{\text{IR}}$  the FWHM duration of the temporal intensity profile of the IR laser pulse. In this work, both the first and second ionization events of  $H_2$  are overwhelmingly induced by the IR laser pulse, i.e., the XUV pulse is relatively weak with its central photon energy well below the first ionization threshold of  $H_2$ . For dissociative double ionization of  $H_2$ , the three involved charge states correspond to  $H_2$ ,  $H_2^+$ , and  $H^+ + H^+$ , respectively.

For a specific charge state, the total wave function  $|\Psi(t)\rangle$  satisfies the TDSE  $i|\dot{\Psi}(t)\rangle = H(t)|\Psi(t)\rangle$ , with  $H(t)$  from Eq. (1) and  $|\Psi(t)\rangle$  expressed using the ansatz

$$|\Psi(t)\rangle = \sum_m \int d\vec{R} \chi_m(\vec{R},t) |\phi_{R,m}^{\text{el}}\rangle \otimes |\vec{R}\rangle, \quad (5)$$

where  $\chi_m(\vec{R},t)$  is the nuclear wave function corresponding to the electronic state  $|\phi_{R,m}^{\text{el}}\rangle$ . Similar to the jump operator in Eq. (2), the total wave function in Eq. (5) is also a coherent superposition of bound electronic states. Substituting Eq. (5) into the TDSE and projecting on the electronic eigenstate  $\langle \phi_{R,m}^{\text{el}}|$ , we obtain a system of coupled equations for the nuclear wave functions

$$i\dot{\chi}_m(\vec{R},t) = \left(T_N + E_m^{\text{el}}(\vec{R}) - \frac{i}{2}\Gamma_m(\vec{R},t)\right) \chi_m(\vec{R},t) + \sum_{k \neq m} V_{mk}(\vec{R},t) \chi_k(\vec{R},t), \quad (6)$$

with  $V_{mk}(\vec{R},t) = \langle \phi_{R,m}^{\text{el}} | V_L(t) | \phi_{R,k}^{\text{el}} \rangle = -\langle \phi_{R,m}^{\text{el}} | \vec{\mu} | \phi_{R,k}^{\text{el}} \rangle \cdot \vec{F}(t)$ , where we have neglected nonadiabatic couplings. The last term in Eq. (6) describes the influence from the dipole couplings between the  $|\phi_{R,m}^{\text{el}}\rangle$  state and the other states within a given system, e.g., in either  $H_2$  or  $H_2^+$ . Equation (6) shows that the nuclear wave packet  $\chi_m(\vec{R},t)$  evolves along its electronic potential energy surface  $E_m^{\text{el}}(\vec{R})$  accompanied by coherent coupling with the other bound electronic states in the same charge state and ionization loss to the adjacent charge state.

We assume that the molecule is aligned along the linear polarization direction of  $\vec{F}(t)$ . This assumption reduces the three-dimensional coupled equations to one-dimensional equations and the equations of motion within a given charge state

can be written in matrix-vector form as

$$i \frac{\partial}{\partial t} \begin{bmatrix} \dots \\ \chi_m(R,t) \\ \dots \\ \chi_k(R,t) \\ \dots \end{bmatrix} = \begin{bmatrix} \dots & \dots & \dots \\ \dots & -\frac{d^2}{dR^2} + E_m^{\text{el}}(R) - \frac{i}{2}\Gamma_m(R,t) & \dots \\ \dots & \dots & \dots \\ \dots & \dots & V_{km}(R,t) \\ \dots & \dots & \dots \end{bmatrix} \begin{bmatrix} \dots \\ \chi_m(R,t) \\ \dots \\ \chi_k(R,t) \\ \dots \end{bmatrix}, \quad (7)$$

where each  $\chi_m(R,t)$  is expanded in a primitive basis for the  $R$  degree of freedom. To obtain the complete nuclear dynamics for double ionization of  $\text{H}_2$ , we solve Eq. (7) in three charge states corresponding to  $\text{H}_2$ ,  $\text{H}_2^+$ , and  $\text{H}^+ + \text{H}^+$ , respectively. It is the quantum jump that transfers nuclear motion in a given charge state to nuclear motion in the charge state with one electron less. Thus, in our model, we have the first jump from  $\text{H}_2$  to  $\text{H}_2^+$  following the first ionization and the second jump from  $\text{H}_2^+$  to  $\text{H}^+ + \text{H}^+$  following the second ionization. In Fig. 1 the relevant Born-Oppenheimer potential energy curves are plotted. The energies corresponding to the ground and excited states of the neutral molecule are taken from accurate correlated *ab initio* calculations [28,29]. The cation energies are obtained from exact simulations using a one-electron diatomic molecule code [30]. The figure shows the potential energy curves for the six lowest electronic states of  $^1\Sigma_g^+$  and  $^1\Sigma_u^+$  symmetries in  $\text{H}_2$ , the potential energy curves for the two lowest electronic states in  $\text{H}_2^+$ , and the  $1/R$  Coulombic curve of  $\text{H}^+ + \text{H}^+$ . The dipole moment functions between electronic states entering the couplings  $V_{mk}(R,t)$  have been obtained through a configuration-interaction calculation for  $\text{H}_2$  by using a procedure similar to that described in Ref. [31] and taken from the literature for  $\text{H}_2^+$  [32].

To make Eq. (7) solvable, it is necessary to have an estimate of the state-resolved ionization rates  $\Gamma_m(R,t)$ . In  $\text{H}_2$ , the  $R$ -dependent ionization potentials  $I_m(R)$  of the considered singly excited states are much smaller than the ionization potential of the ground state (Fig. 1). Thus, in order to ensure ionization from the excited potential energy curves to work in the tunneling regime, the central wavelength of the IR laser pulse is chosen to be long enough to satisfy the corresponding ionization conditions, i.e., the IR photon energy  $\omega_{\text{IR}}$  should be smaller than the ionization potential for the highest-lying excited state in  $\text{H}_2$  in Fig. 1 and the Keldysh parameter  $\gamma$  for this state should be smaller than 1 [33]. Apart from numerically solving the TDSE [34], methods such as the molecular Ammosov-Delone-Krainov theory [35,36] and the weak-field asymptotic theory [37–41] have been developed to obtain analytical formulas for the tunneling ionization rates for molecules. The tunneling ionization rates from the two lowest electronic states in  $\text{H}_2^+$ , i.e., the  $1s\sigma_g$  and  $2p\sigma_u$  states, were *ab initio* values taken from Ref. [42]. Because of the charge-resonance-enhanced ionization (CREI), for the peak probe intensity used in this work, the  $R$ -dependent ionization rates from the  $2p\sigma_u$  state are relatively large at internuclear distances around  $R = 7$  and 11 a.u. Due to lack of more accurate published results, the tunneling ionization rates induced by the IR laser pulse from the excited states  $|\phi_{R,m}^{\text{el}}\rangle$  in  $\text{H}_2$  are approximated by the exponential factor in the tunneling formulas, i.e.,  $\Gamma_m(R,t) = \exp\{-2[\sqrt{2I_m(R)}]^3/[3F_{\text{IR}}(t)]\}$ . We apply the split-operator method to the short-time propagator

to solve Eq. (7) for  $\text{H}_2$  and  $\text{H}_2^+$  as specified by the quantum jumps from  $\text{H}_2$  to  $\text{H}_2^+$  and from  $\text{H}_2^+$  to  $\text{H}^+ + \text{H}^+$  (see below).

The practical application of the MCWP approach contains the following three steps. (i) In  $\text{H}_2$ , starting from the ground state of  $\text{H}_2$  ( $X^1\Sigma_g^+, v=0$ ), we first evolve the initial nuclear wave packet along the potential energy curves in  $\text{H}_2$  (we include 12 curves in this case) under the influence of the pump and probe pulses. The overall probability of staying in  $\text{H}_2$ , i.e.,  $P_{\text{H}_2}(t) = \sum_m \int dR |\chi_m(R,t)|^2$ , decreases over time since the IR pulse induces ionization. The first jumps from  $\text{H}_2$  to  $\text{H}_2^+$  are assumed to have a chance to occur at each time step and the ionization probability  $P_1(t)$  within a small time interval  $\Delta t$  around  $t$  during the presence of the IR field is the drop in the probability  $P_{\text{H}_2}(t)$  at adjacent time steps, i.e.,  $P_1(t) = P_{\text{H}_2}(t) - P_{\text{H}_2}(t + \Delta t)$ . For a given first jump time  $t_1$ , there are 12 individual pathways corresponding to jumps from the 12 involved potential energy curves to  $\text{H}_2^+$  and the relative probability from the potential energy curve for the  $|\phi_{R,m}^{\text{el}}\rangle$  state is  $P_{1m}(t_1) = \langle \Psi(t_1) | C_m^+ C_m | \Psi(t_1) \rangle / \sum_m \langle \Psi(t_1) | C_m^+ C_m | \Psi(t_1) \rangle$ . (ii) After the first ionization, the initial state in  $\text{H}_2^+$  after the first jump at  $t_1$  from the  $|\phi_{R,m}^{\text{el}}\rangle$  state is  $C_m | \Psi(t_1) \rangle = \sum_{k=g,u} \int dR \sqrt{\Gamma_m(R,t_1)} M_k(R) \chi_m(R,t_1) |\phi_{R,k}^{\text{el}}\rangle \otimes |R\rangle$ . Here  $g$  and  $u$  denote the  $1s\sigma_g$  and  $2p\sigma_u$  states in  $\text{H}_2^+$ , respectively, and  $M_k(R)$  describes the field-dressed ground state in  $\text{H}_2^+$  and it is taken from Ref. [27]. Inserting this normalized initial nuclear wave packet into Eq. (7), we obtain the evolution of the nuclear wave packets along the  $1s\sigma_g$  and  $2p\sigma_u$  curves under the influence of the IR pulse. The ionization probability within a time interval  $\Delta t$  around  $t$  for the second jump from  $\text{H}_2^+$  to  $\text{H}^+ + \text{H}^+$  is  $P_2(t; t_1) = P_{\text{H}_2^+}(t; t_1) - P_{\text{H}_2^+}(t + \Delta t; t_1)$ , where  $P_{\text{H}_2^+}(t; t_1) = \sum_{k=g,u} \int dR |\chi_k(R,t)|^2$  is the overall probability of being in  $\text{H}_2^+$  at time  $t$ . For a given second jump time  $t_2$ , the relative probabilities for the second jumps taking place from the two pathways, i.e., from the  $1s\sigma_g$  and  $2p\sigma_u$  curves to  $\text{H}^+ + \text{H}^+$ , are  $P_{2k}(t_2; t_1) = \langle \Psi(t_2) | C_k^+ C_k | \Psi(t_2) \rangle / \sum_k \langle \Psi(t_2) | C_k^+ C_k | \Psi(t_2) \rangle$  with  $k = g$  or  $u$ . (iii) After the second ionization, since there is only the Coulombic curve in  $\text{H}^+ + \text{H}^+$ , the term  $M_m$  in Eq. (2) for the second jump operators is unity, thus the initial wave packet in  $\text{H}^+ + \text{H}^+$ , corresponding to the case where the second jump takes place from the  $1s\sigma_g$  ( $2p\sigma_u$ ) curve, is, before normalization,  $\chi_c(R,t) = \sqrt{\Gamma_g(R,t_2)} \chi_g(R,t_2) [\sqrt{\Gamma_u(R,t_2)} \chi_u(R,t_2)]$ . After removing two electrons from  $\text{H}_2$ , the IR pulse has no influence on the evolution of the nuclear wave packets in  $\text{H}^+ + \text{H}^+$  and the nuclear KER spectra are obtained by projecting the renormalized nuclear wave packets  $\chi_c(R,t_2)$  in  $\text{H}^+ + \text{H}^+$  on the energy-normalized Coulomb waves  $K_E(R)$ , i.e.,

$$P_{E,mk}(t_2; t_1) = \left| \int dR K_E(R) \chi_c(R,t_2) \right|^2, \quad (8)$$

where  $m$  specifies that the first jump takes place from the  $|\phi_{R,m}^{\text{el}}\rangle$  state in  $\text{H}_2$ ,  $k$  specifies that the second jump takes place from the  $1s\sigma_g$  or  $2p\sigma_u$  state in  $\text{H}_2^+$ , and it is implied that  $\chi_c(R, t_2)$  carries the jump history, i.e., the first jump time  $t_1$  and the states  $|\phi_{R,m}^{\text{el}}\rangle$  and  $|\phi_{R,k}^{\text{el}}\rangle$  from which the first and second jumps take place. The total nuclear KER spectrum can be obtained through summing over the KER spectra describing jumps from different states in  $\text{H}_2$  and  $\text{H}_2^+$  at different first and second jump times, i.e.,

$$P_E = \sum_{m,t_1,k,t_2} P_1(t_1)P_{1m}(t_1)P_2(t_2;t_1)P_{2k}(t_2;t_1) \times P_{E,mk}(t_2;t_1). \quad (9)$$

In order to produce converged results, the time interval  $\Delta t$  should be small enough, i.e.,  $\Delta t < \pi/(3\Delta E)$  [43], where  $\Delta E$  can be approximated by the largest ionization potential in Fig. 1. Thus, there are hundreds of time steps when the simulation time is a few tens of femtoseconds. Accordingly, there are hundreds of first and second jumps in Eq. (9), thus without efficient sampling and simulation procedures, it would be very resource and time demanding to obtain the KER spectrum following double ionization of  $\text{H}_2$ . In Appendix A we provide a detailed discussion and validation of our sampling method. For the parameters considered in Sec. III, the number of terms in Eq. (9) is reduced by a factor of  $\approx 3.3 \times 10^5$  compared to the conventional sampling method, leading, of course, to a significant speedup of the calculations.

### B. Validation of the MCWP approach in the XUV-IR scenario

In this section we validate the MCWP approach in the XUV-IR scenario. A complete test of the performance of the MCWP approach in simulating the double-ionization process in the XUV-IR scenario is impossible due to two facts. First, the process considered is not readily accessible by other theoretical approaches. Second, there are no experiments available for this process. This method can, however, be partially validated by comparing with available experimental or *ab initio* results for the single-ionization channel in the XUV-IR scenario. For instance, we have run a simulation under the same pulse parameters as in Ref. [44]: The two pulses have  $\sin^2$  envelopes, the central photon energy of the pump (probe) pulse is 10.885 (4.63) eV, the pump (probe) pulse has a duration of 2 fs (4 fs), and the peak intensity of the pump (probe) pulse is  $10^9$  W/cm<sup>2</sup> ( $10^{12}$  W/cm<sup>2</sup>). The ionization probability following single ionization of  $\text{H}_2$  is presented in Fig. 2 as a function of delay between the pump and probe pulses together with the *ab initio* and model calculations from Ref. [44]. Good agreement between the results for the three cases is observed, thus validating the application of the MCWP approach to the XUV-IR scenario. In our MCWP calculation, the ionization rates from the excited states induced by the probe pulse are calculated using the formula developed for the photoelectric effect [45].

## III. RESULTS AND DISCUSSION

In this section, the nuclear KER spectra after double ionization of  $\text{H}_2$  in an XUV-pump-IR-probe setup are obtained and analyzed. An isolated ultrashort XUV pulse is first applied to pump the ground state of  $\text{H}_2$  to the excited states

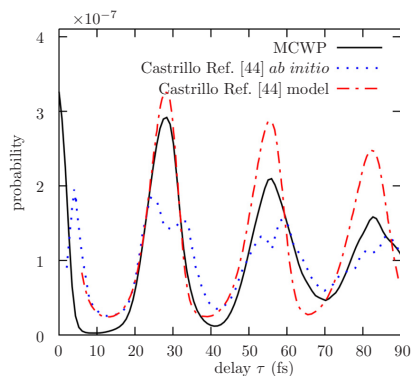


FIG. 2. Single-ionization probability of  $\text{H}_2$  as a function of delay  $\tau$  between the pump and probe pulses. The solid black curve is from our calculation. The dot-dashed red and dotted blue curves are from the model and *ab initio* calculations by González-Castrillo *et al.* [44], respectively. Both the pump and probe pulses have  $\sin^2$  envelopes. The laser parameters are as follows: The central photon energy of the pump (probe) pulse is 10.885 (4.63) eV, the pump (probe) pulse has a duration of 2 fs (4 fs), and the peak intensity of the pump (probe) pulse is  $10^9$  W/cm<sup>2</sup> ( $10^{12}$  W/cm<sup>2</sup>).

of  $^1\Sigma_u^+$  symmetry in  $\text{H}_2$  via a one-photon absorption process. Strong coupling between the excited states of different symmetries,  $^1\Sigma_g^+$  and  $^1\Sigma_u^+$  symmetries, and sequential double ionization are then induced by a time-delayed intense femtosecond IR laser pulse. For the results presented in this section, the central frequency of the XUV pulse is chosen to make the  $B^1\Sigma_u^+$  state in  $\text{H}_2$  resonantly excited at the equilibrium internuclear distance of the  $X^1\Sigma_g^+$  curve, i.e.,  $\omega_{\text{XUV}} = 0.46$  a.u. Excitation to higher-lying excited states of  $^1\Sigma_u^+$  symmetry is unavoidable due to the bandwidth of the XUV pulse. This is the reason why we include six singly excited states of  $^1\Sigma_u^+$  symmetry and six of  $^1\Sigma_g^+$  symmetry in  $\text{H}_2$  in our present model. The central wavelength of the IR pulses is 2400 nm, i.e., the IR photon energy is  $\omega_{\text{IR}} = 0.019$  a.u. This energy is smaller than the ionization potential from  $\text{H}_2$  to  $\text{H}_2^+$  for the highest-lying state in  $\text{H}_2$ , thus the IR field can induce tunneling ionization ( $\gamma < 1$ ) from excited states in  $\text{H}_2$  when its the peak field strength is  $F_{\text{IR}0} = 0.04$  a.u. The peak field strength of the XUV pulse is  $A_{\text{XUV}0}\omega_{\text{XUV}} = 0.005338$  a.u. To explore the influence of the XUV pulse duration on the excited nuclear dynamics in  $\text{H}_2$ , we consider three different cases where the XUV pulse durations  $T_{\text{XUV}}$  are one, three, and five optical cycles, corresponding to  $T_{\text{XUV}} = 334, 1002,$  and  $1671$  as, while the pulse duration of the IR laser pulses is fixed at three optical cycles ( $T_{\text{IR}} = 24$  fs). We have found that a time step of  $\Delta t = 1$  a.u. and a spatial step of  $\Delta R = 0.02$  a.u. ensure convergence of the results presented here (see Appendix A).

### A. Kinetic energy release spectra

We first show the nuclear KER distribution after double ionization of  $\text{H}_2$  when the pulse duration of the XUV pulse is

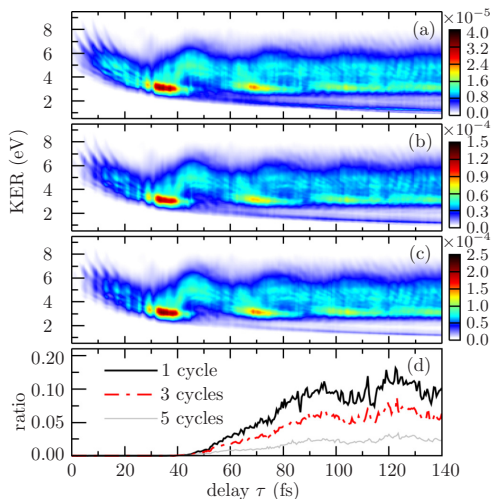


FIG. 3. Nuclear KER distributions as a function of the pump-probe delay  $\tau$  following double ionization of  $H_2$  in the XUV-pump-IR-probe setup when the pulse durations of the XUV pulses are (a) one, (b) three, and (c) five optical cycles, i.e., 334, 1002, and 1670 as, respectively. The central frequency of the XUV (IR) pulse is 0.46 a.u. (0.019 a.u.). The pulse duration of the IR laser pulse is three optical cycles, i.e.,  $T_{\text{IR}} = 24$  fs. The XUV (IR) pulse has a peak electric field strength of 0.005 338 a.u. (0.04 a.u.). The proton yields in the three panels are plotted to the power of 0.6 in order to gain a larger visibility of the structures. The pulse shapes are given in Eqs. (3) and (4). (d) Ratios between the signals on the energy decreasing branches, which are apparent for delays larger than 50 fs with KER values decreasing from around 2 to around 1 eV, and the total yield for the three XUV durations as a function of delay.

one optical cycle, i.e.,  $T_{\text{XUV}} = 13.7$  a.u. = 334 as, in Fig. 3(a). When the delay is increased from 0 to around 10 fs, there are several branches with KER values decreasing from around 10 to around 5 eV. This behavior results from the nuclear wave-packet motion along the two potential energy curves in  $H_2^+$ , i.e., the  $1s\sigma_g$  and  $2p\sigma_u$  curves, moving from smaller to larger internuclear distances. Such a manifestation is also consistent with the fact that the proton yields are much smaller for smaller delays due to smaller ionization rates out of the  $1s\sigma_g$  and  $2p\sigma_u$  curves at smaller internuclear distances. For this small delay range ( $\tau < 10$  fs), the XUV pulse is within the FWHM region of the IR pulse where the IR field is strong, thus there is nearly no time for the nuclear wave packets in  $H_2$  to move since they are ionized to  $H_2^+$  very quickly. For delays larger than 10 fs, the nuclear wave packets in  $H_2$  have time to move along the excited potential energy curves in  $H_2$  before substantial ionization from  $H_2$  to  $H_2^+$  takes place. For the (10–30)-fs delay range, the KER values of the protons decrease from around 5 to around 4 eV, due to the spread of the nuclear wave packets in  $H_2$ . Further increasing the delay from 30 to around 40 fs, there are significant enhancements of the proton yields for KER values around 3 eV. These enhancements result from the fact that the

nuclear wave packets in  $H_2^+$  after the first ionization have time to reach internuclear distances around the CREI [46] position of  $R \approx 11$  a.u. where ionization takes place with a large probability [42]. The enhancements of the proton yields for KER values increasing from 3 to 5 and then decreasing back to 3 eV within the (40–60)-fs delay range is related to the nuclear wave packets moving from larger internuclear distances to smaller internuclear distances and then back to larger internuclear distances. When the delay is larger than 60 fs, the enhancements of the proton yields at KER values around 3 eV, i.e., in the (70–80)-fs range and in the (90–110)-fs range, have a similar origin as the above-mentioned enhancements of the signal at KER values around 3 eV within the (30–40)-fs delay range. This periodic occurrence implies that the vibrational period of the contributing nuclear wave packets is around 30 fs. Due to the spread of the nuclear wave packets in  $H_2$ , the structures of the enhancements of the signal at KER values around 5 eV for delays larger than 60 fs are, however, not easy to observe. The energy decreasing branch with KER values starting from around 2 to around 1 eV for delays larger than 50 fs comes from the nuclear wave packets reaching internuclear distances larger than  $R \approx 6$  a.u. in  $H_2$ , which, as we will see, are originating from the dissociating part of the nuclear wave packets evolving along the  $B' \ ^1\Sigma_u^+$  curve [Fig. 5(e)].

To illustrate the influence of the XUV pulse duration on the excited nuclear dynamics in  $H_2$ , we show in Figs. 3(b) and 3(c) the nuclear KER distributions after double ionization of  $H_2$  when the XUV pulse duration are three and five optical cycles, respectively. The main structures of these two figures are similar to the ones in Fig. 3(a). This similarity is due to the fact that the XUV pulse is extremely short for the three cases and a very short XUV pulse creates nuclear wave packets in the excited states that resemble the initial ground vibrational state in the Franck-Condon approximation. When the XUV pulse duration is increased, this approximation breaks down and the nuclear KER spectra dramatically differ from Fig. 3. For the three panels in Fig. 3, there are small differences appearing at small delays ( $\tau < 30$  fs). For example, the periodic enhancements and suppressions of the proton yield every half of an IR laser cycle for  $\tau < 30$  fs become much easier to recognize when increasing the duration of the XUV pulse. Similar to those in Ref. [47], the periodic enhancements and suppressions of the proton yields originate from the population transfer between the ground state and the dominant excited state, i.e., the  $B' \ ^1\Sigma_u^+$  state, by the XUV pulse and its dependence on the IR field strengths around the instants of the short XUV pulse. If the IR field is weak (strong) around the instant of time when the XUV pulse is on, the Stark shift of the excited state by the IR field is small (large), thus the population transfer is large (small) due to resonant (off-resonant) coupling between the two states. When the population transfer from the ground state to the excited states in  $H_2$  is large, the proton yields following double ionization are enhanced; otherwise they are suppressed. The reason why the periodic enhancements and suppressions become clearer for larger XUV durations is that the smaller bandwidth of the longer XUV pulse makes the population transfer more difficult for the same Stark shift. The main difference, appearing at large delays in Figs. 3(a)–3(c), is that the low-energy decreasing branch becomes less apparent when increasing the duration of the XUV pulse, which is

because the smaller bandwidth makes direct excitation from the ground state to the  $B^1\Sigma_u^+$  state (responsible for this branch) less likely. We plot in Fig. 3(d) the ratios between the signals in the energy decreasing branches and the total proton yields for the three XUV pulse durations, which clearly show that the energy decreasing branch is relatively less important for a larger XUV pulse duration.

### B. Trajectory and wave-packet analysis

Now we concentrate on identifying the origin of the above-outlined characteristic structures in Fig. 3. We first conduct a trajectory analysis for a specific characteristic feature in Fig. 3(a) as an example to show the strength of the MCWP approach in obtaining physical insights, including the state- and time-resolved information, of a given feature in the nuclear KER spectrum. Conducting a trajectory analysis is a unique possibility in the MCWP approach and it can tell us the individual contributions from all the involved trajectories to the signal for a specific KER value at a specific delay in the nuclear KER distribution. Here a trajectory means the complete dynamics leading to the final nuclear wave packet along the Coulombic curve. A trajectory is specified by four parameters: the first and second jump times  $t_1$  and  $t_2$  and the states from which the first and second jumps take place. Thus, by performing the trajectory analysis, we can, for any given feature in the KER spectra, identify the propagation in the neutral  $H_2$ , the first jump time from the  $H_2$  to the  $H_2^+$  system, the propagation in  $H_2^+$ , and the final second jump from  $H_2^+$  to the Coulomb explosion channel. It is interesting to analyze the nuclear KER spectra for  $\tau \approx 71.5$  fs in Fig. 3(a) since at least two important structures are apparent for this value of the time delay  $\tau$ , e.g., the enhancements of the proton yields at KER values around 3 eV and low-energy decreasing branch starting from  $\tau \approx 50$  fs. When we carry out an analysis of the contributions to the signal at a given KER value in a nuclear KER spectrum, it is possible to obtain the origin of the signals at other KER values at the same time. This is because the signals for all the KER values in the same nuclear spectrum are formed from the same collection of trajectories with each trajectory giving its individual contribution to a particular feature. Thus, we present in Figs. 4(b)–4(d) the results obtained after a trajectory analysis to the signal for a KER equal to 3 eV at  $\tau = 71.5$  fs in Fig. 3(a). Figure 4(b) shows the respective probabilities for the first jump taking place from the states in  $H_2$  for the considered energy (3.0 eV). We can see that the first jumps from the  $H\bar{H}^1\Sigma_g^+$  and  $B3^1\Sigma_u^+$  states make the largest contributions to the signal. In Figs. 4(c) and 4(d), the contributions from the trajectories for the first jump taking place from the  $H\bar{H}^1\Sigma_g^+$  and  $B3^1\Sigma_u^+$  states and the second jumps from the  $2p\sigma_u$  state are presented as a function of  $t_1$  and  $t_2$ , respectively. Contributions from the trajectories for the second jumps taking place from the  $1s\sigma_g$  state are not presented since they give much smaller contributions because the ionization rates from the  $1s\sigma_g$  curve are about two orders of magnitude smaller than those from the  $2p\sigma_u$  curve.

For a fixed first jump time, a clear periodic dependence of the dominant trajectories on the second jump time  $t_2$  is observed in Figs. 4(c) and 4(d). These dominant trajectories correspond to ionization events taking place at instants around

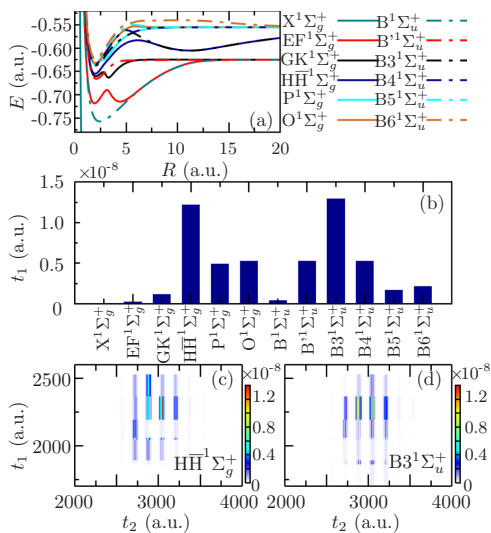


FIG. 4. Trajectory analysis for the enhancement of the proton yields at a specific point in Fig. 3(a): with the KER equal to 3 eV and  $\tau = 71.5$  fs. (a) For better visibility, the potential energy curves for the 12 states of  $1\Sigma_g^+$  and  $1\Sigma_u^+$  symmetries in  $H_2$  are plotted within the energy region between  $-0.5$  and  $-0.8$  eV. (b) Contributions from different states in  $H_2$  to the signal of the considered energy. Also shown are the trajectories making contributions to the signal from the (c)  $H\bar{H}^1\Sigma_g^+$  and (d)  $B3^1\Sigma_u^+$  states. The other laser parameters are as follows:  $\omega_{XUV} = 0.46$  a.u.,  $\omega_{IR} = 0.019$  a.u.,  $I_{XUV} = 13.7$  a.u. (334 as), and  $T_{IR} = 992$  a.u. (24 fs). The peak electric field strengths are 0.005 338 and 0.04 a.u. for the XUV and the IR fields, respectively. The pulse shapes are given in Eqs. (3) and (4).

the field extrema with large second ionization rates from the  $2p\sigma_u$  curve in  $H_2^+$ . For the  $H\bar{H}^1\Sigma_g^+$  state, the most important trajectory corresponds to the first jump occurring at 2193 a.u. (53 fs) and the second jump at around 3039 a.u. (74 fs). For the  $B3^1\Sigma_u^+$  state, the most important trajectory is the first jump occurring at 2193 a.u. (53 fs) and the second jump at around 2889 a.u. (70 fs). The time difference between the first and second jump times for the two cases (21 and 17 fs) is the evolution time of the nuclear wave packets in  $H_2^+$ . The enhancements at around 3.0 eV in Fig. 3(a) are mainly from ionization events occurring at the CREI position of  $R \approx 11$  a.u. from the  $2p\sigma_u$  curve in  $H_2^+$ . These evolution times in  $H_2^+$  imply that the contributing nuclear wave packets move slowly along the  $2p\sigma_u$  curve. This can be verified by the relatively small kinetic energies for these two trajectories before the second ionization taking place, which is the difference between the final kinetic energy and the Coulomb repulsion energy at around  $R \approx 11$  a.u., i.e.,  $3 \text{ eV} - (1/11) \text{ a.u.} \times 27.21 \text{ eV/a.u.} = 0.53 \text{ eV}$ . Thus, the kinetic energies of the contributing nuclear wave packets at  $t_1 = 2193$  a.u. (53 fs) obtained by moving along the  $H\bar{H}^1\Sigma_g^+$  and  $B3^1\Sigma_u^+$  curves are very small and the internuclear distances of the contributing nuclear wave packets along these two curves at  $t_1 = 2193$  a.u. (53 fs) are quite large.



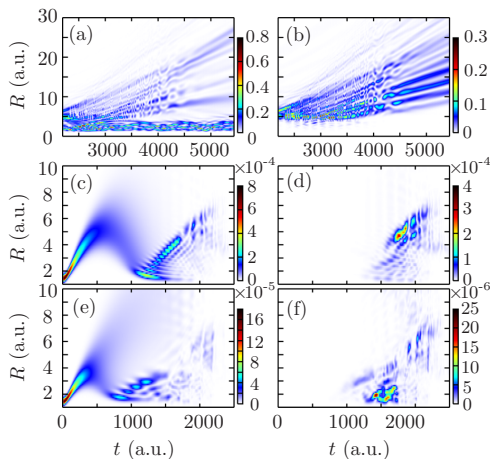


FIG. 5. Evolution of the nuclear wave packets  $|\chi_m(R, t)|^2$  along the (a)  $1s\sigma_g$  and (b)  $2p\sigma_u$  curves in  $H_2^+$  from the  $H\bar{H}^1\Sigma_g^+$  state when the first jump occurs at  $t_1 = 2193$  a.u. (53 fs), which corresponds to the first jump time  $t_1$  of the most important trajectory in Fig. 4(c). Also shown is the evolution of the nuclear wave packets along the (c)  $B^1\Sigma_u^+$ , (d)  $EF^1\Sigma_g^+$ , (e)  $B'^1\Sigma_u^+$ , and (f)  $H\bar{H}^1\Sigma_g^+$  curves in  $H_2$ . The laser parameters are identical to those in Fig. 4.

To confirm this speculation, we show in Figs. 5(a) and 5(b) the evolution of the nuclear wave packets along the  $1s\sigma_g$  and  $2p\sigma_u$  curves in  $H_2^+$  when the first jump takes place at  $t_1 = 2193$  a.u. (53 fs) from the  $H\bar{H}^1\Sigma_g^+$  state. As seen from Fig. 4(b), the  $B^1\Sigma_u^+$  state is as important as the  $H\bar{H}^1\Sigma_g^+$  state. The nuclear wave packets motion along the two  $H_2^+$  curves for the first jumps occurring from the  $B^1\Sigma_u^+$  state at  $t_1 = 2193$  a.u. can be obtained and analyzed in the same way as the wave packets from the  $H\bar{H}^1\Sigma_g^+$  state. We have found that the main features of the evolution of the nuclear wave packets in  $H_2^+$  are very similar irrespective of whether the intermediate  $H\bar{H}^1\Sigma_g^+$  and  $B^1\Sigma_u^+$  states are used and therefore here we only show the results associated with the  $H\bar{H}^1\Sigma_g^+$  state in Figs. 5(a) and 5(b) (see Appendix B for the results associated with the  $B^1\Sigma_u^+$  state). Now let us return to Fig. 5(b), where we can clearly see that the nuclear wave packet moving along the  $2p\sigma_u$  curve, starting from around  $R \approx 6.2$  a.u., reaches internuclear distances around the CREI position of  $R \approx 11$  a.u. at around  $t_2 = 3039$  a.u. (74 fs).

We can also see from Fig. 5(b) that the nuclear wave packet at  $t_2 = 3039$  a.u. is distributed over a very broad range of internuclear distances, i.e., from  $R = 5$  to 15 a.u. Thus, apart from the above-mentioned nuclear wave packet at around  $R = 11$  a.u., the other part of the nuclear wave packet would result in different structures in the nuclear KER spectrum. This means that a detailed analysis of this trajectory is worthwhile. Because of the  $R$ -dependent ionization rates out of the  $2p\sigma_u$  curve in  $H_2^+$ , nuclear wave packets along the  $2p\sigma_u$  curve located at internuclear distances with larger ionization rates are more likely to be ionized to  $H_2^{2+}$ . Thus, for a given trajectory,

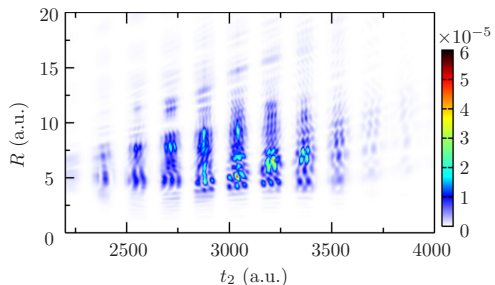


FIG. 6. Initial nuclear wave packets in  $H_2^{2+}$  at different second jump times for the second jumps occurring from the  $2p\sigma_u$  state in  $H_2^+$ , i.e.,  $|\chi_c(R, t_2)|^2$ , when the first jump occurs from the  $H\bar{H}^1\Sigma_g^+$  state at  $t_1 = 2193$  a.u.

the initial nuclear wave packet in  $H_2^{2+}$  is dependent not only on the nuclear wave packet in  $H_2^+$  at its second jump time  $t_2$  but also on the instantaneous ionization rates from  $H_2^+$  to  $H_2^{2+}$  at  $t_2$ , as discussed in Sec. II. In Fig. 6 we show the initial nuclear wave packets in  $H_2^{2+}$  at different second jump times for the second jumps occurring from the  $2p\sigma_u$  state in  $H_2^+$ , when the first jump occurs from the  $H\bar{H}^1\Sigma_g^+$  state in  $H_2$  at  $t_1 = 2193$  a.u. We can see that for the most dominant trajectory discussed above, i.e., for the trajectory where the first jump takes place from the  $H\bar{H}^1\Sigma_g^+$  state at  $t_1 = 2193$  a.u. and the second jump from the  $2p\sigma_u$  state at  $t_2 = 3039$  a.u., there are enhancements of the nuclear wave packet densities at around  $R = 5, 10$ , and 15 a.u. By applying the reflection approximation, i.e.,  $KER \approx \frac{1}{R}$ , such enhancements would result in KER signals peaking at around 5.5, 3, and 2 eV for this considered delay, respectively, which are consistent with the features in the nuclear KER spectrum for the 71.5-fs delay in Fig. 3(a).

To obtain knowledge of the initial wave packets in  $H_2^+$  we plot the evolution of the nuclear wave packets in  $H_2$  along the  $H\bar{H}^1\Sigma_g^+$  state in Fig. 5(f). The two regions with large probabilities at around  $t \approx 1500$  a.u. (37 fs) and  $t \approx 2000$  a.u. (49 fs) are from large dipole couplings between this state and the adjacent  $B'^1\Sigma_u^+$  state. The evolution of the nuclear wave packets in the  $B'^1\Sigma_u^+$  state is plotted in Fig. 5(e). We can see that the population of the nuclear wave packets in the  $H\bar{H}^1\Sigma_g^+$  state is out of phase with that in the  $B'^1\Sigma_u^+$  state for these two regions, i.e.,  $t \approx 1500$  and 2000 a.u., directly showing a time-dependent population transfer between these two states. That is, at certain instants of time when there is a maximum of population in the  $B'^1\Sigma_u^+$  state [Fig. 5(e)], there is a minimum of population in the  $H\bar{H}^1\Sigma_g^+$  state [Fig. 5(f)] and vice versa. To find the origin of the regions with large probabilities in Figs. 5(e) and 5(f), time evolution behaviors of the nuclear wave packets along the  $B^1\Sigma_u^+$  and  $EF^1\Sigma_g^+$  curves are also presented in Figs. 5(c) and 5(d). By examining the out-of-phase behavior of the nuclear wave packets in Figs. 5(c) and 5(d), it is clear that the large probabilities at internuclear distances  $R \approx 6$  a.u. originate from the large dipole coupling from the dominant  $B^1\Sigma_u^+$  state to the adjacent

$EF^1\Sigma_g^+$  state due to a one-photon resonance occurring. A similar out-of-phase behavior of the nuclear wave packets in the  $EF^1\Sigma_g^+$  and  $B^1\Sigma_u^+$  states for time larger than  $t = 2000$  a.u. can be observed by comparing Figs. 4(d) and 4(e). Thus, the enhancements of the proton yields at KER values around 3.0 eV for the 71.5-fs delay in Fig. 3(a) are mainly from the first jumps taking place at around 2193 a.u. (53 fs) from the  $H\bar{H}^1\Sigma_g^+$  state through a population transfer process, i.e.,  $B^1\Sigma_u^+ \rightarrow EF^1\Sigma_g^+ \rightarrow B^1\Sigma_u^+ \rightarrow H\bar{H}^1\Sigma_g^+$  at internuclear distances around  $R \approx 6$  a.u. Moreover, the enhancements at KER values around 3.0 eV for the three delay ranges in Fig. 3(a) are consistent with the moving nuclear wave packets along the  $B^1\Sigma_u^+$  curve periodically reaching its outer turning point around every 30 fs.

Applying the reflection principle, the nuclear wave packets at around  $R = 5.5$  a.u. along the  $2p\sigma_u$  curve in  $H_2^+$  [Fig. 5(b)] at around  $t_2 = 3000$  a.u. (73 fs) result in the enhancements of the proton yields at KER values around 5 eV for the 71.5-fs delay in Fig. 3(a), i.e.,  $\frac{1}{55} \times 27.2 \approx 5$  eV. In fact, for delays larger than 30 fs in Fig. 3(a), it is also the nuclear wave packets at around  $R = 5.5$  a.u. that result in the enhancements of the proton yields at KER values around 5 eV. Moreover, the structure for KER increasing from 3 eV to 5 eV and then decreasing back to 3 eV in the (40–60)-fs delay range in Fig. 3(a) manifests the motion of the nuclear wave packet along the  $B^1\Sigma_u^+$  curve in  $H_2$  when the nuclear wave packets along the  $B^1\Sigma_u^+$  curve are away from the outer turning points. The 20-fs delay range is consistent with the vibrational period of the nuclear wave packets along the  $B^1\Sigma_u^+$  curve [Fig. 5(e)]. Apart from that, the fast moving nuclear wave packets starting at around  $R = 8$  a.u. in Fig. 5(b), which originate from the dissociating part of the nuclear wave packets in the  $B^1\Sigma_u^+$  curve [Fig. 5(e)], later reach distances around  $R = 15$  a.u. at instants of time when the instantaneous field strength becomes maximal. From the reflection principle, the nuclear wave packet located at around  $R = 15$  a.u. results in the appearance of the signals at KER values around  $\frac{1}{15} \times 27.2$  eV = 1.8 eV for the 71.5-fs delay. This KER value is decreased (increased) for a (smaller) larger delay because the dissociation nuclear wave packet in the  $B^1\Sigma_u^+$  state would reach larger (smaller) internuclear distances. Thus, energy decreasing branches show up in Fig. 3. As a result, one can benefit greatly from conducting a trajectory analysis to a given feature in the nuclear KER spectrum in uncovering its origin and the origins of other features in the considered nuclear KER spectrum. By conducting an analysis similar to that for the other characteristic structures in the nuclear KER distribution in Fig. 3, a thorough understanding of the formation of the structures can be achieved.

#### IV. CONCLUSION

We have extended the MCWP approach to simulate the fragmentation upon double ionization of  $H_2$  in an XUV-pump-IR-probe setup where the ultrafast dynamics of singly excited states is involved. We have applied the MCWP approach to this XUV-IR scenario after providing a validation of this method in this scenario. This theoretical study accounts for the ionization induced by the intense IR pulse from the excited states in  $H_2$ ,

reached from the ground state of  $H_2$  by an XUV pulse, and again the ionization from  $H_2^+$  to  $H^+ + H^+$ . We have obtained the nuclear KER distributions for three different pump-probe schemes using XUV pulses of durations of one, three, and five optical cycles, respectively, to excite  $H_2$  for the pump-probe delays ranging from 0 to 140 fs. The nuclear dynamics in molecular excited states is reflected in the characteristic features in the nuclear KER distributions and, for instance, the periodic nuclear motion in the  $B^1\Sigma_u^+$  state is mapped out by trajectory and wave-packet analysis. Apart from that, the Stark effect can play a role in determining the efficiency of population transfer from the ground state to the excited states in  $H_2$  for time delays  $\tau < 30$  fs. The present MCWP approach can be applied to XUV-pump-IR-probe attosecond spectroscopy of any molecule to resolve and control ultrafast dynamics in excited states through laser-induced double-ionization processes, provided the Born-Oppenheimer potential energy curves in different charge states, the dipole moment functions between different states, and the state-resolved ionization rates are available.

#### ACKNOWLEDGMENTS

This work was supported by the European Union Horizon 2020 research and innovation program under the Marie Skłodowska-Curie Grant Agreement No. 641789 MEDEA, the Villum Kann Rasmussen Center of Excellence, QUSCOPE, and MINECO Project No. FIS2016-77889-R (Spain). A.P. acknowledges a Ramón y Cajal contract from the Ministerio de Economía y Competitividad (Spain). The MCWP results presented in this work were obtained at the Centre for Scientific Computing, Aarhus, and the dipole transitions moments at the CCC-UAM computer center, Madrid.

#### APPENDIX A: SAMPLING METHOD

In this appendix we give a detailed description and validation of the MCWP sampling method for XUV-pump-IR-probe spectroscopy. Within the MCWP approach, in order to reproduce experimental results, the time step  $\Delta t$  and the space step  $\Delta R$  should be chosen small enough. We have found that  $\Delta t = 1$  a.u. and  $\Delta R = 0.02$  a.u. give converged results for the processes studied in this work. Apart from that, in order to capture the features of the nuclear motion at large internuclear distances, such as the CREI [46] regions for the  $2p\sigma_u$  state, and also to reduce the reflection from the boundaries, the simulation box should be large enough, e.g.,  $R_{\text{box}} \gtrsim 40$  a.u. For the approach in this work, the first jumps from  $H_2$  to  $H_2^+$  take place at every time step and the second jumps take place from  $H_2^+$  to  $H^+ + H^+$  at every time step after the first jumps. In addition, the first jumps have 12 pathways and the second jumps have two pathways, corresponding to the number of states included in  $H_2$  and  $H_2^+$ , respectively. Thus, for an IR pulse with a duration of 24 fs (992 a.u.), there are at least  $12 \times 2 \times 992^3/3$  terms in Eq. (9). The reduction of the huge number of terms in Eq. (9) to a computationally more feasible level is the task of our sampling method.

In fact, the sampling method in our previous works involving only IR fields [10,18,22,24–26] is very resource and time saving, since it assumes that the first jumps occur at the field

extrema of the IR laser pulse and the second jumps take place at every tenth time step after the first jumps. In those works, laser-induced coupling between the ground and excited states in  $H_2$  was neglected, since more than eight photons were required to resonantly excite the ground state to the lowest excited state in  $H_2$  for the 800-nm wavelength. Such coupling became even more unlikely for mid-IR wavelengths. Thus it was acceptable to only include the ground-state potential energy curve, i.e., the  $X^1\Sigma_g^+$  curve, in  $H_2$  in the calculations. The assumption for the second jumps works well since its sampling points are dense enough to capture the dynamics due to the relatively low velocities of the nuclear motion. The assumption for the first jumps is reasonable due to two facts. First, the nuclear wave packet along the  $X^1\Sigma_g^+$  potential energy curve in  $H_2$  does not change significantly during the evolution. Such a stability of the nuclear wave packet results from the initial wave packet in  $H_2$  being centered around the equilibrium internuclear distance, i.e.,  $R \approx 1.4$  a.u., of the  $X^1\Sigma_g^+$  curve. Second, the very small ionization rates from the  $X^1\Sigma_g^+$  curve increase when increasing the field strength from zero to the peak field strength of the applied laser pulses. Thus, within half an optical cycle where the field strength increases from zero to an extremum and then decreases back again, the first jump occurring at the field extremum describes the events with the largest first ionization probability. Thus, under these assumptions, the number of terms in Eq. (9) is reduced to around  $2 \times 6$  (first jump times)  $\times 99$  (second jump times) from  $2 \times 992^3/3$  for a 2400-nm IR laser pulse with a duration of 24 fs.

The above assumption for the first jumps, however, no longer works in the present XUV-pump-IR-probe case, because of the spread of the nuclear wave packets in the excited states of  $H_2$ . Now the ionization probability  $P_1(t)$  within a time interval  $\Delta t$  depends not only on the instantaneous field strength at time  $t$  but also on the spatial distribution of the nuclear wave packets in  $H_2$  at  $t$ , due to the relatively rapid variations of the large ionization rates out of the excited potential energy curves in  $H_2$  with respect to  $R$ . Thus, the first jump at a given field extremum does not necessarily have the largest probability among the jumps occurring within the same half of the optical cycle, as shown in Fig. 7. In Fig. 7(a), the population in  $H_2$  and the ionization probability within a time interval  $\Delta t$  during the presence of the IR field, i.e.,  $P_{H_2}(t)$  and  $P_1(t)$ , are plotted as a function of  $t$  for an illustrative case: The central frequency of the XUV (IR) pulse is  $\omega_{XUV} = 0.46$  a.u. ( $\omega_{IR} = 0.019$  a.u.), the duration of the XUV (IR) pulse is  $T_{XUV} = 1 \times (2\pi/\omega_{XUV}) = 13.7$  a.u. = 334 as [ $T_{IR} = 3 \times (2\pi/\omega_{IR}) = 992$  a.u. = 24 fs], the peak field strength of the XUV (IR) pulse is  $A_{XUV}\omega_{XUV} = 0.005338$  a.u. ( $F_{IR0} = 0.04$  a.u.), and the pump-probe delay is  $\tau = 33.5$  fs. For better observation of the dependence of  $P_{H_2}(t)$  and  $P_1(t)$  on the instantaneous external field strength, the electric field of the IR pulse  $F_{IR}(t)$  is plotted in Fig. 7(b). The  $t$  axis in Fig. 7(a) is confined from 0 to 1000 a.u., since the population in  $H_2$ ,  $P_{H_2}(t)$ , starts to converge to 0.99955 for  $t$  larger than 1000 a.u. in spite of the presence of the IR pulse. This means that nearly all the excited molecules are ionized by the IR field before  $t \approx 1000$  a.u. In our sampling method, we first determine the instants when the ionization probability  $P_1(t)$  is locally maximized or minimized, which correspond to the instants for the local maxima and minima of the black line

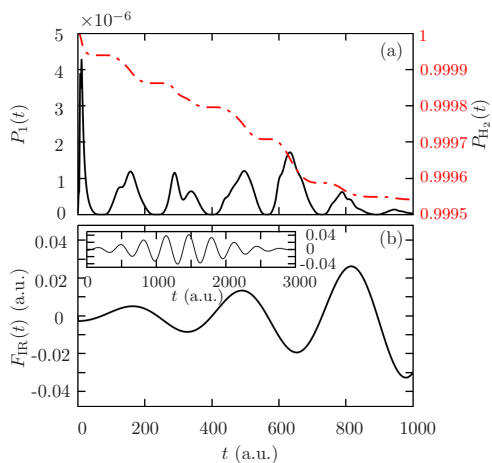


FIG. 7. (a) Probability in  $H_2$  (dot-dashed red curve),  $P_{H_2}(t)$ , and ionization probability  $P_1(t)$  within a time interval of  $\Delta t = 1$  (solid black curve) from  $H_2$  as a function of time during the presence of the IR field. (b) Electric field of the IR pulse in the same time range as (a); for reference the inset shows the electric field of the IR pulse until the turnoff of the IR pulse. The laser parameters are as follows:  $\omega_{XUV} = 0.46$  a.u.,  $\omega_{IR} = 0.019$  a.u. ( $\lambda_{IR} = 2400$  nm),  $T_{XUV} = 1 \times (2\pi/\omega_{XUV}) = 13.7$  a.u. (334 as),  $T_{IR} = 3 \times (2\pi/\omega_{IR}) = 992$  a.u. (24 fs), and time delay  $\tau = 33.5$  fs. The peak electric field strengths are 0.005338 and 0.04 a.u. for the XUV and the IR fields, respectively. The expressions for the two pulses are given in Eqs. (3) and (4).

in Fig. 7(a). The first jumps are assumed to take place at the instants for the local maxima of the black line in Fig. 7(a). For a given first jump taking place at the instant for a given local maximum, the instants for the adjacent left and right local minima  $t_{1L}$  and  $t_{1R}$  are used to define its ionization probability under our sampling method. The new ionization probability  $P_{1new}(t_1)$  at a given first jump time  $t_1$  now becomes the sum over the ionization probabilities within a time interval  $\Delta t$  at each time step between  $t_{1L}$  and  $t_{1R}$ , i.e.,  $P_{1new}(t_1) = \sum_{t=t_{1L}}^{t=t_{1R}} P_1(t)$ . Sampling of the second jump times is the same as in our previous works, i.e., assuming them to occur at every tenth time step. Instead of summing over the ionization probabilities within  $\Delta t$  for the ten time steps around  $t$ , i.e.,  $\sum_t^{t+10\Delta t} P_2(t; t_1)$ , the new ionization probability for the second jump occurring at  $t$  is chosen the same as before, i.e.,  $P_{2new}(t; t_1) = P_2(t; t_1)$ . This assumption is reasonable since the ratio between  $P_2(t_2; t_1)$  and  $P_2(t_2 + 10\Delta t; t_1)$  is nearly the same as the ratio between  $\sum_{t_2}^{t_2+10\Delta t} P_2(t_2; t_1)$  and  $\sum_{t_2}^{t_2+10\Delta t} P_2(t_2 + 10\Delta t; t_1)$ , since the positions of the nuclear wave packets in  $H_2^+$  almost remain the same and the external field does not change significantly in ten time steps. Thus, compared with summing over the ionization probabilities within  $\Delta t$  for ten time steps as the ionization probabilities for the second jumps, our choice of the second ionization probabilities only influences the absolute values of the nuclear KER yields but keeps the shape of the nuclear KER spectra unchanged.



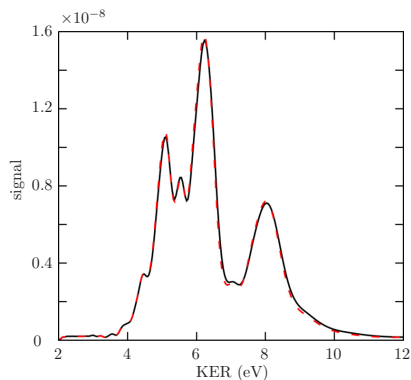


FIG. 8. Nuclear KER spectra obtained through applying the original sampling method (solid black curve) and the sampling method presented in this work (dashed red curve). The  $P_E$  on the vertical axis labels the probability to produce a signal at a given energy. The laser parameters are identical to those for Fig. 7(a) except that a 0.5-fs pump-probe delay is used.

In order to validate our sampling method, we have conducted comparisons between results obtained from this and the original sampling method. As an example, the nuclear KER spectra obtained by these two sampling methods are presented in Fig. 8. The laser parameters are identical to those in Fig. 7(a) except that the pump-probe delay is  $\tau = 0.5$  fs. The excellent agreement between the two curves in Fig. 8 clearly shows that the sampling method presented herein works very well. Our method can reduce the number of terms in Eq. (9) from about  $12 \times 2 \times 992^3/3$  to about  $12 \times 2 \times 10 \times 99$ . Thus, we apply the MCWP approach with this much more efficient sampling method to obtain the results presented in Sec. III.

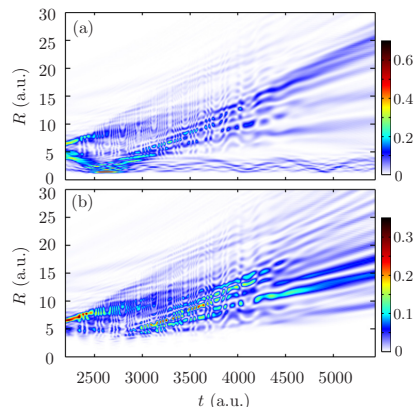


FIG. 9. Evolution of the nuclear wave packets along the (a)  $1s\sigma_g$  and (b)  $2p\sigma_u$  curves in  $H_2^+$  when the first jump occurs from the  $B3^1\Sigma_u^+$  state in  $H_2$  at  $t_1 = 2193$  a.u.

#### APPENDIX B: NUCLEAR WAVE PACKETS IN $H_2^+$ FROM $B3^1\Sigma_u^+$

In this appendix we show in Fig. 9 the nuclear wave packets along the  $1s\sigma_g$  and  $2p\sigma_u$  states in  $H_2^+$  when the first jump occurs at  $t_1 = 2193$  a.u. from the  $B3^1\Sigma_u^+$  state in  $H_2$ . We can clearly see that the evolution of the nuclear wave packets for the first jump occurring from the  $B3^1\Sigma_u^+$  state (Fig. 9) is very similar to that for the first jump occurring from the  $H\bar{H}^1\Sigma_g^+$  state [Figs. 5(a) and 5(b)]. This means that at a given second jump time  $t_2$ , the trajectory whose first jump takes place at  $t_1 = 2193$  a.u. from the  $B3^1\Sigma_u^+$  state would result in a nuclear KER spectrum similar to that associated with the trajectory whose first jump takes place at  $t_1 = 2193$  a.u. from the  $H\bar{H}^1\Sigma_g^+$  state.

- [1] N. R. Isenor, V. Merchant, R. S. Hallsworth, and M. C. Richardson, CO<sub>2</sub> laser-induced dissociation of SiF<sub>4</sub> molecules into electronically excited fragments, *Can. J. Phys.* **51**, 1281 (1973).
- [2] K. Codling and L. J. Frasinski, Dissociative ionization of small molecules in intense laser fields, *J. Phys. B* **26**, 783 (1993).
- [3] H. Niikura, F. Légaré, R. Hasbani, A. D. Bandrauk, M. Y. Ivanov, D. M. Villeneuve, and P. B. Corkum, Sub-laser-cycle electron pulses for probing molecular dynamics, *Nature (London)* **417**, 917 (2002).
- [4] H. Niikura, F. Légaré, R. Hasbani, M. Y. Ivanov, D. M. Villeneuve, and P. B. Corkum, Probing molecular dynamics with attosecond resolution using correlated wave packet pairs, *Nature (London)* **421**, 826 (2003).
- [5] M. F. Kling, C. Siedschlag, A. J. Verhoef, J. I. Khan, M. Schultze, T. Uphues, Y. Ni, M. Uiberacker, M. Drescher, F. Krausz, and M. J. J. Vrakking, Control of electron localization in molecular dissociation, *Science* **312**, 246 (2006).
- [6] I. Znakovskaya, P. von den Hoff, G. Marcus, S. Zherebtsov, B. Bergues, X. Gu, Y. Deng, M. J. J. Vrakking, R. Kienberger, F. Krausz, R. de Vivie-Riedle, and M. F. Kling, Subcycle Controlled Charge-Directed Reactivity with Few-Cycle Midinfrared Pulses, *Phys. Rev. Lett.* **108**, 063002 (2012).
- [7] V. Wanie, H. Ibrahim, S. Baulieu, N. Thiré, B. E. Schmidt, Y. Deng, A. S. Alnaser, I. V. Litvinyuk, X.-M. Tong, and F. Légaré, Coherent control of D<sub>2</sub>/H<sub>2</sub> dissociative ionization by a mid-infrared two-color laser field, *J. Phys. B* **49**, 025601 (2015).
- [8] A. S. Alnaser, X. M. Tong, T. Osipov, S. Voss, C. M. Maharjan, P. Ranitovic, B. Ulrich, B. Shan, Z. Chang, C. D. Lin, and C. L. Cocke, Routes to Control of H<sub>2</sub> Coulomb Explosion in Few-Cycle Laser Pulses, *Phys. Rev. Lett.* **93**, 183202 (2004).
- [9] A. Staudte, D. Pavičić, S. Chelkowski, D. Zeidler, M. Meckel, H. Niikura, M. Schöffler, S. Schössler, B. Ulrich, P. P. Rajeev, T. Weber, T. Jahnke, D. M. Villeneuve, A. D. Bandrauk, C. L. Cocke, P. B. Corkum, and R. Dörner, Attosecond Stroboscopic

- Two-Surface Population Dynamics in Dissociating  $\text{H}_2^+$ , *Phys. Rev. Lett.* **98**, 073003 (2007).
- [10] H. A. Leth, L. B. Madsen, and K. Mølmer, Monte Carlo Wave Packet Theory of Dissociative Double Ionization, *Phys. Rev. Lett.* **103**, 183601 (2009).
- [11] K. P. Singh, F. He, P. Ranitovic, W. Cao, S. De, D. Ray, S. Chen, U. Thumm, A. Becker, M. M. Murnane, H. C. Kapteyn, I. V. Litvinyuk, and C. L. Cocke, Control of Electron Localization in Deuterium Molecular Ions using an Attosecond Pulse Train and a Many-Cycle Infrared Pulse, *Phys. Rev. Lett.* **104**, 023001 (2010).
- [12] F. Kelkensberg, W. Siu, J. F. Pérez-Torres, F. Morales, G. Gademann, A. Rouzée, P. Johnsson, M. Lucchini, F. Calegari, J. L. Sanz-Vicario, F. Martín, and M. J. J. Vrakking, Attosecond Control in Photoionization of Hydrogen Molecules, *Phys. Rev. Lett.* **107**, 043002 (2011).
- [13] G. Sansone, F. Kelkensberg, J. Pérez-Torres, F. Morales, M. F. Kling, W. Siu, O. Ghafur, P. Johnsson, M. Swoboda, E. Benedetti *et al.*, Electron localization following attosecond molecular photoionization, *Nature (London)* **465**, 763 (2010).
- [14] A. González-Castrillo, A. Palacios, H. Bachau, and F. Martín, Clocking Ultrafast Wave Packet Dynamics in Molecules Through UV-Induced Symmetry Breaking, *Phys. Rev. Lett.* **108**, 063009 (2012).
- [15] A. R. Bainbridge, J. Harrington, A. Kirrander, C. Cacho, E. Springate, W. A. Bryan, and R. S. Minns, VUV excitation of a vibrational wavepacket in  $\text{D}_2$  measured through strong-field dissociative ionization, *New J. Phys.* **17**, 103013 (2015).
- [16] F. P. Sturm, X. M. Tong, A. Palacios, T. W. Wright, I. Zalyubovskaya, D. Ray, N. Shivaram, F. Martín, A. Belkacem, P. Ranitovic, and T. Weber, Mapping and controlling ultrafast dynamics of highly excited  $\text{H}_2$  molecules by VUV-IR pump-probe schemes, *Phys. Rev. A* **95**, 012501 (2017).
- [17] T. Ergler, A. Rudenko, B. Feuerstein, K. Zrost, C. D. Schröter, R. Moshhammer, and J. Ullrich, Time-Resolved Imaging and Manipulation of  $\text{H}_2$  Fragmentation in Intense Laser Fields, *Phys. Rev. Lett.* **95**, 093001 (2005).
- [18] H. A. Leth, L. B. Madsen, and K. Mølmer, Monte Carlo wave packet approach to dissociative multiple ionization in diatomic molecules, *Phys. Rev. A* **81**, 053409 (2010).
- [19] J. Dalibard, Y. Castin, and K. Mølmer, Wave-Function Approach to Dissipative Processes in Quantum Optics, *Phys. Rev. Lett.* **68**, 580 (1992).
- [20] K. Mølmer, Y. Castin, and J. Dalibard, Monte Carlo wave-function method in quantum optics, *J. Opt. Soc. Am. B* **10**, 524 (1993).
- [21] H. J. Carmichael, *An Open Systems Approach to Quantum Optics* (Springer, Berlin, 1993).
- [22] H. A. Leth, L. B. Madsen, and K. Mølmer, Dissociative double ionization of  $\text{H}_2$  and  $\text{D}_2$ : Comparison between experiment and Monte Carlo wave packet calculations, *Phys. Rev. A* **81**, 053410 (2010).
- [23] H. A. Leth and L. B. Madsen, Dissociative multiple ionization of diatomic molecules by extreme-ultraviolet free-electron-laser pulses, *Phys. Rev. A* **83**, 063415 (2011).
- [24] H. A. Leth, Dissociative ionization—A study using the Monte Carlo wave packet approach, Ph.D. thesis, Aarhus University, 2011.
- [25] Q. Jing and L. B. Madsen, Laser-induced dissociative ionization of  $\text{H}_2$  from the near-infrared to the mid-infrared regime, *Phys. Rev. A* **94**, 063402 (2016).
- [26] Q. Jing, Monte Carlo wave packet approach to dissociative double ionization of  $\text{H}_2$  interacting with intense laser pulses, M.Sc. thesis, Aarhus University, 2016.
- [27] H. Kono, Y. Sato, Y. Fujimura, and I. Kawata, Identification of the doorway states to ionization of molecules in intense laser fields, *Laser Phys.* **13**, 883 (2003).
- [28] L. Wolniewicz and K. Dressler, The  $EF$ ,  $GK$ , and  $H\bar{H}^1\Sigma_g^+$  states of hydrogen. Improved *ab initio* calculation of vibrational states in the adiabatic approximation, *J. Chem. Phys.* **82**, 3292 (1985).
- [29] G. Staszewska and L. Wolniewicz, Adiabatic energies of excited  $^1\Sigma_g^+$  states of the hydrogen molecule, *J. Mol. Spectrosc.* **212**, 208 (2002).
- [30] J. D. Power, Fixed nuclei two-centre problem in quantum mechanics, *Philos. Trans. R. Soc. London Ser. A* **274**, 663 (1973).
- [31] A. Palacios, H. Bachau, and F. Martín, Excitation and ionization of molecular hydrogen by ultrashort vuv laser pulses, *Phys. Rev. A* **75**, 013408 (2007).
- [32] J. T. Lin and T. F. Jiang, Photodissociation of  $\text{H}_2^+$  in intense chirped laser fields, *Phys. Rev. A* **63**, 013408 (2000).
- [33] L. V. Keldysh, Ionization in the field of a strong electromagnetic wave, *Sov. Phys. JETP* **20**, 1307 (1965).
- [34] M. Awasthi, Y. V. Vanne, A. Saenz, A. Castro, and P. Decleva, Single-active-electron approximation for describing molecules in ultrashort laser pulses and its application to molecular hydrogen, *Phys. Rev. A* **77**, 063403 (2008).
- [35] X. M. Tong, Z. X. Zhao, and C. D. Lin, Theory of molecular tunneling ionization, *Phys. Rev. A* **66**, 033402 (2002).
- [36] X. M. Tong and C. D. Lin, Empirical formula for static field ionization rates of atoms and molecules by lasers in the barrier-suppression regime, *J. Phys. B* **38**, 2593 (2005).
- [37] O. I. Tolstikhin, T. Morishita, and L. B. Madsen, Theory of tunneling ionization of molecules: Weak-field asymptotics including dipole effects, *Phys. Rev. A* **84**, 053423 (2011).
- [38] L. B. Madsen, O. I. Tolstikhin, and T. Morishita, Application of the weak-field asymptotic theory to the analysis of tunneling ionization of linear molecules, *Phys. Rev. A* **85**, 053404 (2012).
- [39] O. I. Tolstikhin, L. B. Madsen, and T. Morishita, Weak-field asymptotic theory of tunneling ionization in many-electron atomic and molecular systems, *Phys. Rev. A* **89**, 013421 (2014).
- [40] A. I. Dnestryan and O. I. Tolstikhin, Integral-equation approach to the weak-field asymptotic theory of tunneling ionization, *Phys. Rev. A* **93**, 033412 (2016).
- [41] L. B. Madsen, F. Jensen, A. I. Dnestryan, and O. I. Tolstikhin, Structure factors for tunneling ionization rates of molecules: General Hartree-Fock-based integral representation, *Phys. Rev. A* **96**, 013423 (2017).
- [42] M. Plummer and J. F. McCann, Field-ionization rates of the hydrogen molecular ion, *J. Phys. B* **29**, 4625 (1996).
- [43] M. R. Hermann and J. A. Fleck, Split-operator spectral method for solving the time-dependent Schrödinger equation in spherical coordinates, *Phys. Rev. A* **38**, 6000 (1988).
- [44] A. González-Castrillo, J. F. Pérez-Torres, A. Palacios, and F. Martín, Probing vibrational wave packets in molecular excited states, *Theor. Chem. Acc.* **128**, 735 (2011).

- [45] H. A. Bethe and E. E. Salpeter, *Quantum Mechanics of One- and Two-Electron Atoms* (Springer Science + Business Media, New York, 2012).
- [46] T. Zuo and A. D. Bandrauk, Charge-resonance-enhanced ionization of diatomic molecular ions by intense lasers, *Phys. Rev. A* **52**, R2511 (1995).
- [47] P. Ranitovic, X.-M. Tong, B. Gramkow, S. De, B. DePaola, K. Singh, W. Cao, M. Magrakvelidze, D. Ray, I. Bocharova *et al.*, IR-assisted ionization of helium by attosecond extreme ultraviolet radiation, *New J. Phys.* **12**, 013008 (2010).



---

# Bibliography

- [1] U. Keller, G. W. 'tHooft, W. H. Knox, and J. E. Cunningham, "Femtosecond pulses from a continuously self-starting passively mode-locked Ti:sapphire laser," *Opt. Lett.* **16**, 1022 (1991).
- [2] A. Stingl, C. Spielmann, F. Krausz, and R. Szipöcs, "Generation of 11-fs pulses from a Ti:sapphire laser without the use of prisms," *Opt. Lett.* **19**, 204 (1994).
- [3] A. Stingl, M. Lenzner, C. Spielmann, F. Krausz, and R. Szipöcs, "Sub-10-fs mirror-dispersion-controlled Ti:sapphire laser," *Opt. Lett.* **20**, 602 (1995).
- [4] J. Ringling, O. Kittelmann, F. Noack, G. Korn, and J. Squier, "Tunable femtosecond pulses in the near vacuum ultraviolet generated by frequency conversion of amplified Ti:sapphire laser pulses," *Opt. Lett.* **18**, 2035 (1993).
- [5] M. R. X. de Barros and P. C. Becker, "Two-color synchronously mode-locked femtosecond Ti:sapphire laser," *Opt. Lett.* **18**, 631 (1993).
- [6] C.-H. Pai, Y.-Y. Chang, L.-C. Ha, Z.-H. Xie, M.-W. Lin, J.-M. Lin, Y.-M. Chen, G. Tsaur, H.-H. Chu, S.-H. Chen, J.-Y. Lin, J. Wang, and S.-Y. Chen, "Generation of intense ultrashort mid-infrared pulses by laser-plasma interaction in the bubble regime," *Phys. Rev. A* **82**, 063804 (2010).

- [7] E. A. Stepanov, A. A. Lanin, A. A. Voronin, A. B. Fedotov, and A. M. Zheltikov, “Solid-State Source of Subcycle Pulses in the Midinfrared,” *Phys. Rev. Lett.* **117**, 043901 (2016).
- [8] A. A. Zholents and M. S. Zolotarev, “Femtosecond X-Ray Pulses of Synchrotron Radiation,” *Phys. Rev. Lett.* **76**, 912 (1996).
- [9] R. W. Schoenlein, S. Chattopadhyay, H. H. W. Chong, T. E. Glover, P. A. Heimann, C. V. Shank, A. A. Zholents, and M. S. Zolotarev, “Generation of Femtosecond Pulses of Synchrotron Radiation,” *Science* **287**, 2237 (2000), <http://science.sciencemag.org/content/287/5461/2237.full.pdf> .
- [10] V. Ayvazyan, N. Baboi, I. Bohnet, R. Brinkmann, M. Castellano, P. Castro, L. Catani, S. Choroba, A. Cianchi, M. Dohlus, *et al.*, “Generation of GW Radiation Pulses from a VUV Free-Electron Laser Operating in the Femtosecond Regime,” *Phys. Rev. Lett.* **88**, 104802 (2002).
- [11] P. Emma, K. Bane, M. Cornacchia, Z. Huang, H. Schlarb, G. Stupakov, and D. Walz, “Femtosecond and Subfemtosecond X-Ray Pulses from a Self-Amplified Spontaneous-Emission–Based Free-Electron Laser,” *Phys. Rev. Lett.* **92**, 074801 (2004).
- [12] P. Antoine, A. L’Huillier, and M. Lewenstein, “Attosecond Pulse Trains Using High–Order Harmonics,” *Phys. Rev. Lett.* **77**, 1234 (1996).
- [13] P. M. Paul, E. S. Toma, P. Breger, G. Mullot, F. Augé, P. Balcou, H. G. Muller, and P. Agostini, “Observation of a Train of Attosecond Pulses from High Harmonic Generation,” *Science* **292**, 1689 (2001), <http://science.sciencemag.org/content/292/5522/1689.full.pdf> .
- [14] J. Mauritsson, P. Johnsson, E. Gustafsson, A. L’Huillier, K. J. Schafer, and M. B. Gaarde, “Attosecond Pulse Trains Generated Using Two Color Laser Fields,” *Phys. Rev. Lett.* **97**, 013001 (2006).
- [15] C. Spielmann, N. H. Burnett, S. Sartania, R. Koppitsch, M. Schnürer, C. Kan, M. Lenzner, P. Wobrauschek, and

- F. Krausz, "Generation of Coherent X-rays in the Water Window Using 5-Femtosecond Laser Pulses," *Science* **278**, 661 (1997), <http://science.sciencemag.org/content/278/5338/661.full.pdf> .
- [16] X. Feng, S. Gilbertson, H. Mashiko, H. Wang, S. D. Khan, M. Chini, Y. Wu, K. Zhao, and Z. Chang, "Generation of Isolated Attosecond Pulses with 20 to 28 Femtosecond Lasers," *Phys. Rev. Lett.* **103**, 183901 (2009).
- [17] G. Sansone, E. Benedetti, F. Calegari, C. Vozzi, L. Avaldi, R. Flammini, L. Poletto, P. Villoresi, C. Altucci, R. Velotta, S. Stagira, S. De Silvestri, and M. Nisoli, "Isolated Single-Cycle Attosecond Pulses," *Science* **314**, 443 (2006), <http://science.sciencemag.org/content/314/5798/443.full.pdf> .
- [18] M. Hentschel, R. Kienberger, C. Spielmann, G. A. Reider, N. Milosevic, T. Brabec, P. Corkum, U. Heinzmann, M. Drescher, and F. Krausz, "Attosecond metrology," *Nature* **414**, 509 (2001).
- [19] H. Mashiko, S. Gilbertson, C. Li, S. D. Khan, M. M. Shakya, E. Moon, and Z. Chang, "Double Optical Gating of High-Order Harmonic Generation with Carrier-Envelope Phase Stabilized Lasers," *Phys. Rev. Lett.* **100**, 103906 (2008).
- [20] J. H. Posthumus, J. Plumridge, M. K. Thomas, K. Codling, L. J. Frasinski, A. J. Langley, and P. F. Taday, "Dynamic and geometric laser-induced alignment of molecules in intense laser fields," *Journal of Physics B: Atomic, Molecular and Optical Physics* **31**, L553 (1998).
- [21] M. Tsubouchi, B. J. Whitaker, L. Wang, H. Kohguchi, and T. Suzuki, "Photoelectron Imaging on Time-Dependent Molecular Alignment Created by a Femtosecond Laser Pulse," *Phys. Rev. Lett.* **86**, 4500 (2001).
- [22] S. De, I. Znakovskaya, D. Ray, F. Anis, N. G. Johnson, I. A. Bocharova, M. Magrakvelidze, B. D. Esry, C. L. Cocke, I. V. Litvinyuk, and M. F. Kling, "Field-Free Orientation of CO Molecules by Femtosecond Two-Color Laser Fields," *Phys. Rev. Lett.* **103**, 153002 (2009).

- [23] L. J. Frasinski, J. H. Posthumus, J. Plumridge, K. Codling, P. F. Taday, and A. J. Langley, "Manipulation of Bond Hardening in  $\text{H}_2^+$  by Chirping of Intense Femtosecond Laser Pulses," *Phys. Rev. Lett.* **83**, 3625 (1999).
- [24] A. Giusti-Suzor, X. He, O. Atabek, and F. H. Mies, "Above-threshold dissociation of  $\text{H}_2^+$  in intense laser fields," *Phys. Rev. Lett.* **64**, 515 (1990).
- [25] C. Cornaggia, J. Lavancier, D. Normand, J. Morellec, P. Agostini, J. P. Chambaret, and A. Antonetti, "Multielectron dissociative ionization of diatomic molecules in an intense femtosecond laser field," *Phys. Rev. A* **44**, 4499 (1991).
- [26] S. Chelkowski, C. Foisy, and A. D. Bandrauk, "Electron-nuclear dynamics of multiphoton  $\text{H}_2^+$  dissociative ionization in intense laser fields," *Phys. Rev. A* **57**, 1176 (1998).
- [27] A. Assion, T. Baumert, M. Bergt, T. Brixner, B. Kiefer, V. Seyfried, M. Strehle, and G. Gerber, "Control of Chemical Reactions by Feedback-Optimized Phase-Shaped Femtosecond Laser Pulses," *Science* **282**, 919 (1998), <http://science.sciencemag.org/content/282/5390/919.full.pdf> .
- [28] M. F. Kling, C. Siedschlag, A. J. Verhoef, J. I. Khan, M. Schultze, T. Uphues, Y. Ni, M. Uiberacker, M. Drescher, F. Krausz, and M. J. J. Vrakking, "Control of Electron Localization in Molecular Dissociation," *Science* **312**, 246 (2006), <http://science.sciencemag.org/content/312/5771/246.full.pdf> .
- [29] G. Sansone, F. Kelkensberg, J. Pérez-Torres, F. Morales, M. F. Kling, W. Siu, O. Ghafur, P. Johnsson, M. Swoboda, E. Benedetti, *et al.*, "Electron localization following attosecond molecular photoionization," *Nature* **465**, 763 (2010).
- [30] K. P. Singh, F. He, P. Ranitovic, W. Cao, S. De, D. Ray, S. Chen, U. Thumm, A. Becker, M. M. Murnane, H. C. Kapteyn, I. V. Litvinyuk, and C. L. Cocke, "Control of Electron Localization in Deuterium Molecular Ions using an Attosecond Pulse Train and a Many-Cycle Infrared Pulse," *Phys. Rev. Lett.* **104**, 023001 (2010).



- 
- [31] C. I. Blaga, J. Xu, A. D. DiChiara, E. Sistrunk, K. Zhang, P. Agostini, T. A. Miller, L. F. DiMauro, and C. Lin, “Imaging ultrafast molecular dynamics with laser-induced electron diffraction,” *Nature* **483**, 194 (2012).
- [32] M. Meckel, D. Comtois, D. Zeidler, A. Staudte, D. Pavičić, H. C. Bandulet, H. Pépin, J. C. Kieffer, R. Dörner, D. M. Villeneuve, and P. B. Corkum, “Laser-Induced Electron Tunneling and Diffraction,” *Science* **320**, 1478 (2008), <http://science.sciencemag.org/content/320/5882/1478.full.pdf> .
- [33] M. Lein, “Molecular imaging using recolliding electrons,” *J. Phys. B: At., Mol. Opt. Phys.* **40**, R135 (2007).
- [34] L. Cederbaum and J. Zobeley, “Ultrafast charge migration by electron correlation,” *Chemical Physics Letters* **307**, 205 (1999).
- [35] P. M. Kraus, B. Mignolet, D. Baykusheva, A. Rupenyan, L. Horný, E. F. Penka, G. Grassi, O. I. Tolstikhin, J. Schneider, F. Jensen, L. B. Madsen, A. D. Bandrauk, F. Remacle, and H. J. Wörner, “Measurement and laser control of attosecond charge migration in ionized iodoacetylene,” *Science* **350**, 790 (2015), <http://science.sciencemag.org/content/350/6262/790.full.pdf> .
- [36] T. Zuo and A. D. Bandrauk, “Charge-resonance-enhanced ionization of diatomic molecular ions by intense lasers,” *Phys. Rev. A* **52**, R2511 (1995).
- [37] S. Chelkowski, A. Conjusteau, T. Zuo, and A. D. Bandrauk, “Dissociative ionization of  $\text{H}_2^+$  in an intense laser field: Charge-resonance-enhanced ionization, Coulomb explosion, and harmonic generation at 600 nm,” *Phys. Rev. A* **54**, 3235 (1996).
- [38] H. Niikura, F. Légaré, R. Hasbani, M. Y. Ivanov, D. Villeneuve, and P. Corkum, “Probing molecular dynamics with attosecond resolution using correlated wave packet pairs,” *Nature* **421**, 826 (2003).
- [39] T. Ergler, A. Rudenko, B. Feuerstein, K. Zrost, C. D. Schröter, R. Moshhammer, and J. Ullrich, “Spatiotemporal Imaging of Ul-

- trafast Molecular Motion: Collapse and Revival of the  $D_2^+$  Nuclear Wave Packet,” *Phys. Rev. Lett.* **97**, 193001 (2006).
- [40] F. Kelkensberg, C. Lefebvre, W. Siu, O. Ghafur, T. T. Nguyen-Dang, O. Atabek, A. Keller, V. Serov, P. Johnsson, M. Swoboda, T. Remetter, A. L’Huillier, S. Zherebtsov, G. Sansone, E. Benedetti, F. Ferrari, M. Nisoli, F. Lépine, M. F. Kling, and M. J. J. Vrakking, “Molecular Dissociative Ionization and Wave-Packet Dynamics Studied Using Two-Color XUV and IR Pump-Probe Spectroscopy,” *Phys. Rev. Lett.* **103**, 123005 (2009).
- [41] M. Magrakvelidze, O. Herrwerth, Y. H. Jiang, A. Rudenko, M. Kurka, L. Foucar, K. U. Kühnel, M. Kübel, N. G. Johnson, C. D. Schröter, S. Düsterer, R. Treusch, M. Lezius, I. Ben-Itzhak, R. Moshhammer, J. Ullrich, M. F. Kling, and U. Thumm, “Tracing nuclear-wave-packet dynamics in singly and doubly charged states of  $N_2$  and  $O_2$  with XUV-pump–XUV-probe experiments,” *Phys. Rev. A* **86**, 013415 (2012).
- [42] S. Baker, J. S. Robinson, C. A. Haworth, H. Teng, R. A. Smith, C. C. Chirilă, M. Lein, J. W. G. Tisch, and J. P. Marangos, “Probing Proton Dynamics in Molecules on an Attosecond Time Scale,” *Science* **312**, 424 (2006), <http://science.sciencemag.org/content/312/5772/424.full.pdf> .
- [43] J. Itatani, J. Levesque, D. Zeidler, H. Niikura, H. Pépin, J.-C. Kieffer, P. B. Corkum, and D. M. Villeneuve, “Tomographic imaging of molecular orbitals,” *Nature* **432**, 867 (2004).
- [44] A. Assion, M. Geisler, J. Helbing, V. Seyfried, and T. Baumert, “Femtosecond pump-probe photoelectron spectroscopy: Mapping of vibrational wave-packet motion,” *Phys. Rev. A* **54**, R4605 (1996).
- [45] J. E. Bækhoj, L. Yue, and L. B. Madsen, “Nuclear-motion effects in attosecond transient-absorption spectroscopy of molecules,” *Phys. Rev. A* **91**, 043408 (2015).
- [46] I. Sánchez and F. Martín, “Origin of Unidentified Structures in Resonant Dissociative Photoionization of  $H_2$ ,” *Phys. Rev. Lett.* **79**, 1654 (1997).

- 
- [47] I. Sánchez and F. Martín, “Resonant dissociative photoionization of  $H_2$  and  $D_2$ ,” *Phys. Rev. A* **57**, 1006 (1998).
- [48] F. Martín, “Ionization and dissociation using B-splines: photoionization of the hydrogen molecule,” *J. Phys. B: At., Mol. Opt. Phys.* **32**, R197 (1999).
- [49] A. Palacios, J. L. Sanz-Vicario, and F. Martín, “Theoretical methods for attosecond electron and nuclear dynamics: applications to the  $H_2$  molecule,” *J. Phys. B: At., Mol. Opt. Phys.* **48**, 242001 (2015).
- [50] D. J. Haxton, K. V. Lawler, and C. W. McCurdy, “Multiconfiguration time-dependent Hartree-Fock treatment of electronic and nuclear dynamics in diatomic molecules,” *Phys. Rev. A* **83**, 063416 (2011).
- [51] S. Bauch, H. R. Larsson, C. Hinz, and M. Bonitz, “The time-dependent generalized active space configuration interaction approach to correlated ionization dynamics of diatomic molecules,” *J. Phys.: Conf. Ser.* **696**, 012008 (2016).
- [52] J. Dalibard, Y. Castin, and K. Mølmer, “Wave-function approach to dissipative processes in quantum optics,” *Phys. Rev. Lett.* **68**, 580 (1992).
- [53] H. A. Leth, L. B. Madsen, and K. Mølmer, “Monte Carlo Wave Packet Theory of Dissociative Double Ionization,” *Phys. Rev. Lett.* **103**, 183601 (2009).
- [54] H. A. Leth, L. B. Madsen, and K. Mølmer, “Monte Carlo wave packet approach to dissociative multiple ionization in diatomic molecules,” *Phys. Rev. A* **81**, 053409 (2010).
- [55] H. A. Leth, L. B. Madsen, and K. Mølmer, “Dissociative double ionization of  $H_2$  and  $D_2$ : Comparison between experiment and Monte Carlo wave packet calculations,” *Phys. Rev. A* **81**, 053410 (2010).
- [56] H. A. Leth and L. B. Madsen, “Dissociative multiple ionization of diatomic molecules by extreme-ultraviolet free-electron-laser pulses,” *Phys. Rev. A* **83**, 063415 (2011).

- [57] A. Staudte, D. Pavičić, S. Chelkowski, D. Zeidler, M. Meckel, H. Niikura, M. Schöffler, S. Schössler, B. Ulrich, P. P. Rajeev, T. Weber, T. Jahnke, D. M. Villeneuve, A. D. Bandrauk, C. L. Cocke, P. B. Corkum, and R. Dörner, “Attosecond Strobing of Two-Surface Population Dynamics in Dissociating  $\text{H}_2^+$ ,” *Phys. Rev. Lett.* **98**, 073003 (2007).
- [58] H. Fukuzawa, K. Motomura, X.-J. Liu, G. Prümper, M. Okunishi, K. Ueda, N. Saito, H. Iwayama, K. Nagaya, M. Yao, M. Nagasono, A. Higashiya, M. Yabashi, T. Ishikawa, H. Ohashi, and H. Kimura, “Ion momentum spectroscopy of  $\text{N}_2$  and  $\text{O}_2$  molecules irradiated by EUV free-electron laser pulses,” *J. Phys. B: At., Mol. Opt. Phys.* **42**, 181001 (2009).
- [59] R. Mitrić, J. Petersen, and V. Bonačić Koutecký, “Laser-field-induced surface-hopping method for the simulation and control of ultrafast photodynamics,” *Phys. Rev. A* **79**, 053416 (2009).
- [60] Q. Jing and L. B. Madsen, “Laser-induced dissociative ionization of  $\text{H}_2$  from the near-infrared to the mid-infrared regime,” *Phys. Rev. A* **94**, 063402 (2016).
- [61] Q. Jing, R. Y. Bello, F. Martín, A. Palacios, and L. B. Madsen, “Monte Carlo wave-packet approach to trace nuclear dynamics in molecular excited states by XUV-pump-IR-probe spectroscopy,” *Phys. Rev. A* **97**, 043426 (2018).
- [62] K. Schnorr, A. Senftleben, M. Kurka, A. Rudenko, L. Foucar, G. Schmid, A. Broska, T. Pfeifer, K. Meyer, D. Anielski, R. Boll, D. Rolles, M. Kübel, M. F. Kling, Y. H. Jiang, S. Mondal, T. Tachibana, K. Ueda, T. Marchenko, M. Simon, G. Brenner, R. Treusch, S. Scheit, V. Averbukh, J. Ullrich, C. D. Schröter, and R. Moshhammer, “Time-Resolved Measurement of Interatomic Coulombic Decay in  $\text{Ne}_2$ ,” *Phys. Rev. Lett.* **111**, 093402 (2013).
- [63] H. A. Leth, *Dissociative Ionization: A Study Using the Monte Carlo Wave Packet Approach*, Ph.D. thesis, Aarhus University (2011).

- 
- [64] M. Feit, J. Fleck, and A. Steiger, “Solution of the Schrödinger equation by a spectral method,” *J. Comput. Phys.* **47**, 412 (1982).
- [65] P. Schwendner, F. Seyl, and R. Schinke, “Photodissociation of  $\text{Ar}_2^+$  in strong laser fields,” *Chem. Phys.* **217**, 233 (1997), dynamics of Driven Quantum Systems.
- [66] T. D. G. Walsh, F. A. Ilkov, S. L. Chin, F. Châteauneuf, T. T. Nguyen-Dang, S. Chelkowski, A. D. Bandrauk, and O. Atabek, “Laser-induced processes during the Coulomb explosion of  $\text{H}_2$  in a Ti-sapphire laser pulse,” *Phys. Rev. A* **58**, 3922 (1998).
- [67] A. S. Alnaser, X. M. Tong, T. Osipov, S. Voss, C. M. Maharjan, P. Ranitovic, B. Ulrich, B. Shan, Z. Chang, C. D. Lin, and C. L. Cocke, “Routes to Control of  $\text{H}_2$  Coulomb Explosion in Few-Cycle Laser Pulses,” *Phys. Rev. Lett.* **93**, 183202 (2004).
- [68] S. Saugout, E. Charron, and C. Cornaggia, “ $\text{H}_2$  double ionization with few-cycle laser pulses,” *Phys. Rev. A* **77**, 023404 (2008).
- [69] S. Saugout and C. Cornaggia, “Temporal separation of  $\text{H}_2$  double-ionization channels using intense ultrashort 10-fs laser pulses,” *Phys. Rev. A* **73**, 041406 (2006).
- [70] V. Wanie, H. Ibrahim, S. Beaulieu, N. Thiré, B. E. Schmidt, Y. Deng, A. S. Alnaser, I. V. Litvinyuk, X.-M. Tong, and F. Légaré, “Coherent control of  $\text{D}_2/\text{H}_2$  dissociative ionization by a mid-infrared two-color laser field,” *J. Phys. B: At., Mol. Opt. Phys.* **49**, 025601 (2016).
- [71] T. Sharp, “Potential-energy curves for molecular hydrogen and its ions,” *Atomic Data and Nuclear Data Tables* **2**, 119 (1970).
- [72] J. T. Lin and T. F. Jiang, “Photodissociation of  $\text{H}_2^+$  in intense chirped laser fields,” *Phys. Rev. A* **63**, 013408 (2000).
- [73] O. I. Tolstikhin, T. Morishita, and L. B. Madsen, “Theory of tunneling ionization of molecules: Weak-field asymptotics including dipole effects,” *Phys. Rev. A* **84**, 053423 (2011).

- [74] O. I. Tolstikhin, L. B. Madsen, and T. Morishita, “Weak-field asymptotic theory of tunneling ionization in many-electron atomic and molecular systems,” *Phys. Rev. A* **89**, 013421 (2014).
- [75] M. Plummer and J. F. McCann, “Field-ionization rates of the hydrogen molecular ion,” *J. Phys. B: At., Mol. Opt. Phys.* **29**, 4625 (1996).
- [76] H. Kono, Y. Sato, Y. Fujimura, and I. Kawata, “Identification of the doorway states to ionization of molecules in intense laser fields,” *Laser physics* **13**, 883 (2003).
- [77] I. V. Litvinyuk, A. S. Alnaser, D. Comtois, D. Ray, A. T. Hasan, J.-C. Kieffer, and D. M. Villeneuve, “Wavelength-dependent study of strong-field Coulomb explosion of hydrogen,” *New J. Phys.* **10**, 083011 (2008).
- [78] T. Ergler, A. Rudenko, B. Feuerstein, K. Zrost, C. D. Schröter, R. Moshhammer, and J. Ullrich, “Time-Resolved Imaging and Manipulation of H<sub>2</sub> Fragmentation in Intense Laser Fields,” *Phys. Rev. Lett.* **95**, 093001 (2005).
- [79] Y. H. Jiang, A. Rudenko, J. F. Pérez-Torres, O. Herrwerth, L. Foucar, M. Kurka, K. U. Kühnel, M. Toppin, E. Plésiat, F. Morales, F. Martín, M. Lezius, M. F. Kling, T. Jahnke, R. Dörner, J. L. Sanz-Vicario, J. van Tilborg, A. Belkacem, M. Schulz, K. Ueda, T. J. M. Zouros, S. Düsterer, R. Treusch, C. D. Schröter, R. Moshhammer, and J. Ullrich, “Investigating two-photon double ionization of D<sub>2</sub> by XUV-pump–XUV-probe experiments,” *Phys. Rev. A* **81**, 051402 (2010).
- [80] A. R. Bainbridge, J. Harrington, A. Kirrander, C. Cacho, E. Springate, W. A. Bryan, and R. S. Minns, “VUV excitation of a vibrational wavepacket in D<sub>2</sub> measured through strong-field dissociative ionization,” *New J. Phys.* **17**, 103013 (2015).
- [81] Y. H. Jiang, A. Rudenko, J. F. Pérez-Torres, O. Herrwerth, L. Foucar, M. Kurka, K. U. Kühnel, M. Toppin, E. Plésiat, F. Morales, F. Martín, M. Lezius, M. F. Kling, T. Jahnke, R. Dörner, J. L. Sanz-Vicario, J. van Tilborg, A. Belkacem,

- M. Schulz, K. Ueda, T. J. M. Zouros, S. Düsterer, R. Treusch, C. D. Schröter, R. Moshhammer, and J. Ullrich, “Investigating two-photon double ionization of  $D_2$  by XUV-pump–XUV-probe experiments,” *Phys. Rev. A* **81**, 051402 (2010).
- [82] F. P. Sturm, X. M. Tong, A. Palacios, T. W. Wright, I. Zalyubovskaya, D. Ray, N. Shivaram, F. Martín, A. Belkacem, P. Ranitovic, and T. Weber, “Mapping and controlling ultrafast dynamics of highly excited  $H_2$  molecules by VUV-IR pump-probe schemes,” *Phys. Rev. A* **95**, 012501 (2017).
- [83] L. Wolniewicz and K. Dressler, “The EF, GK, and  $H\bar{H}^1\Sigma_g^+$  states of hydrogen. Improved ab initio calculation of vibrational states in the adiabatic approximation,” *J. Chem Phys.* **82**, 3292 (1985), <https://doi.org/10.1063/1.448228> .
- [84] G. Staszewska and L. Wolniewicz, “Adiabatic Energies of Excited  $^1\Sigma_u$  States of the Hydrogen Molecule,” *J. Mol. Spectrosc.* **212**, 208 (2002).
- [85] A. Palacios, H. Bachau, and F. Martín, “Excitation and ionization of molecular hydrogen by ultrashort vuv laser pulses,” *Phys. Rev. A* **75**, 013408 (2007).
- [86] P. M. Dehmer and W. A. Chupka, “On the mechanism for vibrational autoionization in  $H_2$ ,” *J. Chem. Phys.* **66**, 1972 (1977), <https://doi.org/10.1063/1.434154> .
- [87] C. Bordas, P. F. Brevet, M. Broyer, J. Chevalere, P. Labastie, and J. P. Perrot, “Electric-field–hindered vibrational autoionization in molecular Rydberg states,” *Phys. Rev. Lett.* **60**, 917 (1988).
- [88] M. Misakian and J. C. Zorn, “Dissociative Excitation of Molecular Hydrogen by Electron Impact,” *Phys. Rev. A* **6**, 2180 (1972).
- [89] K. Kollmann, “Energetic protons from autoionising states of  $H_2$ ,” *J. Phys. B: At. Mol. Phys.* **11**, 339 (1978).
- [90] M. G. Maujean, “Photodissociation of doubly excited states of  $H_2$ , HD, and  $D_2$ ,” *J. Chem. Phys.* **85**, 4830 (1986), <https://doi.org/10.1063/1.451717> .

- [91] Y. M. Chung, E. Lee, T. Masuoka, and J. A. R. Samson, “Dissociative photoionization of H<sub>2</sub> from 18 to 124 eV,” *J. Chem. Phys.* **99**, 885 (1993), <https://doi.org/10.1063/1.465352> .
- [92] R. Browning and J. Fryar, “Dissociative photoionization of H<sub>2</sub> and D<sub>2</sub> through the 1s $\sigma_g$  ionic state,” *J. Phys. B: At. Mol. Phys.* **6**, 364 (1973).
- [93] S. L. Guberman, “The doubly excited autoionizing states of H<sub>2</sub>,” *The Journal of Chemical Physics* **78**, 1404 (1983), <https://doi.org/10.1063/1.444882> .
- [94] I. Sánchez and F. Martín, “The doubly excited states of the H<sub>2</sub> molecule,” *J. Chem. Phys.* **106**, 7720 (1997), <https://doi.org/10.1063/1.473773> .
- [95] I. Sánchez and F. Martín, “Doubly excited autoionizing states of H<sub>2</sub> above the second ionization threshold: the Q2 resonance series,” *J. Chem. Phys.* **110**, 6702 (1999), <https://doi.org/10.1063/1.478576> .
- [96] J. Fernández and F. Martín, “Autoionizing  $^1\Sigma_u^+$  and  $^1\Pi_u$  states of H<sub>2</sub> above the third and fourth ionization thresholds,” *J. Phys. B: At., Mol. Opt. Phys.* **34**, 4141 (2001).
- [97] I. B. Jr and C. E. Bielschowsky, “Doubly excited states of molecular hydrogen: theoretical absorption and photodissociation cross sections,” *J. Phys. B: At., Mol. Opt. Phys.* **33**, 1713 (2000).
- [98] K. Ito, R. I. Hall, and M. Ukai, “Dissociative photoionization of H<sub>2</sub> and D<sub>2</sub> in the energy region of 25–45 eV,” *J. Chem. Phys.* **104**, 8449 (1996), <https://doi.org/10.1063/1.471594> .
- [99] J. L. Sanz-Vicario, H. Bachau, and F. Martín, “Time-dependent theoretical description of molecular autoionization produced by femtosecond xuv laser pulses,” *Phys. Rev. A* **73**, 033410 (2006).
- [100] K. Sakai, S. Stoychev, T. Ouchi, I. Higuchi, M. Schöffler, T. Mazza, H. Fukuzawa, K. Nagaya, M. Yao, Y. Tamenori, A. I. Kuleff, N. Saito, and K. Ueda, “Electron-Transfer-Mediated Decay and Interatomic Coulombic Decay from the Triply Ionized States in Argon Dimers,” *Phys. Rev. Lett.* **106**, 033401 (2011).



- 
- [101] W. Eberhardt, G. Kalkoffen, and C. Kunz, "Measurement of the Auger Decay after Resonance Excitation of Xe  $4d$  and Kr  $3d$  Resonance Lines," *Phys. Rev. Lett.* **41**, 156 (1978).
- [102] J. M. Schins, P. Breger, P. Agostini, R. C. Constantinescu, H. G. Muller, G. Grillon, A. Antonetti, and A. Mysyrowicz, "Observation of Laser-Assisted Auger Decay in Argon," *Phys. Rev. Lett.* **73**, 2180 (1994).
- [103] M. L. Knotek and P. J. Feibelman, "Ion Desorption by Core-Hole Auger Decay," *Phys. Rev. Lett.* **40**, 964 (1978).
- [104] L. S. Cederbaum, J. Zobeley, and F. Tarantelli, "Giant Intermolecular Decay and Fragmentation of Clusters," *Phys. Rev. Lett.* **79**, 4778 (1997).
- [105] S. Marburger, O. Kugeler, U. Hergenhahn, and T. Möller, "Experimental Evidence for Interatomic Coulombic Decay in Ne Clusters," *Phys. Rev. Lett.* **90**, 203401 (2003).
- [106] T. Jahnke, A. Czasch, M. S. Schöffler, S. Schössler, A. Knapp, M. Kász, J. Titze, C. Wimmer, K. Kreidi, R. E. Grisenti, A. Staudte, O. Jagutzki, U. Hergenhahn, H. Schmidt-Böcking, and R. Dörner, "Experimental Observation of Interatomic Coulombic Decay in Neon Dimers," *Phys. Rev. Lett.* **93**, 163401 (2004).
- [107] G. Öhrwall, M. Tchapyguine, M. Lundwall, R. Feifel, H. Bergersen, T. Rander, A. Lindblad, J. Schulz, S. Peredkov, S. Barth, S. Marburger, U. Hergenhahn, S. Svensson, and O. Björneholm, "Femtosecond Interatomic Coulombic Decay in Free Neon Clusters: Large Lifetime Differences between Surface and Bulk," *Phys. Rev. Lett.* **93**, 173401 (2004).
- [108] T. Jahnke, H. Sann, T. Havermeier, K. Kreidi, C. Stuck, M. Meckel, M. Schöffler, N. Neumann, R. Wallauer, S. Voss, *et al.*, "Ultrafast energy transfer between water molecules," *Nat. Phys.* **6**, 139 (2010).

- [109] E. F. Aziz, N. Ottosson, M. Faubel, I. V. Hertel, and B. Winter, "Interaction between liquid water and hydroxide revealed by core-hole de-excitation," *Nature* **455**, 89 (2008).
- [110] M. Mucke, M. Braune, S. Barth, M. Förstel, T. Lischke, V. Ulrich, T. Arion, U. Becker, A. Bradshaw, and U. Hergenhahn, "A hitherto unrecognized source of low-energy electrons in water," *Nat. Phys.* **6**, 143 (2010).
- [111] S. Scheit, L. S. Cederbaum, and H.-D. Meyer, "Time-dependent interplay between electron emission and fragmentation in the interatomic Coulombic decay," *J. Chem. Phys.* **118**, 2092 (2003), <https://doi.org/10.1063/1.1531996> .
- [112] R. Santra, J. Zobeley, L. S. Cederbaum, and N. Moiseyev, "Interatomic Coulombic Decay in van der Waals Clusters and Impact of Nuclear Motion," *Phys. Rev. Lett.* **85**, 4490 (2000).
- [113] N. Moiseyev, R. Santra, J. Zobeley, and L. S. Cederbaum, "Fingerprints of the nodal structure of autoionizing vibrational wave functions in clusters: Interatomic Coulombic decay in Ne dimer," *J. Chem. Phys.* **114**, 7351 (2001), <https://doi.org/10.1063/1.1361070> .
- [114] R. Santra, L. Cederbaum, and H.-D. Meyer, "Electronic decay of molecular clusters: non-stationary states computed by standard quantum chemistry methods," *Chemical Physics Letters* **303**, 413 (1999).
- [115] V. Averbukh, I. B. Müller, and L. S. Cederbaum, "Mechanism of Interatomic Coulombic Decay in Clusters," *Phys. Rev. Lett.* **93**, 263002 (2004).
- [116] E. Saldin, E. Schneidmiller, and M. Yurkov, "Statistical properties of radiation from VUV and X-ray free electron laser," *Opt. Commun.* **148**, 383 (1998).
- [117] E. L. Saldin, E. A. Schneidmiller, and M. V. Yurkov, "Statistical and coherence properties of radiation from x-ray free-electron lasers," *New J. Phys.* **12**, 035010 (2010).

- [118] S. Krinsky and R. L. Gluckstern, “Analysis of statistical correlations and intensity spiking in the self-amplified spontaneous-emission free-electron laser,” *Phys. Rev. ST Accel. Beams* **6**, 050701 (2003).
- [119] K. Meyer, C. Ott, P. Raith, A. Kaldun, Y. Jiang, A. Senftleben, M. Kurka, R. Moshhammer, J. Ullrich, and T. Pfeifer, “Noisy Optical Pulses Enhance the Temporal Resolution of Pump-Probe Spectroscopy,” *Phys. Rev. Lett.* **108**, 098302 (2012).
- [120] T. Pfeifer, Y. Jiang, S. Düsterer, R. Moshhammer, and J. Ullrich, “Partial-coherence method to model experimental free-electron laser pulse statistics,” *Opt. Lett.* **35**, 3441 (2010).
- [121] K. Codling, R. G. Houlgate, J. B. West, and P. R. Woodruff, “Angular distribution and photoionization measurements on the 2p and 2s electrons in neon,” *J. Phys. B: At. Mol. Phys.* **9**, L83 (1976).
- [122] A. K. Pradhan, “Photo-ionization cross-sections of Ne II, Ne III and Ne IV,” *Monthly Notices of the Royal Astronomical Society* **190**, 5P (1980).
- [123] S. Scheit, V. Averbukh, H.-D. Meyer, N. Moiseyev, R. Santra, T. Sommerfeld, J. Zobeley, and L. S. Cederbaum, “On the interatomic Coulombic decay in the Ne dimer,” *J. Chem. Phys.* **121**, 8393 (2004), <https://aip.scitation.org/doi/pdf/10.1063/1.1794654> .